Patterns with Potential

Advancing Cardiac Resynchronization Therapy through Imaging-Based Personalized Heart Modeling

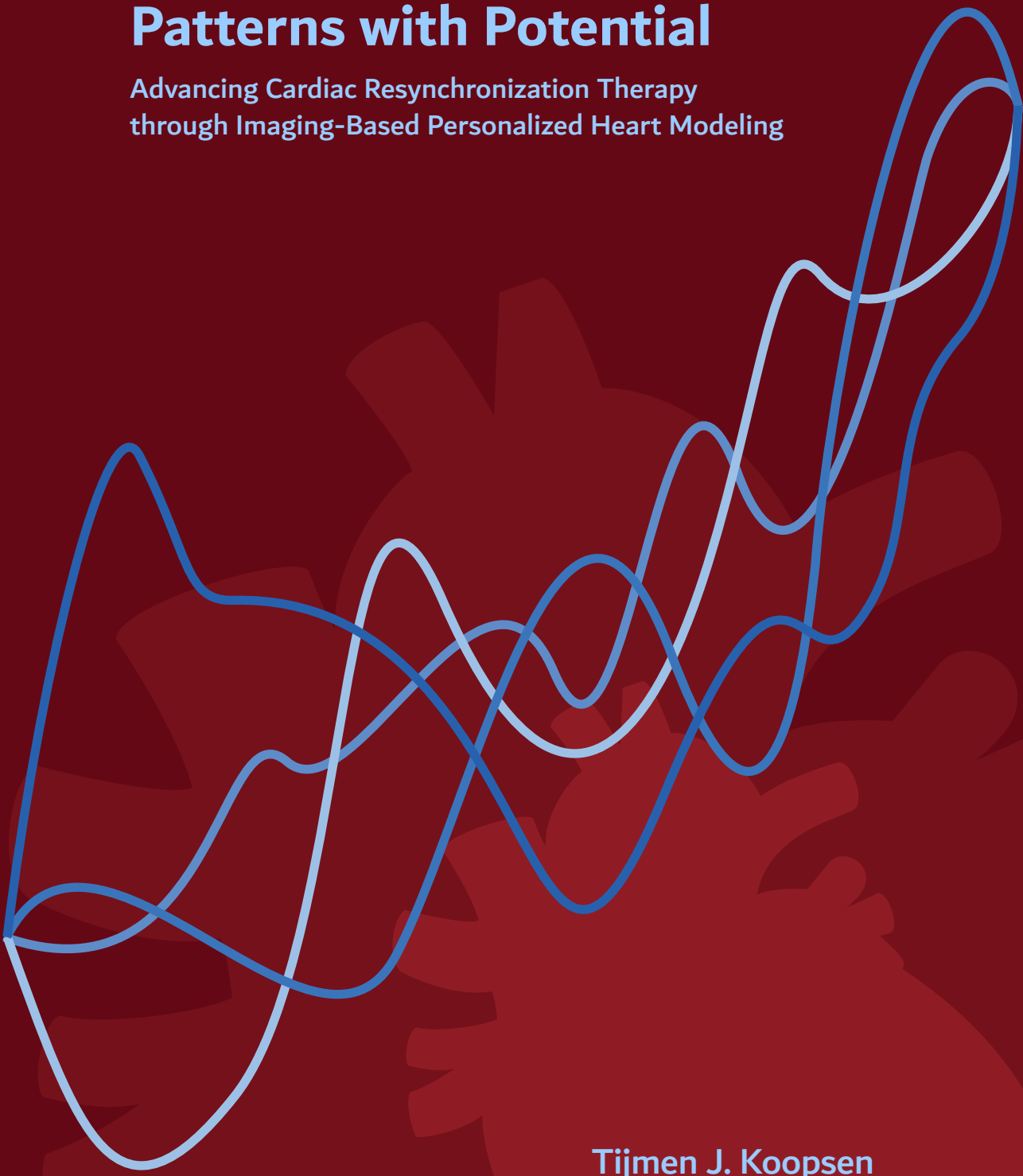

Tijmen J. Koopsen

Patterns with Potential

Advancing Cardiac Resynchronization Therapy through Imaging-Based Personalized Heart Modeling

Tijmen J. Koopsen

Patterns with Potential
Advancing Cardiac Resynchronization Therapy through Imaging-Based Personalized Heart Modeling
Tijmen Koopsen
ISBN: 978-94-6496-304-5

Cover: Steven Laan, Tijmen Koopsen
Lay-out: Ilse Modder, www.ilsemodder.nl
Printing: Gildeprint Enschede, gildeprint.nl

Patterns with Potential

Dissertation

to obtain the degree of Doctor at Maastricht University,
on the authority of the Rector Magnificus, Prof.dr. Pamela Habibović
in accordance with the decision of the Board of Deans,
to be defended in public on Friday 17 January 2025, at 13:00 hours

by

Tijmen Johan Koopsen

born on 4 May 1994
in Veldhoven, The Netherlands

Supervisors

Prof. dr. ir. J. Lumens (Maastricht University, Maastricht, The Netherlands)

Prof. dr. T. Delhaas (Maastricht University, Maastricht, The Netherlands)

Assessment Committee

Chair

Prof. dr. ir. R.L.M. Peeters (Maastricht University, Maastricht, The Netherlands)

Members

Prof. dr. L. Geris (Catholic University Leuven, Leuven, Belgium)

Dr. J.G.L.M. Luermans (Maastricht University Medical Center, Maastricht, The Netherlands)

Prof. dr. J.U. Voigt (Catholic University Leuven, Leuven, Belgium)

Prof. dr. P.G.A. Volders (Maastricht University, Maastricht, The Netherlands)

Financial support by the **Dutch Heart Foundation** for the publication of this thesis is gratefully acknowledged.

Financial support for the publication of this thesis by **Maastricht University** is gratefully acknowledged.

“Understanding of life begins with the understanding of patterns”

- Fritjof Capra

CONTENTS

1

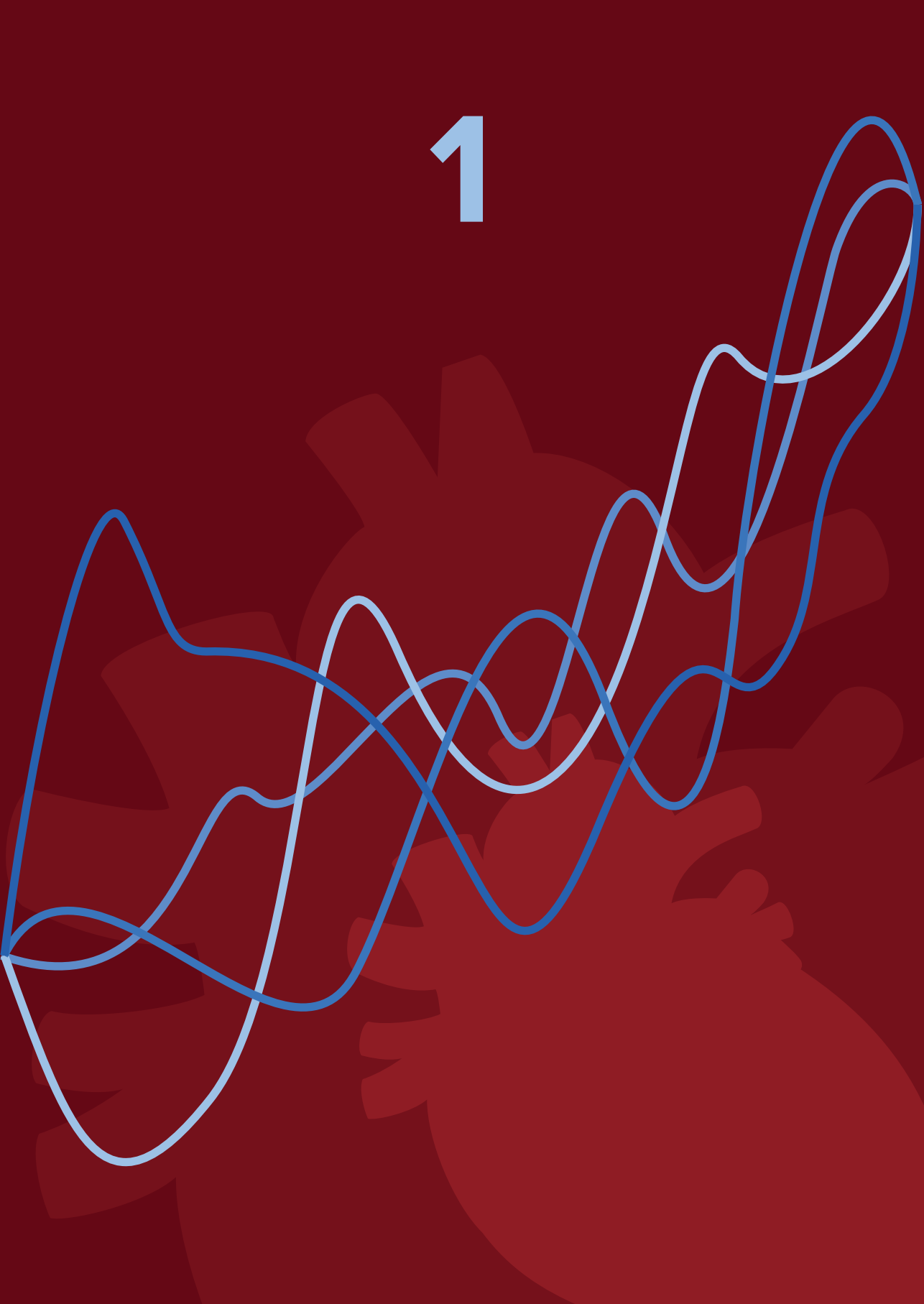

General Introduction

1.1 HEART FAILURE AND DYSSYNCHRONY

Heart failure (HF) is a complex clinical syndrome in which the heart cannot pump enough blood to meet the body's demands [1]. It is a significant health problem that affects 1-2% of adults worldwide, with a prevalence that is only expected to increase in the upcoming years. Despite recent improvements in pharmacological treatment of HF, patients often have a reduced quality of life and five-year mortality rates remain as high as 67% [2].

Approximately one-third of HF patients has a ventricular conduction disturbance, most frequently left bundle branch block (LBBB) [3]. Abnormal ventricular conduction leads to a dyssynchronous contraction of the ventricles, which impairs cardiac pump function and stimulates ventricular remodeling [4-6]. Conduction abnormalities can thereby cause HF development [7], but they may also evolve as a consequence of existing HF and accelerate disease progression [8]. Heart failure patients with LBBB have been associated with a worse prognosis than those without [9].

1.2 CARDIAC RESYNCHRONIZATION THERAPY: A SUCCESSFUL HEART FAILURE TREATMENT?

Cardiac resynchronization therapy (CRT) is an established device therapy for dyssynchronous HF patients with a reduced LV ejection fraction (EF) [1]. The aim of CRT is to restore a synchronous contraction and relaxation of the ventricles through biventricular pacing. Clinical studies have demonstrated that CRT acutely improves pump function [10] and that it reduces HF symptoms and mortality [11,12].

Based on the results of large clinical trials [13-15], CRT is currently recommended in HF patients with an LVEF ≤35% who have a QRS duration ≥150 ms with LBBB QRS morphology [1]. In patients with a QRS duration between 130 and 149 ms or non-LBBB morphology, outcome after CRT is less certain, and CRT should be considered. CRT device implantation is not recommended in patients with a narrow QRS complex (<130 ms) [14].

Despite the important success of CRT as an HF treatment, a significant uncertainty remains about which patients will benefit from this therapy. Up to 45% of implanted patients are found to be non-responders, depending on the response criteria used [16]. At the same time, a large number of eligible patients do not currently receive a CRT device [17]. Therefore, strategies to further improve patient selection and delivery of CRT are essential [18].

1.3 MYOCARDIAL DEFORMATION: A MISSING PIECE OF THE PUZZLE?

In HF patients with LBBB, speckle tracking echocardiography has demonstrated a typical LV deformation pattern which reflects the septal-to-lateral electro-mechanical interactions [19,20]. This deformation pattern is characterized by early systolic shortening of the septum paralleled by stretching of the lateral wall, followed by septal systolic rebound stretch accompanied with a pronounced shortening of the lateral wall [20]. In studies which have included follow-up after CRT, this typical deformation pattern has been associated with a positive response [21-24].

In contrast, septal strain patterns with a different morphology during LBBB, especially those with a pseudonormal shortening including a late-systolic shortening peak, have been linked to less favorable outcomes after CRT [22,25]. Clinical, experimental, and computational studies have explained these findings by showing that these abnormal strain patterns are caused by an additional loss of myocardial contractility, e.g. as a consequence of ischemia or infarction [22,26]. Based on these observations, the septal rebound stretch (SRS) and systolic stretch index (SSI) have been introduced as prognostic indices and these indices showed to be additive to ECG characteristics for the prediction of outcome after CRT [27,28].

Despite the promising results obtained in these retrospective studies, deformation imaging is not yet part of clinical routine to select candidates for CRT [1]. This is due to the lack of evidence in randomized clinical trials which did not demonstrate an additional predictive power of mechanical dyssynchrony indices on top of ECG parameters in populations with a wide QRS complex [29,30]. More studies are needed to show that strain has prognostic value which is additive to the currently used clinical guidelines.

1.4 FROM POPULATION TO INDIVIDUAL: THE DIGITAL TWIN OF THE FAILING HEART

While strain indices have shown to provide valuable prognostic information in CRT candidates, these indices reduce a patient's complex set of myocardial deformation patterns to a single quantitative index. This index is expected to have limited discriminative power to determine the unique electro-mechanical disease substrate of HF patients, which could be an essential step to further improve prediction of the potential of CRT. The classification of patients based on septal strain morphology involves a similar non-uniqueness due to interindividual variability within subgroups.

The most important hypothesis of this thesis is that a personalized approach, which focuses on characterization of the unique electro-mechanical disease substrate of a patient, is the key to better patient selection and delivery of CRT. This hypothesis follows recent developments in the field of personalized medicine which are based on generating

the patient's Digital Twin [31]. The Digital Twin is a virtual representation of the patient which is obtained by integrating patient-specific measurements into a generic statistical or mechanistic model. As a result, the Digital Twin includes the patient's unique cardiovascular properties and can be used to evaluate the effect of virtual therapies.

To develop a representative Digital Twin, several challenges need to be dealt with [32]. One challenge includes the choice of an appropriate model which allows to integrate the available measurement data. The CircAdapt model of the human heart and circulation [33] provides a suitable model to integrate myocardial strain measurements, due to its ability to simulate regional myocardial mechanics at the same spatial scale as current non-invasive strain imaging technologies and at low computational cost. Furthermore, relevant model parameters for personalization should be selected (Parameter challenge), an optimization method should be designed (Optimization challenge), and estimated model parameters should be translated into meaningful diagnostic or prognostic indices (Translation challenge). All of these challenges will be addressed in this thesis.

1.5 AIM AND OUTLINE OF THE THESIS

The aim of this thesis is to obtain more insight into the electro-mechanical disease substrates of dyssynchronous HF patients and to investigate whether integrative imaging-based characterization of the patient's disease can help to predict response to CRT. To achieve this aim, we integrate non-invasive imaging data, i.e. LV cavity volume and regional strain measurements, into the CircAdapt model of the human heart and circulation to generate the patient's Digital Twin. In **Chapter 2**, we perform simulations to reproduce distinct LV strain patterns as observed in dyssynchronous HF patients. Given the differences in CRT response associated with these strain patterns, we generate hypotheses about the underlying myocardial abnormalities and we illustrate the usefulness of a patient-specific modeling approach based on strain patterns. Since myocardial infarction (MI) has been shown to be an important determinant of the effect of CRT, we aim to realistically simulate myocardial mechanics during ischemia and infarction. In **Chapter 3**, we therefore introduce a novel modeling approach for MI which is validated by comparison with experimental and clinical deformation measurements. To ensure reliable parameter estimations in personalized models of the failing heart, in **Chapter 4**, we apply a framework of sensitivity and identifiability analysis to determine which model parameters can be identified from echocardiographic LV cavity volume and regional strain measurements. This subset of model parameters is used to generate the patient's Digital Twin. In **Chapter 5**, this Digital Twin technology is retrospectively tested in a population of HF patients selected for CRT. Using virtual pacing in the Digital Twin, the effect of CRT is predicted and compared with clinical outcome. The concluding **Chapter 6** discusses the Digital Twin approach in a more global context, addressing both technological and clinical aspects. Furthermore, an outlook on potential future improvements is provided.

REFERENCES

1. McDonagh TA *et al.* (2021). 2021 ESC Guidelines for the diagnosis and treatment of acute and chronic heart failure. *Eur. Heart J.* 42(36), 3599-3726.
2. Tsao CW, Lyass A, Enserro D, Larson MG, Ho JE, Kizer JR, Gottdiener JS, Psaty BM, Vasan RS (2018). Temporal Trends in the Incidence of and Mortality Associated With Heart Failure With Preserved and Reduced Ejection Fraction. *JACC Heart Failure.* 6(8), 678-685.
3. Auricchio A, Prinzen FW (2017). Enhancing Response in the Cardiac Resynchronization Therapy Patient: The 3B Perspective—Bench, Bits, and Bedside. *JACC Clin. Electrophysiol.* 3(11), 1203-1219.
4. van Oosterhout MFM, Prinzen FW, Arts T, Schreuder JJ, Vanagt WYR, Cleutjens JPM, Reneman RS (1998). Asynchronous electrical activation induces asymmetrical hypertrophy of the left ventricular wall. *Circulation*. 98(6), 588-595.
5. Vernooy K, Verbeek XAAM, Peschar M, Crijns HJGM, Arts T, Cornelussen RNM, Prinzen FW (2005). Left bundle branch block induces ventricular remodelling and functional septal hypoperfusion. *Eur. Heart J.* 26(1), 91-98.
6. Nguyên UC, Verzaal NJ, van Nieuwenhoven FA, Vernooy K, Prinzen FW (2018). Pathobiology of cardiac dyssynchrony and resynchronization therapy. *Europace*. 20(12), 1898-1909.
7. Zannad F *et al.* (2007). Left bundle branch block as a risk factor for progression to heart failure. *Eur. J. Heart Fail.* 9(1), 7-14.
8. Sletten OJ *et al.* (2021). Lateral Wall Dysfunction Signals Onset of Progressive Heart Failure in Left Bundle Branch Block. *JACC Cardiovasc. Imaging*. 14(11), 2059-2069.
9. Baldasseroni S *et al.* (2002). Left bundle-branch block is associated with increased 1-year sudden and total mortality rate in 5517 outpatients with congestive heart failure: A report from the Italian Network on Congestive Heart Failure. *Am. Heart J.* 143(3), 398-405.
10. de Roest GJ, Allaart CP, Kleijn SA, Delnoy PPHM, Wu L, Hendriks ML, Bronzwaer JGF, van Rossum AC, de Cock CC (2013). Prediction of long-term outcome of cardiac resynchronization therapy by acute pressure-volume loop measurements. *Eur J. Heart Fail.* 15, 299-307.
11. Cleland JGF, Daubert JC, Erdmann E, Freemantle N, Gras D, Kappenberger L, Tavazzi L (2005). The Effect of Cardiac Resynchronization on Morbidity and Mortality in Heart Failure. *N. Engl. J. Med.* 352(15), 1539-1549.
12. Moss AJ *et al.* (2009). Cardiac-Resynchronization Therapy for the Prevention of Heart-Failure Events. *N. Engl. J. Med.* 361(14), 1329-1338.
13. Abraham WT *et al.* (2002). Cardiac Resynchronization in Chronic Heart Failure. *N. Engl. J. Med.* 346(24), 1845-1853.
14. Ruschitzka F *et al.* (2013). Cardiac-Resynchronization Therapy in Heart Failure with a Narrow QRS Complex. *N. Engl. J. Med.* 369(15), 1395-1405.
15. Cleland JG, Abraham WT, Linde C, Gold MR, Young JB, Daubert JC, Sherfesee L, Wells GA, Tang ASL (2013). An individual patient meta-analysis of five randomized trials assessing the effects of cardiac resynchronization therapy on morbidity and mortality in patients with symptomatic heart failure. *Eur. Heart J.* 34(46), 3547-3556.
16. Daubert C, Behar N, Martins RP, Mabo P, Leclercq C (2017). Avoiding non-responders to cardiac resynchronization therapy: A practical guide. *Eur. Heart J.* 38(19), 1463-1472.
17. Mullens W *et al.* (2020). Optimized implementation of cardiac resynchronization therapy: a call for action for

referral and optimization of care: A joint position statement from the Heart Failure Association (HFA), European Heart Rhythm Association (EHRA), and European Association. *Eur. J. Heart Fail.* 22(12), 2349-2369.

18. Mullens W, Grimm RA, Verga T, Dresing T, Starling RC, Wilkoff BL, Tang W (2009). Insights From a Cardiac Resynchronization Optimization Clinic as Part of a Heart Failure Disease Management Program. *J. Am. Coll. Cardiol*. 53(9), 765-773.
19. Voigt JU, Schneider TM, Korder S, Szulik M, Gürel E, Daniel WG, Rademakers F, Flachskampf FA (2009). Apical transverse motion as surrogate parameter to determine regional left ventricular function inhomogeneities: A new, integrative approach to left ventricular asynchrony assessment. *Eur. Heart. J.* 30(8), 959-968.
20. Risum N *et al.* (2012). Simple regional strain pattern analysis to predict response to cardiac resynchronization therapy: Rationale, initial results, and advantages. *Am. Heart J.* 163(4), 697-704.
21. Parsai *et al.* (2009). Toward understanding response to cardiac resynchronization therapy: Left ventricular dyssynchrony is only one of multiple mechanisms. *Eur. Heart J.* 30(8), 940-949.
22. Leenders GE, Lumens J, Cramer MJ, De Boeck BWL, Doevendans PA, Delhaas T, Prinzen FW (2011). Septal Deformation Patterns Delineate Mechanical Dyssynchrony and Regional Differences in Contractility: Analysis of Patient Data Using a Computer Model. *Circ. Heart Fail.* 5(1), 87-96.
23. Ross S, Nestaas E, Kongsgaard E, Odland HH, Haland TF, Hopp E, Haugaa KH, Edvardsen T (2020). Septal contraction predicts acute haemodynamic improvement and paced QRS width reduction in cardiac resynchronization therapy. *Eur. Heart J. Cardiovasc. Imaging.* 21(8), 845-852.
24. Risum N *et al.* (2015). Identification of Typical Left Bundle Branch Block Contraction by Strain Echocardiography Is Additive to Electrocardiography in Prediction of Long-Term Outcome after Cardiac Resynchronization Therapy. *J. Am. Coll. Cardiol.* 66(6), 631-641.
25. Maréchaux S *et al.* (2014). Relationship between two-dimensional speckle-tracking septal strain and response to cardiac resynchronization therapy in patients with left ventricular dysfunction and left bundle branch block: A prospective pilot study. *J. Am. Soc. Echocardiogr.* 27(5), 501-511.
26. Aalen JM *et al.* (2019). Mechanism of Abnormal Septal Motion in Left Bundle Branch Block: Role of Left Ventricular Wall Interactions and Myocardial Scar. *JACC Cardiovasc. Imaging.* 12(12), 2402-2413.
27. Lumens J *et al.* (2015). Differentiating Electromechanical from Non-Electrical Substrates of Mechanical Discoordination to Identify Responders to Cardiac Resynchronization Therapy. *Circ. Cardiovasc. Imaging.* 8(9), 1-12.
28. Gorcsan J, Anderson CP, Tayal B, Sugahara M, Walmsley J, Starling RC, Lumens J (2019). Systolic Stretch Characterizes the Electromechanical Substrate Responsive to Cardiac Resynchronization Therapy. *JACC Cardiovasc. Imaging*. 12(9), 1741-1752.
29. Chung ES *et al.* (2008). Results of the Predictors of Response to CRT (PROSPECT) Trial. *Circulation*. 117(20), 2608-2616.
30. Seo Y, Ito H, Nakatani S, Takami M, Naito S, Shiga T, Ando K, Wakayama Y, Aonuma K (2011). The role of echocardiography in predicting responders to cardiac resynchronization therapy - Results from the Japan cardiac resynchronization therapy registry trial (J-CRT). *Circ. J.* 75(5), 1156-1163.
31. Corral-Acero J *et al.* (2020). The 'Digital Twin' to enable the vision of precision cardiology. *Eur. Heart J.* 41(48), 4556-4564.
32. Gray RA, Pathmanathan P (2018). Patient-specific cardiovascular computational modeling: Diversity of

personalization and challenges. *J. Cardiovasc. Transl. Res.* 11(2), 80-88.

33. Arts T, Delhaas T, Bovendeerd P, Verbeek X, Prinzen FW (2004). Adaptation to mechanical load determines shape and properties of heart and circulation: the CircAdapt model. *Am. J. Physiol. Circ. Physiol.* 288(4), H1943-H1954.

2

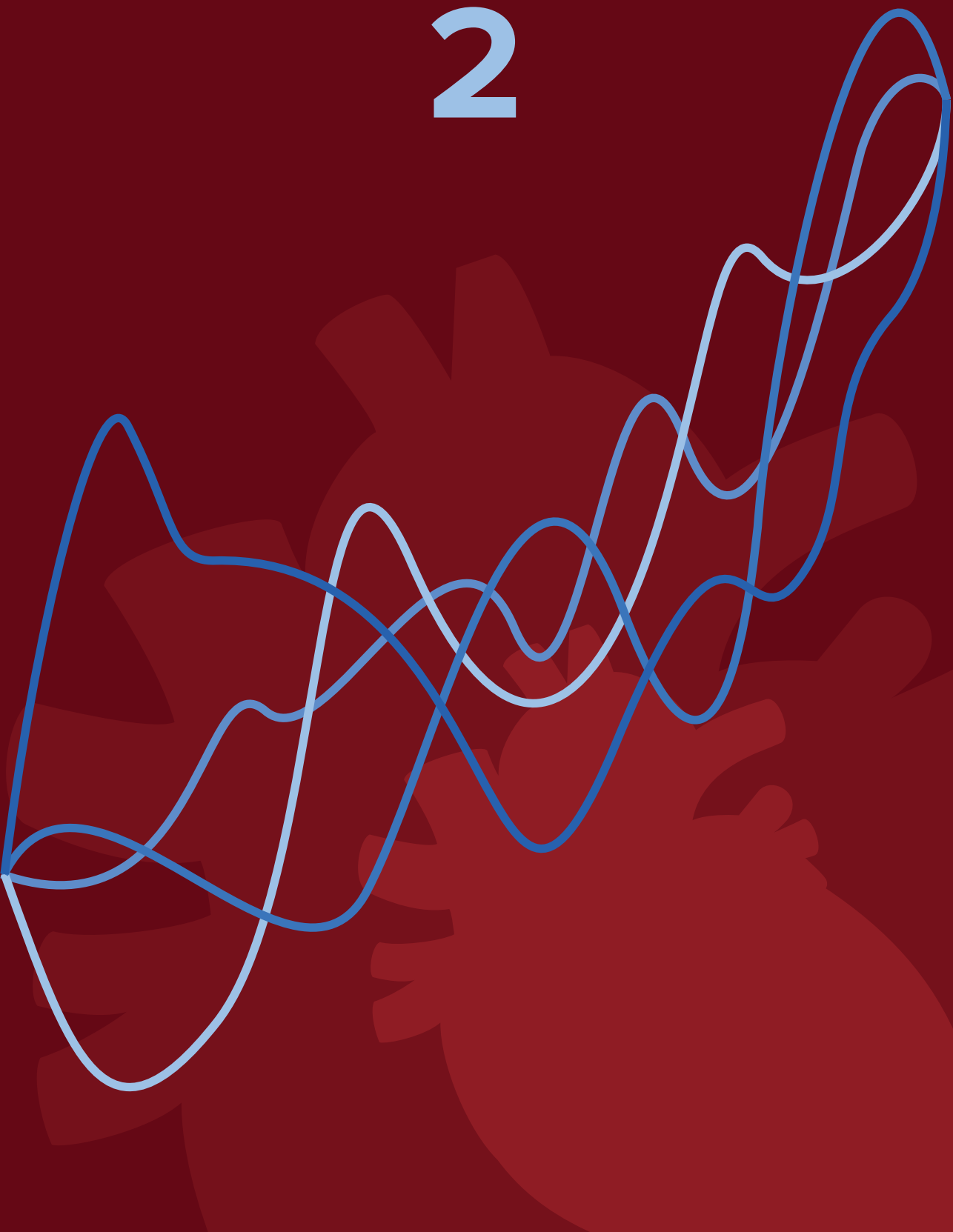

What Do We Gain from Septal Strain?

J. Lumens, T. Koopsen, and A.S. Beela, “What Do We Gain from Septal Strain?”,

JACC Cardiovasc. Imaging 2021;14(9):1703-1706.

2.1 INTRODUCTION

Left bundle branch block (LBBB) has been long recognized as a ventricular conduction disorder in humans. Although it is a rather common finding in patients with chronic heart failure [1], LBBB is relatively rare in the general population [2]. It is well recognized that LBBB can lead to progressive worsening of cardiac pump function and thereby contributes to the development of heart failure. Bolstered by the development of cardiac resynchronization therapy, LBBB has become a therapeutic target.

2.2 THE POLARIZING EFFECT OF LBBB ON LEFT VENTRICULAR FUNCTION

Many studies have revealed the characteristic polarizing effect of isolated LBBB on the electromechanical function of the ventricular myocardium [3-5]. In the healthy heart, the relatively synchronous electric activation of the ventricular myocardium guarantees a rather uniform distribution of mechanical contraction, relaxation, and work across the ventricular walls. This electromechanical harmony is disturbed by LBBB and replaced with a characteristic pattern of mechanical interactions between the early-activated septum and late-activated lateral wall (Figure 2.1, second column). Speckle tracking echocardiography has propelled our mechanistic understanding of LBBB-induced mechanical dyssynchrony by enabling the noninvasive measurement of regional myocardial deformation in the ventricular walls. Before the onset of left ventricular (LV) ejection, the early-activated septal myocardium is already actively contracting, while the late-activated lateral myocardium is still in a passive state, offering little resistance to septal shortening and explaining the pre-ejection shortening of the septum and stretch of the lateral wall. As a consequence, the lateral wall is preloaded more than the septal wall upon electric activation. The combination of this regional preload disparity and the myofilament property of length-dependent activation (i.e., the cellular basis of the Frank-Starling law) [6] results in normal or even supranormal shortening of the lateral wall and less than normal shortening or even systolic stretching of the septum during ejection. As a result, myocardial workload is unevenly distributed in the LBBB heart, with the septum performing little or even negative work, and the lateral wall experiencing a (supra)normal workload [3-5].

2.3 COMPETITIVE FORCES SHAPING SEPTAL STRAIN

The exact morphology of a septal strain pattern in patients with LBBB can be seen as the integrative result of a competition between rivaling forces originating from the septal and lateral myocardial segments, triggered by the electric activation delay and modulated by

the contractility of both walls. Using a combination of computer simulations and patient data, Leenders et al. [7] were the first to describe how the classical septal strain pattern in LBBB patients is modulated by regional changes of contractile strength of the LV myocardium. Their study demonstrated that the presence of a classical septal strain pattern with an early-systolic and a late-systolic shortening peak in patients with LBBB, also reported by others [8-9], discloses relatively preserved contractile function in both the septal and lateral walls. A septal strain pattern with only 1 early-systolic shortening peak followed by systolic rebound stretch, however, was shown to be indicative of a changed balance of contractile forces in favor of the lateral wall. In the same study, most patients with heart failure with LBBB presented with a septal strain pattern with only a late-systolic shortening peak, which could be explained by a global loss of contractile function in both LV walls. As compared to the late-peak pattern, the double-peak and early-peak septal strain patterns were associated with more favorable outcome after cardiac resynchronization therapy, both in terms of LV reverse remodeling and survival [7,10].

2.4 ANOTHER (YET SIMILAR) WAY OF LOOKING AT SEPTAL STRAIN

Calle et al. [11] analyzed the differences in septal deformation patterns in a composite cohort of patients with strict LBBB, covering a much wider range of LV ejection fraction than in previous studies. Alternatively, yet supporting the same concept of competitive forces shaping the septal strain pattern, the authors suggested that progressive ventricular remodeling induced by LBBB [5,12,13], rather than loss of contractile function, can explain the changes of septal strain morphology in LBBB patients. In their study, they categorized septal strain patterns in 4 groups with increasing amplitude of systolic stretch and decreasing peak shortening. LV remodeling was characterized by increased LV end-diastolic cavity dimensions, reduced LV ejection fraction, and increased LV mass index, reflecting LV eccentric remodeling. Despite the cross-sectional nature of the study, their data suggest that the influence of lateral wall contraction on the pattern of septal strain becomes larger over time. The most normal pattern of septal deformation, with no or little systolic stretch and normal or mildly reduced peak strain, was found in patients with preserved LV ejection fraction. In contrast, patients with more pronounced LV systolic dysfunction presented with more abnormal septal strain patterns, characterized by significant systolic stretch and reduced amplitude of shortening during ejection. Given the low prevalence of LBBB in structurally normal hearts, the authors aimed for patients with LBBB induced by transcatheter aortic valve replacement to represent a new-onset, nonremodeled LBBB substrate. Indeed, the majority of those patients demonstrated the most normal septal strain pattern, referred to as a stage LBBB-1 pattern. Although this pattern was a common finding in their study, animal models of acute LBBB presented with the classical septal strain

pattern, with systolic stretch and reduced peak shortening [5,14]. Therefore, more research is needed to determine whether the differences between stage LBBB-1 and stage LBBB-2 septal strain patterns, as proposed by Calle et al. [11], can be caused by LBBB-induced remodeling or by a difference in myocardial properties before the onset of LBBB. After all, most transcatheter aortic valve replacement patients have extensively remodeled hearts with hypertrophic and stiff LV walls, most likely responding differently to new-onset LBBB.

2.5 CAN SEPTAL STRAIN REFLECT THE EXTENT OF LBBB-INDUCED REMODELING?

To investigate this hypothesis, we performed computer simulations using the well-established CircAdapt model of the human heart and circulation (www.circadapt.org, Maastricht University), which enables realistic simulation of regional myocardial mechanics and global hemodynamics in the failing heart with LBBB [4,7,15]. Figure 2.1 shows simulated septal and lateral wall strain patterns in LBBB hearts with no structural LV remodeling (Figure 2.1, second column) and with increasing LV eccentric remodeling (Figure 2.1, third and fourth columns). The simulations corroborate the findings of Calle et al. [11] by demonstrating that LV eccentric remodeling can change the morphology of septal strain from a classical double-peak pattern (stage LBBB-2/LBBB-3) to a pattern with a single early-systolic shortening peak followed by stretch during the entire ejection phase. Furthermore, the model confirmed that LV concentric remodeling can transform the stage LBBB-2 pattern into a stage LBBB-1 pattern (Figure 2.1, first column).

2.6 THE DIAGNOSTIC GAIN OF SEPTAL STRAIN

Although the 12-lead electrocardiogram remains the preferred diagnostic modality to confirm or exclude the presence of LBBB, echocardiographic assessment of septal deformation can reveal the contractile status of the LV myocardium, which can be compromised by regional myocardial dysfunction related to ischemia, scar, and adverse remodeling. As such, the septum can be thought of as a whistleblower revealing a disturbed balance of septal-to-lateral contractile strength. Both the study by Calle et al. [11] and these simulations suggest that this balance is modulated by LV volumetric remodeling, among other factors, induced by LBBB.

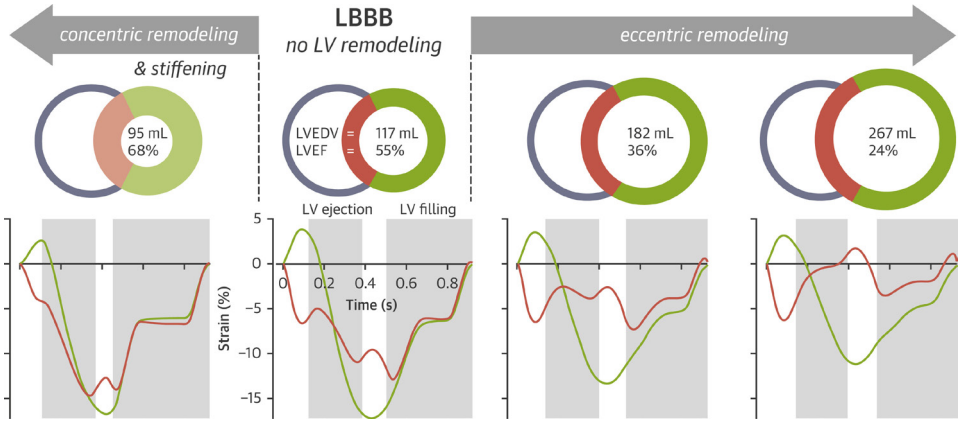

Figure 2.1: Simulations of septal strain and LV remodeling. Starting from the LBBB simulation with no LV remodeling (second column) and a classical double-peak septal strain pattern, increasing the extent of LV eccentric remodeling (third and fourth column) led to a significant morphology change of the septal strain pattern, showing more or even only septal stretch during the LV ejection phase and reduced values of peak shortening in both walls. In contrast, a combination of LV concentric remodeling and global myocardial stiffening (first column) transformed the classical LBBB-induced septal strain pattern into a pattern with continuous systolic septal shortening and relatively normal peak shortening in both walls. Simulations were performed using the CircAdapt model of the human heart and circulation (www.circadapt.org, Maastricht University). In all simulations, LBBB was simulated by delaying the mean LV free wall activation time 30 ms relative to mean septal and right ventricular free wall activation times. LV eccentric remodeling was simulated by a simultaneous increase of wall mass and area, by 20% and 30% (third column) and by 40% and 60% (fourth column), respectively. LV concentric remodeling was simulated by increasing wall mass and stiffness by 20% and 300%, respectively. Heart rate (65 beats/min) and cardiac output (4.2 L/min) were the same for all simulations. LBBB = left bundle branch block; LV = left ventricular.

REFERENCES

1. Clark AL, Goode K, Cleland JGF (2008). The prevalence and incidence of left bundle branch block in ambulant patients with chronic heart failure. *Eur. J. Heart Fail.* 10(7), 696-702.
2. Koskinas KC, Ziakas A (2015). Left Bundle Branch Block in Cardiovascular Disease: Clinical Significance and Remaining Controversies. *Angiology.* 66(9), 797-800.
3. Russell K *et al.* (2012). A novel clinical method for quantification of regional left ventricular pressure-strain loop area: a non-invasive index of myocardial work. *Eur. Heart J.* 33(6), 724-733.
4. Lumens J *et al.* (2013). Comparative electromechanical and hemodynamic effects of left ventricular and biventricular pacing in dyssynchronous heart failure: Electrical resynchronization versus left-right ventricular interaction. *J. Am. Coll. Cardiol.* 62(25), 2395-2403.
5. Vernooy K, Verbeek XAAM, Peschar M, Crijns HJGM, Arts T, Cornelussen RNM, Prinzen FW (2005). Left bundle branch block induces ventricular remodelling and functional septal hypoperfusion. *Eur. Heart J.* 26(1), 91-98.
6. de Tombe PP, Mateja RD, Tachampa K, Ait Mou Y, Farman GP, Irving TC (2010). Myofilament length dependent activation. *J. Mol. Cell. Cardiol.* 48(5), 851-858.
7. Leenders GE, Lumens J, Cramer MJ, De Boeck BWL, Doevendans PA, Delhaas T, Prinzen FW (2011). Septal Deformation Patterns Delineate Mechanical Dyssynchrony and Regional Differences in Contractility: Analysis of Patient Data Using a Computer Model. *Circ. Heart Fail.* 5(1), 87-96.
8. De Boeck BWL, Teske AJ, Meine M, Leenders GE, Cramer MJ, Prinzen FW, Doevendans PA (2009). Septal rebound stretch reflects the functional substrate to cardiac resynchronization therapy and predicts volumetric and neurohormonal response. *Eur. J. Heart Fail.* 11(9), 863-871.
9. Risum N *et al.* (2012). Simple regional strain pattern analysis to predict response to cardiac resynchronization therapy: Rationale, initial results, and advantages. *Am. Heart J.* 163(4), 697-704.
10. Maréchaux S *et al.* (2014). Relationship between two-dimensional speckle-tracking septal strain and response to cardiac resynchronization therapy in patients with left ventricular dysfunction and left bundle branch block: A prospective pilot study. *J. Am. Soc. Echocardiogr.* 27(5), 501-511.
11. Calle S, Kamoen V, De Buyzere M, De Pooter J, Timmermans F (2021). A Strain-Based Staging Classification of Left Bundle Branch Block-Induced Cardiac Remodeling. *JACC Cardiovasc. Imaging.* 14(9), 1691-1702.
12. Vernooy K, Cornelussen RNM, Verbeek XAAM, Vanagt WYR, van Hunnik A, Kuiper M, Arts T, Crijns HJGM, Prinzen FW (2007). Cardiac resynchronization therapy cures dyssynchronopathy in canine left bundle-branch block hearts. *Eur. Heart J.* 28(17), 2148-2155.
13. Prinzen FW, Cheriex EC, Delhaas T, van Oosterhout MFM, Arts T, Wellens HJJ, Reneman RS (1995). Asymmetric thickness of the left ventricular wall resulting from asynchronous electric activation: A study in dogs with ventricular pacing and in patients with left bundle branch block. *Am. Heart J.* 130(5), 1045-1053.
14. Russell K, Opdahl A, Remme EW, Gjesdal O, Skulstad H, Kongsgaard E, Edvardsen T, Smiseth OA (2010). Evaluation of left ventricular dyssynchrony by onset of active myocardial force generation: A novel method that differentiates between electrical and mechanical etiologies. *Circ. Cardiovasc. Imaging.* 3(4), 405-414.
15. Walmsley J, Arts T, Derval N, Bordachar P, Cochet H, Ploux S, Prinzen FW, Delhaas T, Lumens J (2015). Fast Simulation of Mechanical Heterogeneity in the Electrically Asynchronous Heart Using the MultiPatch Module. *PLoS Comput. Biol.* 11(7), 1-23.

3

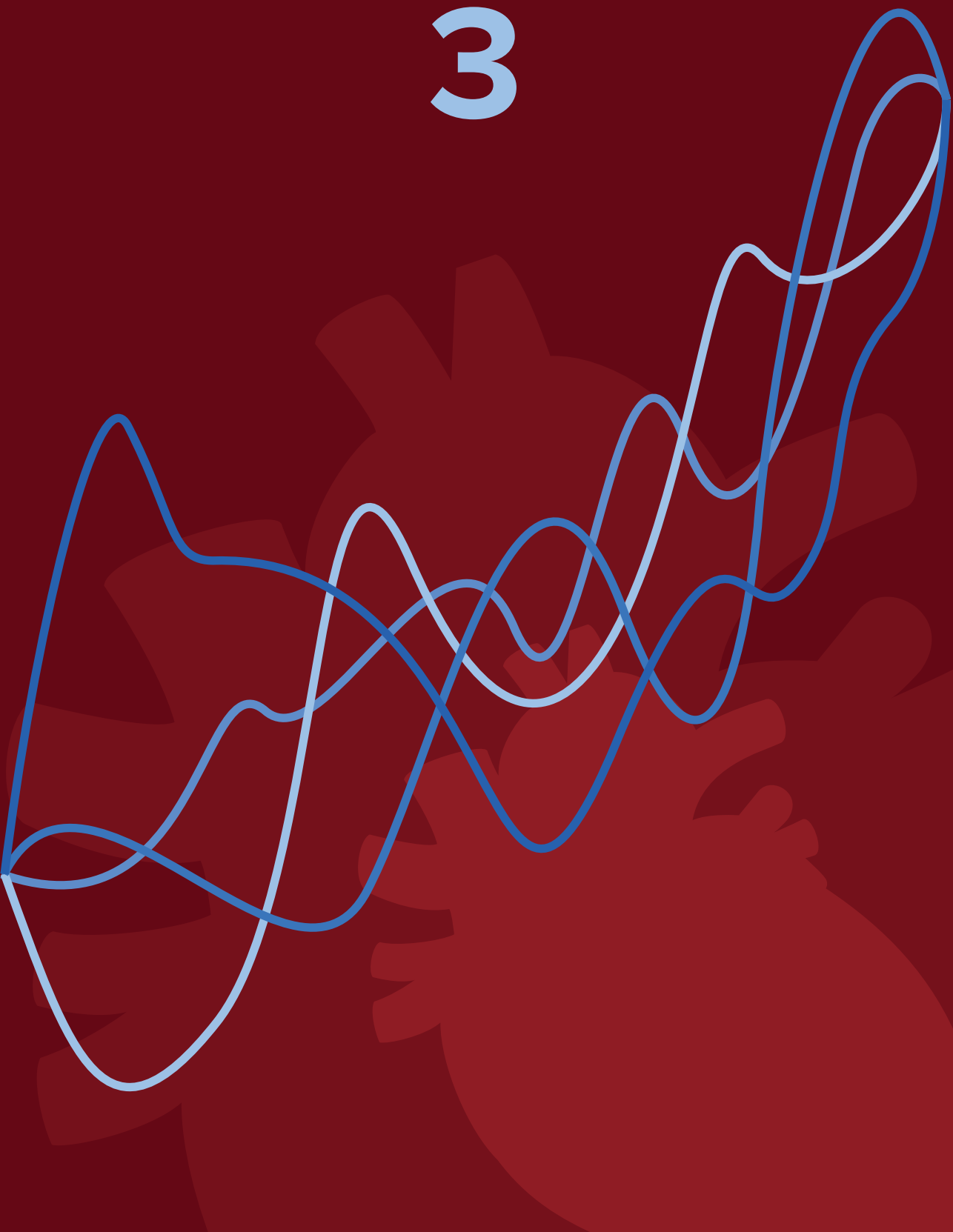

A Lumped Two-Compartment Model for Simulation of Ventricular Pump and Tissue Mechanics in Ischemic Heart Disease

T. Koopsen, N. van Osta, T. van Loon, F.A. van Nieuwenhoven, F.W. Prinzen, B.R. van Klarenbosch, F.P. Kirkels, A.J. Teske, K. Vernooy, T. Delhaas, and J. Lumens, "A Lumped Two-Compartment Model for Simulation of Ventricular Pump and Tissue Mechanics in Ischemic Heart Disease",

Front. Physiol. 2022;13:782592.

ABSTRACT

Computational modeling of cardiac mechanics and hemodynamics in ischemic heart disease (IHD) is important for better understanding of the complex relations between ischemia-induced heterogeneity of myocardial tissue properties, regional tissue mechanics, and hemodynamic pump function. We validated and applied a lumped two-compartment modeling approach for IHD integrated into the CircAdapt model of the human heart and circulation.

Ischemic contractile dysfunction was simulated by subdividing a left ventricular (LV) wall segment into a hypothetical contractile and non-contractile compartment, and dysfunction severity was determined by the non-contractile volume fraction ($NCVF$). Myocardial stiffness was determined by zero-passive stress length ($L_{s0,pas}$) and non-linearity (k_{ECM}) of the passive stress-sarcomere length relation of the non-contractile compartment. Simulated end-systolic pressure volume relations (ESPVRs) for 20% acute ischemia were qualitatively compared between a two- and one-compartment simulation, and parameters of the two-compartment model were tuned to previously published canine data of regional myocardial deformation during acute and prolonged ischemia and reperfusion. In six patients with myocardial infarction (MI), $NCVF$ was automatically estimated using echocardiographic LV strain and volume measurements obtained acutely and six months after MI. Estimated segmental $NCVF$ values at baseline and 6-month follow-up were compared with percentage late gadolinium enhancement (LGE) at 6-month follow-up.

Simulation of 20% $NCVF$ shifted the ESPVR rightward while moderately reducing slope, while a one-compartment simulation caused a leftward shift with severe reduction in slope. Through tuning of $NCVF$, $L_{s0,pas}$ and k_{ECM} it was found that manipulation of $NCVF$ alone reproduced the deformation during acute ischemia and reperfusion, while additional manipulations of $L_{s0,pas}$ and k_{ECM} were required to reproduce deformation during prolonged ischemia and reperfusion. Out of all segments with LGE>25% at follow-up, the majority (68%) had higher estimated $NCVF$ at baseline than at follow-up. Furthermore, baseline $NCVF$ correlated better with percentage LGE than did $NCVF$ at follow-up.

We successfully used a two-compartment model for simulation of ventricular pump and tissue mechanics in IHD. Patient-specific optimizations using regional myocardial deformation estimated $NCVF$ in a small cohort of MI patients in the acute and chronic phase after MI while estimated $NCVF$ values closely approximated the extent of myocardial scar at follow-up. In future studies, this approach can facilitate deformation imaging-based estimation of myocardial tissue properties in patients with cardiovascular disease.

3.1 INTRODUCTION

Computational modeling of cardiac mechanics and hemodynamics in ischemic heart disease (IHD) is important for better understanding of the complex relations between ischemia-induced heterogeneity of myocardial tissue properties, regional tissue mechanics, and hemodynamic pump function. Spatially detailed three-dimensional models based on the finite element method (FEM) are most frequently used for simulation of myocardial infarction (MI) and its effects on cardiac geometry, tissue mechanics, and electrophysiology. While many studies have successfully used FEM models for investigating the pathophysiology and potential treatment of MI [1-13], complexity of these models can provide a problem when performing simulations on a patient-specific level [14].

Reduced-order modeling approaches with sufficient spatial and physiological detail to accurately simulate global and regional tissue mechanics are important for patient-specific simulation of MI [14,15]. The CircAdapt lumped-parameter model of the human heart and circulation is a closed-loop model which simulates real-time, beat-to-beat hemodynamics and mechanics of heart and blood vessels [16,17]. Previous studies using CircAdapt have shown that the model realistically simulates global ventricular hemodynamics and regional myocardial mechanics in various pathological conditions [17,18]. However, its ability to simulate the effects of ischemia-induced contractile dysfunction on both global pump and regional tissue mechanics has not been evaluated yet.

In this study, we present and test a modeling approach for MI-induced myocardial contractile dysfunction, which is integrated into the CircAdapt modeling framework. Following previous observations by Sunagawa et al. [19], who showed that global ventricular mechanics during acute regional ischemia were best described using a two-compartment modeling approach, we subdivided an ischemic wall segment into an active and a passive compartment. We validated this two-compartment implementation by comparing its simulated effects of regional ischemia on global LV pump function against the results of a one-compartment implementation, and by tuning parameters of the two-compartment model to mimic existing data of regional myocardial deformation in dogs with coronary artery ligation. We then evaluated whether the model could be used to estimate the severity of regional contractile dysfunction in MI patients by applying an automatic optimization algorithm to measurements of regional myocardial deformation performed within 72 hours and after six months following MI, and by comparing estimated severities to percentage late gadolinium enhancement (LGE) after six months.

3.2 MATERIALS AND METHODS

A brief description of the CircAdapt model components which are most relevant for this study will be given below. For further details on the CircAdapt model we refer to previously published validation studies [17,18]. Thereafter, the one- and two-compartment model for ischemia-induced contractile dysfunction will be described, and we explain how simulated global mechanics were compared between both modeling approaches. Then, we will describe how model simulations using the two-compartment model were tuned using existing experimental measurements. Finally, we will introduce the clinical data and computational methods used for imaging-based estimation of regional contractile dysfunction in patient hearts acutely and six months after MI.

3.2.1 The CircAdapt model

The CircAdapt computational model of the human heart and circulation is a closed-loop lumped-parameter model that simulates beat-to-beat hemodynamics and mechanics of heart and blood vessels [16,17]. The model uses a simplified ventricular geometry, where cardiac walls are represented by thick-walled spherical shells consisting of myofibers. The TriSeg module allows for interventricular interaction by coupling the left (LV) and right ventricular (RV) walls through the interventricular septum [17]. Walls can be subdivided into patches using the MultiPatch module [18], which enables heterogeneity of myocardial tissue properties within the walls. Myofiber active and passive stress generation is modeled using a three-element Hill model [20]. In brief, the series contractile element with time-dependent length $L_{si}(t)$ generates an active stress $\sigma_{f,act}(t)$ which represents the force developed through cross-bridge formation between actin and myosin filaments. The zero-active stress contractile element length $L_{si0,act}$ defines the length at which no active stress is developed. The series elastic element with time-dependent length $L_{se}(t)$ describes the intrinsic elasticity of the sarcomere, and a reference length of $L_{se,iso}$ is used to define the length of the series elastic element at the onset of isovolumetric contraction. Furthermore, the density of cross-bridge formation is described by a time-dependent contractility state variable $C(t, L_{si}(t))$, while active stress generation is scaled by a parameter $S_{f,act}$. Taken together, active stress is calculated as follows:

$$\sigma_{f,act}(t) = S_{f,act} \cdot C(t, L_{si}(t)) \cdot (L_{si}(t) - L_{si0,act}) \cdot \frac{L_{se}(t)}{L_{se,iso}} \quad (3.1)$$

Passive myocardial tissue behavior is described by the parallel elastic element, which captures both extracellular and intracellular structures. Therefore, total passive stress $\sigma_{f,pas}(t)$ is the sum of extracellular matrix stress $\sigma_{f,ECM}(t)$ and intracellular stress, i.e. titin stress $\sigma_{f,tit}(t)$:

$$\sigma_{f,pas}(t) = \sigma_{f,ECM}(t) + \sigma_{f,tit}(t) \quad (3.2)$$

Extracellular matrix stress $\sigma_{f,ECM}(t)$ depends as follows on the total time-dependent sarcomere length $L_s(t)$, which is the sum of $L_{si}(t)$ and $L_{se}(t)$:

$$\sigma_{f,ECM}(t) = S_{f,pas} \cdot \left(\left(\frac{L_s(t)}{L_{s0,pas}} \right)^{k_{ECM}} - 1 \right) \tag{3.3}$$

Here, $S_{f,pas}$ is a parameter scaling passive stress development, while $L_{s0,pas}$ is the zero-passive stress sarcomere length. Parameter k_{ECM} determines the non-linearity of the relation. Titin stress $\sigma_{f,tit}(t)$ depends on $L_s(t)$, $S_{f,act}$, and two parameters which scale the development of titin stress ($k_{1,tit}$) and the non-linearity of the relation ($k_{2,tit}$):

$$\sigma_{f,tit}(t) = S_{f,act} \cdot k_{1,tit} \cdot \left(\left(\frac{L_s(t)}{L_{s0,pas}} \right)^{k_{2,tit}} - 1 \right) \tag{3.4}$$

3.2.2 Simulating ischemia-induced contractile dysfunction: one-compartment vs. two-compartment model

In a combined experimental and modeling study, Sunagawa et al. [19] showed that LV systolic function during regional ischemia was best captured by a two-compartment model including an active and a passive compartment. The rationale behind this two-compartment model is that the active compartment lumps all of the normally functioning tissue within the non-ischemic and ischemic region, while the passive compartment lumps all of the non-functional parts of the ischemic region. As mentioned before, we hypothesized that we could use a similar modeling approach not only for simulating global LV pump mechanics during regional ischemia, but also to simulate average regional LV tissue mechanics (i.e. myofiber stress and strain) in ischemic myocardial segments which are defined by deformation imaging techniques, for example speckle tracking echocardiography (STE). In the CircAdapt model, tissue properties are defined per myocardial patch, and by default each myocardial wall includes one myocardial patch. Active and passive stress of a patch is calculated using Equations 3.1-3.4. To simulate reduced patch contractility, one approach is to reduce parameter $S_{f,act}$ (Equation 3.1). Since this approach does not involve subdivision of the myocardial patch into multiple patches (i.e. compartments), we term this as a one-compartment modeling approach for simulating contractile dysfunction. For the two-compartment model of ischemia, the CircAdapt MultiPatch module [18] is applied. The MultiPatch module has previously been used to subdivide myocardial walls into different patches each having their own unique tissue properties [18,21,22]. In this study, we apply the MultiPatch module to further subdivide an ischemic myocardial patch with volume V_{patch} into a contractile and a non-contractile patch (i.e. compartment) with volumes V_C and V_{NC}, respectively (Figure 3.1). Compared to the implementation of Sunagawa et al. [19], where the subdivided volume V_{patch} equaled the volume of the entire LV wall, we additionally apply the two-compartment model on a regional level, where V_{patch} equals the volume of an echocardiographic segment by approximation. Mechanics of V_C are described by

Equations 3.1-3.4, while for V_{NC} it holds $S_{f,act} = 0$,, and therefore the mechanics of V_{NC} are fully described by Equation 3.3. The degree of patch contractile dysfunction is determined by the non-contractile volume fraction ($NCVF$), defined as the relative volume of the non-contractile compartment:

$$NCVF = \frac{V_{NC}}{V_{patch}} \tag{3.5}$$

3.2.3 Myofiber strain calculations

Calculated strain $\varepsilon(t)$ during the cardiac cycle represented engineering strain based on sarcomere length $L_s(t)$:

$$\varepsilon(t) = \left(\frac{L_s(t)}{L_{s,ref}} - 1\right) \cdot 100\% \tag{3.6}$$

where $L_{s,ref}$ is a reference sarcomere length used for strain calculations.

For the two-compartment model, sarcomere length $L_s(t)$ of V_{patch} was calculated as the volume-weighted average of the sarcomere lengths of the contractile and non-contractile compartments, respectively $L_{s,C}(t)$ and $L_{s,NC}(t)$:

$$L_s(t) = (1 - NCVF) \cdot L_{s,C}(t) + NCVF \cdot L_{s,NC}(t) \tag{3.7}$$

3.2.4 Simulation protocol

Global myocardial mechanics: one-compartment vs. two-compartment model

In line with the study of Sunagawa et al. [19], we compared simulated LV pump mechanics during acute regional ischemia when using a two-compartment model against a one-compartment model by constructing end-systolic pressure volume relations (ESPVRs). We started with a baseline reference simulation with heart rate of 71 bpm, stroke volume (SV) of 72 mL, and mean arterial pressure (MAP) of 92 mmHg. Homeostatic pressure-flow regulation was enabled, meaning that MAP and SV were kept constant through regulation of peripheral arterial resistance and circulating blood volume. First, for the two-compartment simulation, $NCVF$ was set to 0.2 in the LV free wall and septum to simulate 20% ischemia. Using the one-compartment model, $S_{f,act}$ in the LV and septal wall was gradually reduced until LV end-diastolic volume was similar as for the two-compartment simulation. Then, for both simulations of ischemia, as well as for the baseline simulation, afterload manipulations were done by increasing and reducing arterial resistance by 20% compared to the reference value while disabling pressure-flow regulation, thereby constructing an ESPVR. Zero-pressure volume (V_0) and slope (E_{max}) of the ESPVR were calculated.

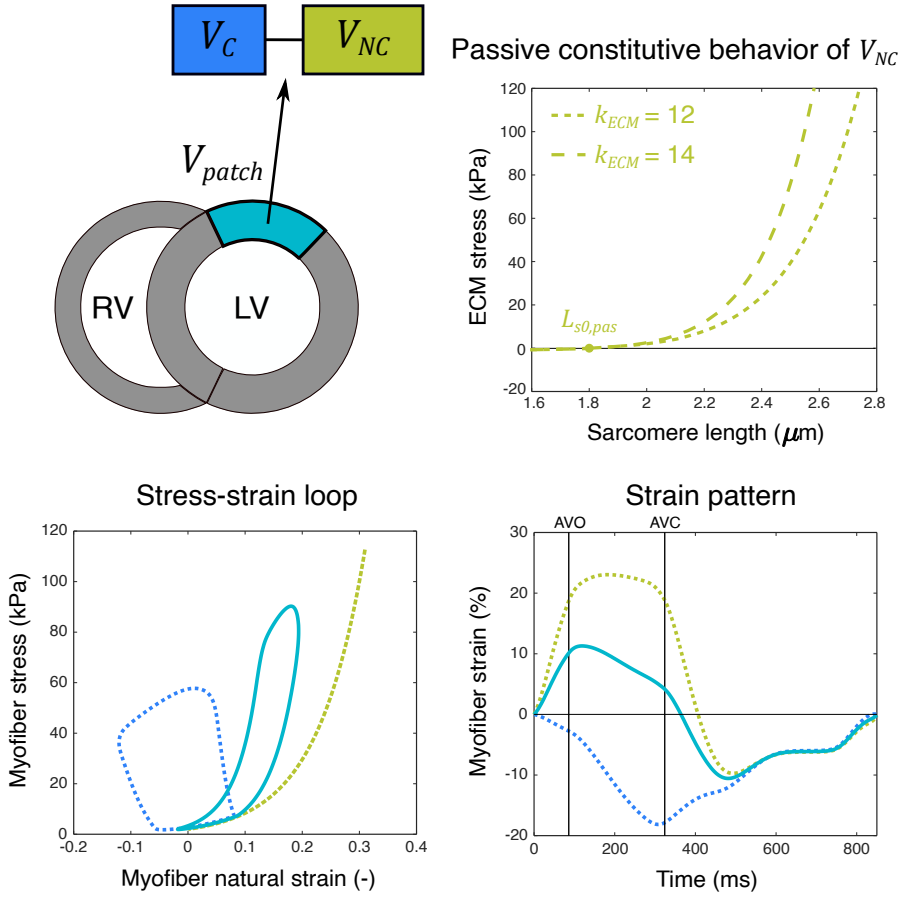

Figure 3.1: Schematic representation of the two-compartment modeling approach used for simulation of ischemic myocardial dysfunction. A myocardial patch with volume V_{patch} was subdivided into a hypothetical contractile and non-contractile patch (i.e. compartment) with volumes V_C and V_{NC}, respectively, being serially coupled (top left). Myocardial volume V_C generated active stress, while V_{NC} was passive (bottom left). Myocardial stiffness was determined by passive constitutive behavior of V_{NC}, determined by zero-passive stress sarcomere length ($L_{s0,pas}$) and non-linearity parameter (k_{ECM}) (top right). The resulting strain pattern of V_{patch} (bottom right) and its stress-strain loop (bottom left) were calculated from the volume-weighted average sarcomere length and stress of V_C and V_{NC}. AVO, aortic valve opening; AVC, aortic valve closure.

Regional myocardial mechanics: acute ischemia and reperfusion

We hypothesized that acute ischemia and subsequent reperfusion could realistically be simulated by manipulation of $NCVF$. To test this hypothesis, we used existing experimental data of regional myocardial deformation measured using sonomicrometry during acute 15-minute left anterior descending (LAD) coronary artery occlusion and subsequent reperfusion in a representative dog (Figure 3.4, upper panel) [23]. The ultrasonic crystals

used for sonomicrometry were implanted in the inner third of the myocardium of the anterior LV wall, aligned parallel with the LV long axis. We started with a baseline reference simulation with similar heart rate (105 bpm) as in the experiment, and we modified MAP to obtain similar LV peak systolic pressure (84 mmHg). Stroke volume was set to 49 mL to obtain a similar amplitude of segmental shortening as in the experiment. Starting from the baseline simulation, we simulated 15 minutes of LAD occlusion by increasing $NCVF$ from 0 to 1 in a myocardial region which occupied 30% of total LV wall volume and which was proportionally distributed over the septum and LV free wall. Assuming that the experimental ultrasonic crystals were placed entirely in the anterior LV wall, strain and segment lengths in the model were calculated within the dysfunctional region located in the LV free wall. Sarcomere length L_s in the model was translated to measured segment length SL by multiplying L_s with a constant, calculated from the difference between simulated end-diastolic L_s ($L_{s,ED}$) and experimentally reported end-diastolic segment length ($SL_{exp,ED}$) in the baseline reference situation:

$$SL = L_s \cdot \frac{L_{s,ED}(baseline)}{SL_{exp,ED}(baseline)} \tag{3.8}$$

Parameters $L_{s0,pas}$ and k_{ECM} of V_{NC} (Equation 3.3) were tuned to represent the experimental condition after 15 minutes of ischemia, i.e. with similar end-diastolic segment length and systolic stretch amplitude. Starting from the simulation of 15-minute LAD occlusion, we reduced $NCVF$ from 1 to 0 with steps of 0.2 to simulate contractile recovery after reperfusion.

Regional myocardial mechanics: prolonged ischemia and reperfusion

To evaluate whether the two-compartment model could also accurately simulate regional mechanics in ischemic dysfunction with increased stiffness, potentially indicating MI, we attempted to calibrate parameters $L_{s0,pas}$ and k_{ECM} to experimental data of regional myocardial deformation obtained after 4 hours of LAD occlusion followed by reperfusion [23]. We first calibrated the baseline reference simulation by setting heart rate to the experimentally measured value of 111 bpm and tuning MAP such that simulated peak LV systolic pressure was 91 mmHg. Stroke volume was set to 41 mL to obtain a similar amplitude of segmental shortening as in the experiment. Then, we again simulated acute anteroseptal ischemia occupying 30% of total LV wall volume, with $NCVF$=1 and values for $L_{s0,pas}$ and k_{ECM} tuned such that end-diastolic segment length and systolic stretch amplitude were similar between model and experiment. Starting from this simulation of acute ischemia, we modified k_{ECM} until segmental systolic stretch in the model matched the reported stretch after 4 hours of ischemia. We further modified k_{ECM} to obtain a similar systolic stretch as measured after 15 minutes of subsequent reperfusion. In both simulations, $L_{s0,pas}$ was tuned to obtain similar end-diastolic segment lengths between model and experiment.

3.2.5 Patient-specific $NCVF$ estimation

Patient cohort

Six patients were selected from the DEFI-MI (DEtection of cardiac FIbrosis by LGE magnetic resonance imaging (MRI) and circulating biomarkers in patients with Myocardial Infarction) cohort. This was a prospective study on first-time MI patients, approved by the local ethics committee (METC: NL45241.041.13) and in accordance with the declaration of Helsinki. Patients in this study were included after an acute MI where urgent revascularization was performed. From the measured cohort, we selected patients with narrow QRS (<120 ms) who had a minimum infarct size of 10% of LV wall mass and a minimum relative LGE percentage of 25% in at least one myocardial AHA segment.

Echocardiographic measurements

Echocardiography was performed at baseline (i.e. within 72 hours after admission) and at 6-month follow-up using a commercially available system (Vivid E9, GE Vingmed Ultrasound AS, Horten, Norway). LV volumes and ejection fraction (EF) were acquired by Simpson's biplane method. Focused loops of the apical four-chamber view, two-chamber view, and three-chamber view were stored for post-processing (GE EchoPAC version 203). Speckle tracking deformation imaging of the LV was performed in 18 segments according to current clinical standards while blinded to the MRI results [22].

Cardiac magnetic resonance

At a median of six months after primary MI, all patients underwent contrast-enhanced 1.5 Tesla cardiac magnetic resonance (CMR) imaging (Philips Healthcare, Best, The Netherlands). LGE image acquisition was performed 15 minutes after administration of 0.2 ml/kg gadobutrol (Gadovist, Bayer Vital GmbH, Leverkusen, Germany), using prospective ECG-gated sequences of the short axis views from base to apex, with 5mm slice-thickness. Images were analyzed off-line using Philips ISP9 software (Philips Healthcare, Best, The Netherlands). Using the RV insertion points to the interventricular septum as anatomical landmarks, the heart was subdivided into 16 segments according to the model of the American Heart Association (AHA) [24], excluding the apical cap. LGE was quantitatively assessed using the full width at half maximum (FWHM) method, providing a percentage for each of the analyzed segments, as well as the total infarct (scar) size (global %) of the whole LV.

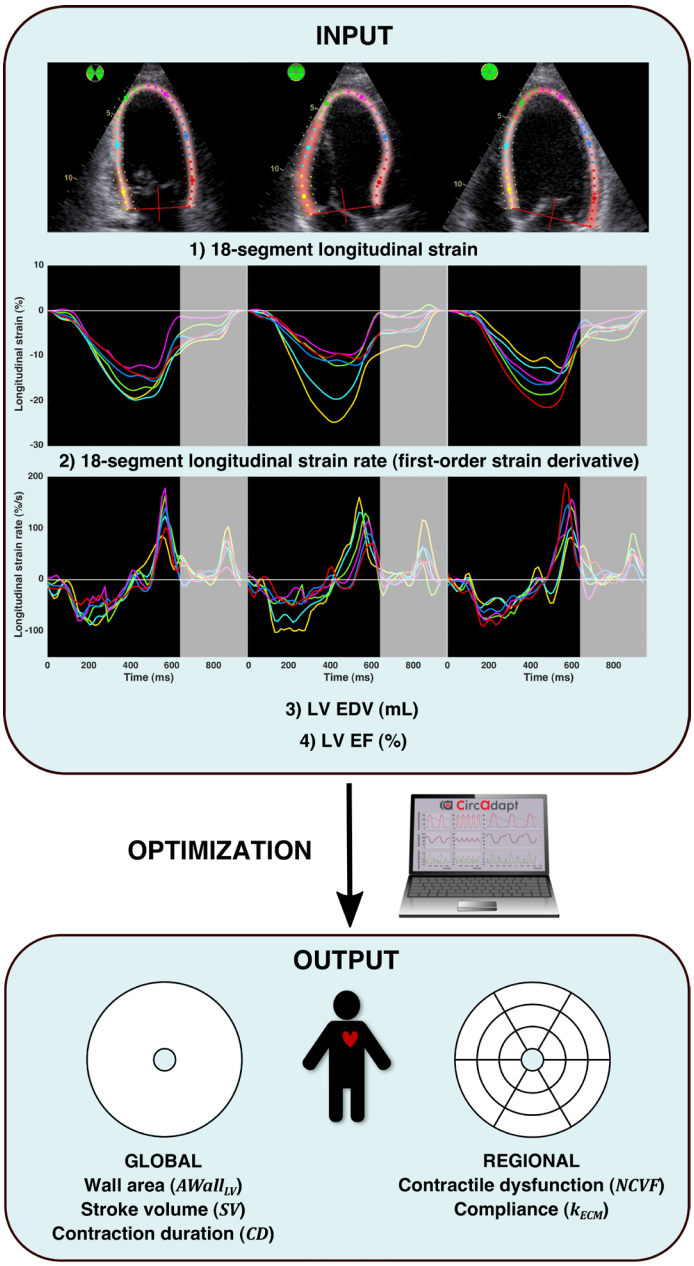

Figure 3.2: Patient-specific parameter estimation protocol. The input of the optimization algorithm (INPUT) consisted of 1) 18-segment longitudinal strain, 2) 18-segment longitudinal strain rate (calculated as first-order time derivative of strain), 3) LV end-diastolic volume (EDV), and 4) LV ejection fraction (EF). Strain and strain rate signals were analyzed until early diastole, as indicated by the grey-enhanced parts of the strain and strain rate signals. For numerical optimization (OPTIMIZATION), a multi-swarm particle swarm optimization (MSPSO) algorithm similar as previously described in van Osta et al. [25] was run which estimated (OUTPUT): global LV wall area, global stroke volume, global ventricular contraction duration, regional contractile dysfunction, and regional compliance.

Optimization algorithm

To estimate $NCVF$ on a segmental level, we used a multi-swarm particle swarm optimization (MSPSO) algorithm as previously described by van Osta et al. [25]. MSPSO is a stochastic optimization algorithm which is highly suitable for non-linear optimization problems. A brief description of the optimization algorithm will be provided here, for further methodological details we refer to van Osta et al. [25]. As an input to the optimization algorithm, we used four different echocardiographic measurements (Figure 3.2, INPUT): 1) 18-segment longitudinal strain, 2) 18-segment longitudinal strain rate, calculated as first-order time-derivative of the strain signal, 3) LV end-diastolic volume (EDV), and 4) LV ejection fraction (EF). All four components were normalized in the objective function based on their expected measurement uncertainty, and simulated strains were also scaled to match global strain amplitude between simulation and measurement. Strain and strain rate signals were analyzed until a pre-defined time point within the diastolic phase, defined as 10% of the cycle time after the moment of 10% global re-lengthening (i.e. global longitudinal strain (GLS) becomes less than 90% of its maximal value). Late diastolic strain was thereby neglected, considering the effects of e.g. drift compensation. Within the time interval analyzed, the sum of squared errors (SSE) between model and measurement was calculated, and SSE was corrected for the number of time points. Parameters estimated in the model (Figure 3.2, OUTPUT) included regional $NCVF$ and k_{ECM}, as well as global LV wall area $A_{wall,LV}$, global ventricular contraction duration CD and stroke volume SV. Parameter estimation (Figure 3.2, OPTIMIZATION) was initiated by performing 1000 quasi-random Monte Carlo (MC) simulations with heart rate (HR) set to the measured value. For each MC simulation, the objective function was calculated and in addition for each individual segment an error was calculated as the sum of error in segmental strain and strain rate. A total of 40 initial candidate solutions were selected, which were the best 20 MC simulations based on the objective function and 20 random combinations of the best 20 segmental parameter sets (i.e. $NCVF$ and k_{ECM}) based on segmental error. Subswarms were reassigned every 40 iterations, and MSPSO was stopped when either all particles had normalized energy < 10^{-4}, meaning that within one iteration all parameters changed by less than 1% of the width of their MC sampling domain, or a maximum number of 1000 iterations was reached.

Model implementation

The CircAdapt model as used in this study has been published before in more detail [18]. To reduce computational cost, a C++ implementation of this version was used as published before [26]. Equations were linearized using the Newton–Raphson method and 61 ordinary differential equations were time-integrated using the Adams–Bashford method with a variable timestep Δt with $\max(\Delta t) = 2$ ms. MSPSO was performed in Matlab 2019a (MathWorks, Natick, MA, USA). Simulations ran in parallel on an AMD Ryzen Threadripper 3970X.

3.3 RESULTS

3.3.1 Global myocardial mechanics: one-compartment vs. two-compartment model

Constructed ESPVRs for the one- and two-compartment simulations of LV acute regional ischemia are shown in Figure 3.3. Associated values of V_0 and E_{max} are provided in Table 3.1. Compared to the baseline simulation, E_{max} (2.07 mmHg/mL) was moderately reduced for the two-compartment simulation (1.21 mmHg/mL), but it was severely reduced for the one-compartment simulation (0.45 mmHg/mL) of regional ischemia. Furthermore, with respect to the baseline V_0 (13.2 mL), V_0 was increased for the two-compartment simulation (46.7 mL), consistent with a rightward shift of the ESPVR, while the one-compartment simulation demonstrated a reduction of V_0 to -102.4 mL.

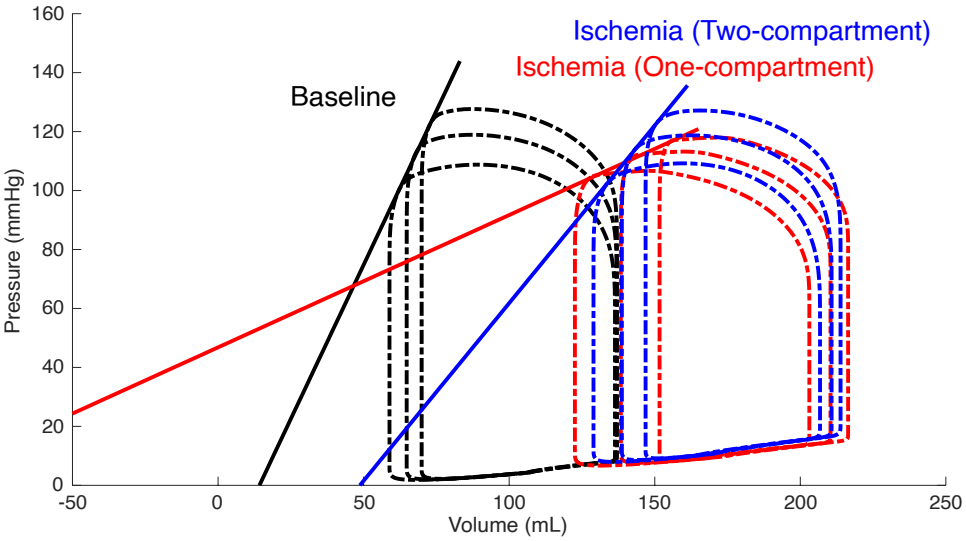

Figure 3.3: Simulated left ventricular (LV) end-systolic pressure-volume relations (ESPVRs) for a baseline healthy LV (black loops and line), and for an ischemic LV affecting 20% of LV wall mass modeled by a two-compartment approach (blue loops and line) and a one-compartment approach (red loops and line). ESPVRs were constructed by afterload manipulations through reducing and increasing arterial resistance by 20% compared to the reference resistance. The two-compartment simulation of ischemia demonstrated a rightward shift of the ESPVR with a moderate reduction in slope, while the one-compartment simulation demonstrated a severe reduction in both slope and zero-pressure volume.

Table 3.1: Characteristics of the left ventricular (LV) end-systolic pressure-volume relation (ESPVR)

	V_0 (mL)	E_{max} (mmHg/mL)
Baseline	13.2	2.07
Ischemia (One-compartment)	-102.4	0.45
Ischemia (Two-compartment)	46.7	1.21

3.3.2 Regional myocardial mechanics: acute ischemia and reperfusion

Simulated LV pressure-segment length loops and corresponding strain patterns at baseline ($NCVF$=0) and during acute ischemia ($NCVF$=1) were successfully calibrated using the experimental measurements (Figure 3.4 and 3.5, respectively). Calibrated parameter values are provided in Table 3.2, and demonstrated an increase of $L_{s0,pas}$ and k_{ECM} during acute ischemia with respect to baseline. Starting from this simulation of acute ischemia, a reduction of $NCVF$ shifted the LV pressure-segment length loop leftward, i.e. back towards the baseline loop, while loop area increased. The loops and strain patterns for $NCVF$ values of 0.4 and 0.2 were similar to the measured loops and strain patterns after 15 minutes and 3 hours of reperfusion, respectively (Figure 3.4-3.5).

3.3.3 Regional myocardial mechanics: prolonged ischemia and reperfusion

When starting from the calibrated simulation of acute ischemia, increasing k_{ECM} led to a reduced amplitude of segmental systolic stretch, while also shifting the LV pressure-segment length loop leftward (Figure 3.6-3.7). Calibration of parameters $L_{s0,pas}$ and k_{ECM} demonstrated that a further increase of both $L_{s0,pas}$ and k_{ECM} was needed to reproduce the measured loop after 4 hours of ischemia (Table 3.3), while a reduction of $L_{s0,pas}$ combined with a further increase of k_{ECM} was needed to reproduce the data after 15 minutes of subsequent reperfusion.

3.3.4 Patient-specific $NCVF$ estimation

Patient characteristics are summarized in Table 3.4. Results of the patient-specific estimation of $NCVF$ for two different patients (PATIENT 1 and 2) are shown in Figures 3.8 and 3.9, respectively. For all four other patients, results are shown in the Supplementary Material section. In both PATIENT 1 and 2, it can be noted that estimated $NCVF$ values were increased in segments with increased systolic stretch or reduced peak systolic strain, both at baseline and 6-month follow-up. In the acute phase after MI, PATIENT 1 (Figure 3.8) demonstrated a localized area of increased $NCVF$ in the anterior, anteroseptal, and inferoseptal segments, extending from the base all the way into the apex. At 6-month follow-up, LGE revealed presence of scar tissue within the same area, especially in the apical septal and mid-ventricular anterior and anteroseptal regions. While increased segmental $NCVF$ values remained after six months, $NCVF$ in the anterior, anteroseptal, and inferoseptal segments were lower than at baseline. This functional improvement over time was also reflected by an increase of LVEF from 30% at baseline to 49% at 6-month follow-up. In PATIENT 2 (Figure 3.9), increased values of $NCVF$ at baseline were found especially in the apical anterior and septal segments, but it was extended into the mid-ventricular and basal segments. At 6-month follow-up, while the size of the region with increased $NCVF$ was reduced, severe contractile dysfunction remained in the apex and mid-ventricular anteroseptal region. LGE revealed presence of a large, transmural scar in this area. Analysis of all 22 myocardial segments with LGE>25% at 6-month follow-up revealed that in most segments

(68%) $NCVF$ was higher at baseline than after six months (Figure 3.10). At baseline, 21 (95%) segments had $NCVF$>25% and 12 (55%) had $NCVF$>50%, while at 6-month follow-up, 15 (68%) segments had $NCVF$>25% and 6 (27%) had $NCVF$>50%. Average segmental $\Delta NCVF$ between baseline and 6-month follow-up was -16.1 ± 21.8%.

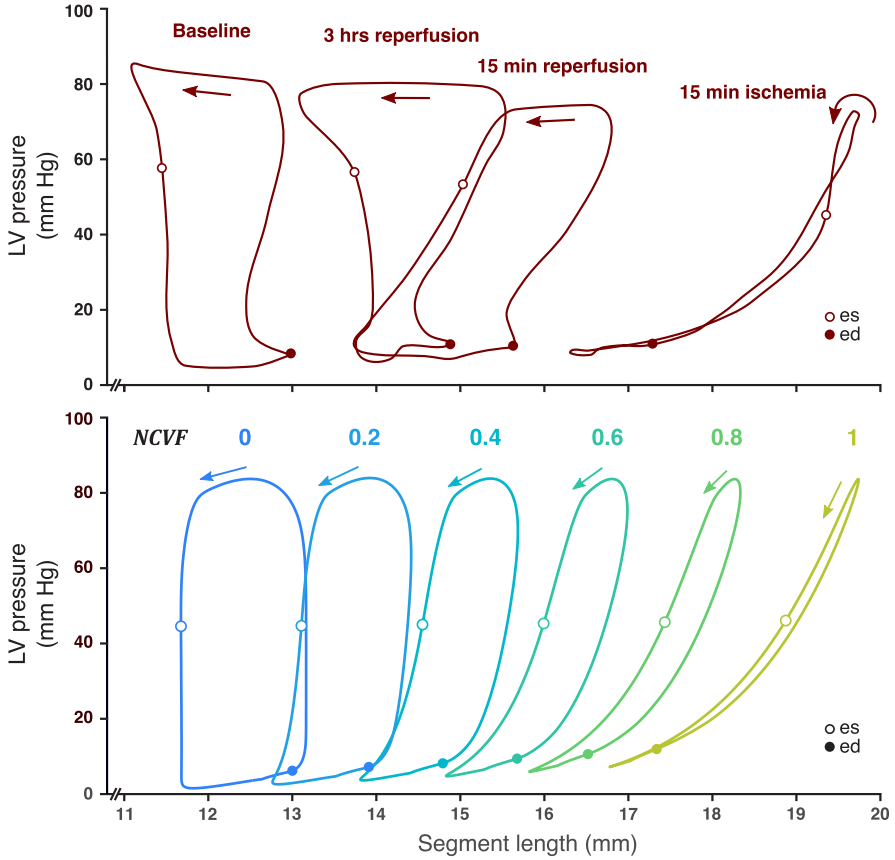

Figure 3.4: Comparison between measured LV pressure-segment length loops in a representative dog after 15 min of left anterior descending (LAD) coronary artery occlusion followed by 15 min and 3 h of reperfusion (upper panel, resketched from Lyseggen et al. [23]) and simulated LV pressure-segment length loops (lower panel) for varying regional contractile dysfunction ($NCVF$). ed, end-diastole; es, end-systole.

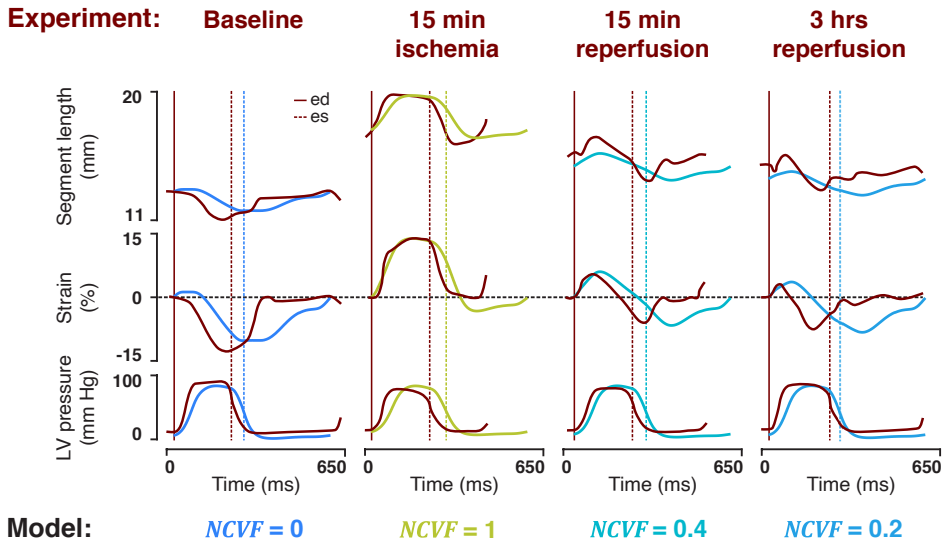

Figure 3.5: Comparison between the temporal behavior of measured segment length, strain, and LV pressure in the same representative dog as in **Figure 3.4** after 15 min of left anterior descending (LAD) coronary artery occlusion followed by 15 min and 3 h of reperfusion (dark red tracings, resketched from Lyseggen et al. [23]) and simulated segment length, strain and LV pressure (blue and green tracings) for the best matching severities of regional contractile dysfunction ($NCVF$). ed, end-diastole; es, end-systole.

Table 3.2: Calibrated parameter values for the simulations of acute ischemia and reperfusion.

	$NCVF$ (-)	$L_{s0,pas}$ (μm)	k_{ECM} (-)
Baseline	0	1.75*	10*
15 min ischemia	1	2.21	17
15 min reperfusion	0.4	2.21	17
3 hrs reperfusion	0.2	2.21	17

*Since $NCVF = 0$, values of $L_{s0,pas}$ and k_{ECM} represent those of the contractile compartment V_c

Table 3.3: Calibrated parameter values for the simulations of acute ischemia, prolonged ischemia and reperfusion.

	$NCVF$ (-)	$L_{s0,pas}$ (μm)	k_{ECM} (-)
Baseline	0	1.75*	10*
15 min ischemia	1	2.01	26
4 hrs ischemia	1	2.19	70
15 min reperfusion	1	2.03	120

*Since $NCVF = 0$, values of $L_{s0,pas}$ and k_{ECM} represent those of the contractile compartment V_c

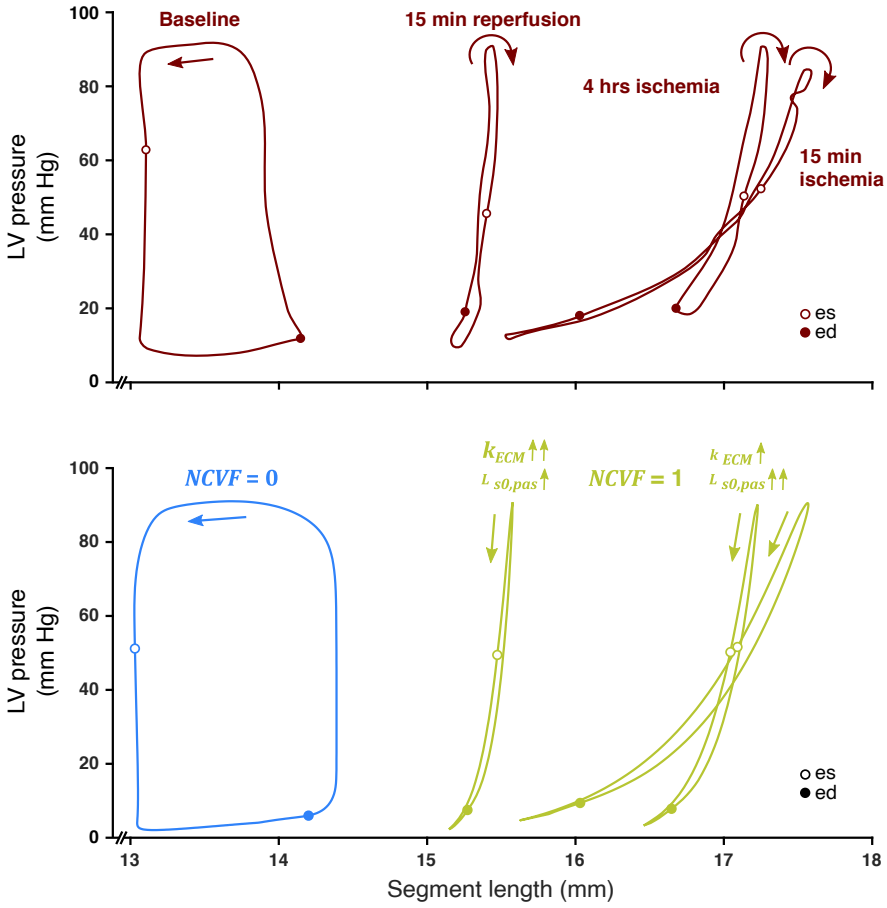

Figure 3.6: Comparison between measured LV pressure-segment length loops in a representative dog after 15 min and 4 h of left anterior descending (LAD) coronary artery occlusion, followed by 15 min of reperfusion (upper panel, resketched from Lyseggen et al. [23]) and simulated LV pressure-segment length loops (lower panel) for no contractile dysfunction ($NCVF$ = 0, blue loop), and complete contractile dysfunction ($NCVF$ = 1, all three green loops), where nonlinearity parameter (k_{ECM}) and zero-stress sarcomere length ($L_{s0,pas}$) were calibrated for the green loops to mimic the experimental measurements (values can be found in **Table 3.3**). ed, end-diastole; es, end-systole.

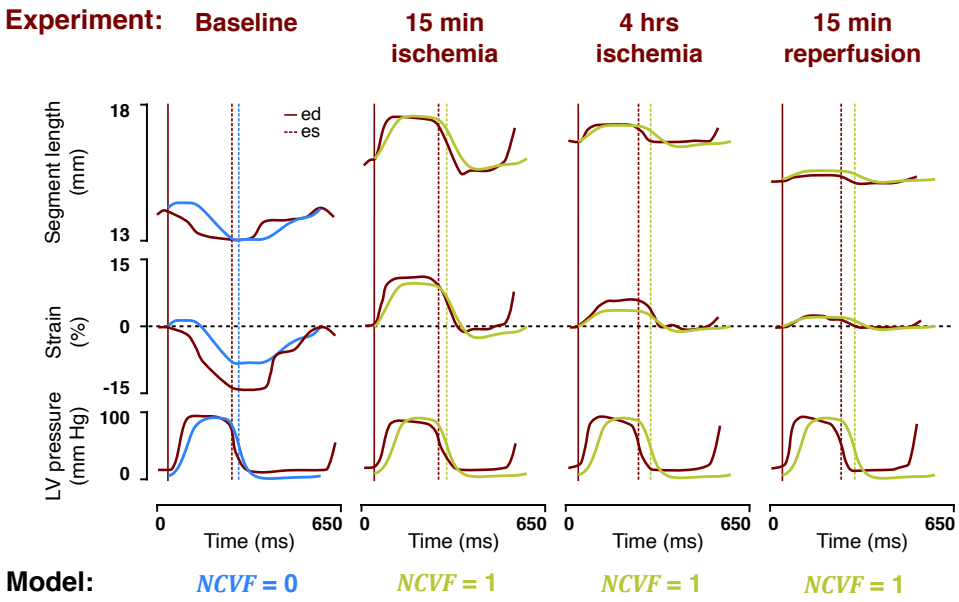

Figure 3.7: Comparison between the temporal behavior of measured segment length, strain, and LV pressure in the same representative dog as in **Figure 3.6** after 15 min and 4 h of left anterior descending (LAD) coronary artery occlusion, followed by 15 min of reperfusion (dark red tracings, resketched from Lyseggen et al. [23]) and the simulated segment length, strain and LV pressure (blue and green tracings) for no contractile dysfunction ($NCVF$ = 0) and for three simulations of complete contractile dysfunction ($NCVF$ = 1) with calibrated values of the nonlinearity parameter (k_{ECM}) and zero-stress sarcomere length ($L_{s0,pas}$). ed, end-diastole; es, end-systole.

Table 3.4: Patient characteristics of the selected DEFI-MI subcohort

n	6 (83% male)
Age at baseline (years)	57.6 ± 9.5
Relative infarct size (% of LV wall mass)	16 ± 6
QRS duration baseline (ms)	90 ± 11
LVEF baseline (%)	49.8 ± 11.5
LVEDV baseline (mL)	100 ± 31
QRS duration 6-month follow-up (ms)	92 ± 13
LVEF 6-month follow-up (%)	50.5 ± 3.5
LVEDV 6-month follow-up (mL)	98 ± 25

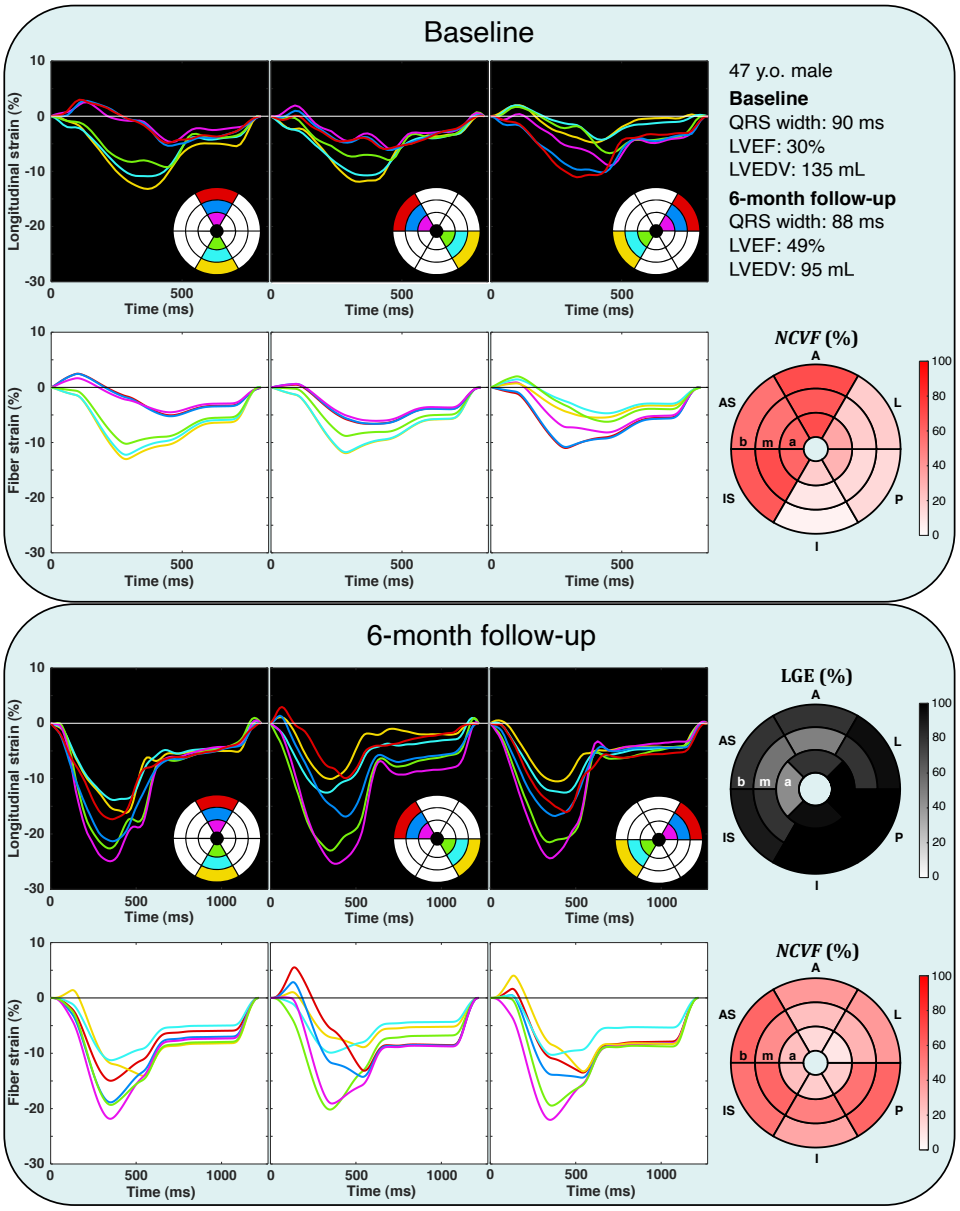

Figure 3.8: Echocardiographic strain measurements (black panels) and simulated strain patterns obtained using an optimization algorithm (white panels) at baseline and 6-month follow-up in one patient from the DEFI-MI subcohort (PATIENT 1, a 47-year-old male). Estimated $NCVF$ values at baseline were higher in the anterior (A), anteroseptal (AS), and inferoseptal (IS) wall segments than in the rest of the heart. After six months, scar tissue was found in the same area using late gadolinium enhancement (LGE). Although contractile dysfunction remained at 6-month follow-up, $NCVF$ values in the A, AS and IS segments were lower. I, inferior; P, posterior; L, lateral; b, base; m, mid-ventricle; a, apex.

3.4 DISCUSSION

In this computational study, we used the CircAdapt model of the human heart and circulation to test the ability of a lumped two-compartment model to realistically simulate the effects of ischemia-induced contractile dysfunction on ventricular pump and myocardial tissue mechanics. The modeling approach was first evaluated on the level of global LV mechanics by constructing ESPVRs at baseline and during acute regional ischemia using simulations with a two- and one-compartment modeling approach. Then, simulated regional strains and pressure-length loops for increasing degrees of contractile dysfunction were compared with existing gold standard myocardial deformation measurements in dogs with acute and prolonged ischemia followed by reperfusion. Finally, patient-specific optimizations were performed to estimate the non-contractile volume fraction $NCVF$ in a small cohort of MI patients in the acute and chronic phase after MI, and estimated values were compared with LGE percentages after six months. Our results demonstrated that 1) global LV mechanics during regional ischemia were more realistically simulated by the two-compartment than the one-compartment model, 2) manipulation of $NCVF$ alone could reproduce the experimental deformation data of acute ischemia and subsequent reperfusion, while additional increases of myocardial stiffness were needed to reproduce the deformation data during prolonged ischemia followed by reperfusion, and 3) the patient-specific simulations further supported the idea that this modeling approach can potentially be used for strain-based estimation of regional myocardial contractile dysfunction in patients with cardiovascular disease.

3.4.1 Two-compartment model realistically simulates global LV mechanics

Constructed LV ESPVRs at baseline and during acute regional ischemia using both a one- and two-compartment modeling approach demonstrated that E_{max} was much less affected when a two-compartment model was used (Figure 3.3, Table 3.1). This result was expected and is in line with the observations of Sunagawa et al. [19]. While in their study they found no reduction in E_{max} for an ischemic region size of 20%, however, our simulation demonstrated a reduction of E_{max} from 2.07 mmHg/mL to 1.21 mmHg/mL. This lower value of E_{max} in our simulation was likely caused by the relatively compliant passive tissue constitutive behavior, determined by the value of parameter k_{ECM} (Equation 3.3). When increasing k_{ECM}, the non-linearity of the passive stress-sarcomere length relation increases which causes stiffer passive tissue behavior, thereby increasing E_{max}. This effect of infarct stiffness on LV systolic function was also previously demonstrated in a modeling study by Fomovsky et al. [1]. We note that, at the same time, as a result of the parameterization of passive tissue behavior, the change in V_0 with respect to baseline (+33.5 mL) was more pronounced in our two-compartment model than in the experimental observations, where it was approximately +10 mL for an ischemic region size of 20% [19]. Qualitatively, however, a similar rightward shift of the ESPVR was observed. The one-compartment simulation of acute regional ischemia demonstrated a severe reduction of V_0 to a value of -102.4 mL, which is not consistent with

experimental observations.

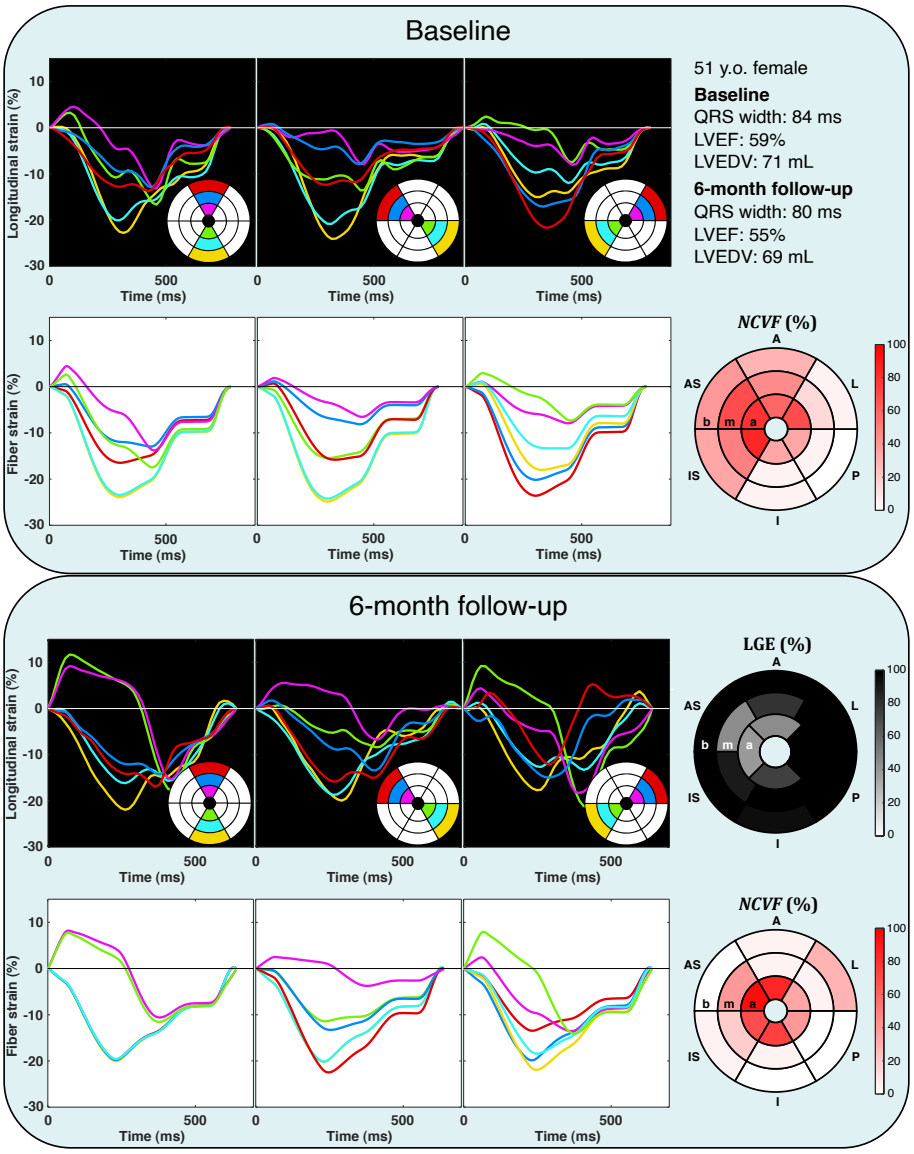

Figure 3.9: Echocardiographic strain measurements (black panels) and simulated strain patterns obtained using an optimization algorithm (white panels) at baseline and 6-month follow-up in one patient from the DEFI-MI subcohort (PATIENT 2, a 51-year-old female). Estimated $NCVF$ values at baseline were higher in the anterior (A), anteroseptal (AS), and inferoseptal (IS) wall segments, as well as in the apical (a) inferior (I), posterior (P), and lateral (L) wall segments, than in the rest of the heart. After six months, scar tissue was found using late gadolinium enhancement (LGE) in part of this dysfunctional area, extending from the apex into the mid-ventricular (m) anteroseptal segment. Increased values of $NCVF$ were remained in these scarred segments. b, base.

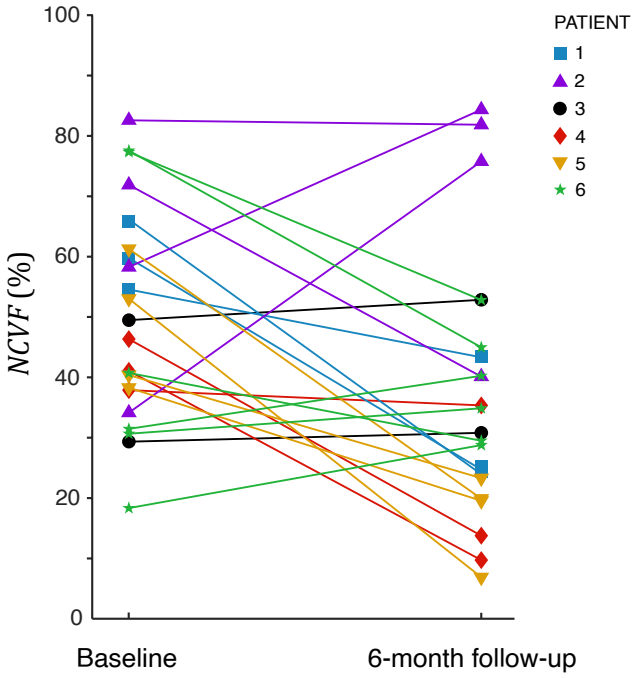

Figure 3.10: Estimated $NCVF$ values at baseline and 6-month follow-up in all 22 segments with LGE>25% at 6-month follow-up. Different symbol-color-combinations indicate different patients, as shown in the legend. The majority of segments (68%) demonstrated a reduction of $NCVF$ at 6-month follow-up with respect to baseline. Results for PATIENT 1 and PATIENT 2 are also shown in **Figures 3.8** and **3.9**, respectively. Results for PATIENTS 3-6 are shown in the Supplementary Material section.

3.4.2 Two-compartment model reproduces regional mechanics during acute ischemia and reperfusion

Simulated strain patterns and LV pressure-segment length loops for $NCVF$ values of 1, 0.4, and 0.2 qualitatively agreed with the experimental data of acute ischemia followed by 15 minutes and 3 hours of reperfusion, respectively (Figure 3.4-3.5). While parameters $L_{s0,pas}$ and k_{ECM} were calibrated for the simulation of $NCVF$=1 to match reported end-diastolic segment length and systolic stretch amplitude during acute ischemia, contractile recovery was simulated by reducing $NCVF$ without further modifying $L_{s0,pas}$ and k_{ECM} (Table 3.2). This result supports $NCVF$ as a parameter quantifying the degree of contractile dysfunction. Calibrated parameter values for the simulation of acute ischemia demonstrated that $L_{s0,pas}$ and k_{ECM} were increased with respect to their baseline values. Increases in $L_{s0,pas}$ during acute ischemia have been reported in previous studies which have found that ischemic tissue dimensions were larger at matched pressures [27]. Adding to the discussion of the previous paragraph, the relatively large increase in k_{ECM} during acute ischemia with respect to baseline may indicate an inadequate parameterization of k_{ECM} in the baseline simulation, causing the myocardium to be too compliant. While immediate increases in tissue stiffness

during acute ischemia have been reported [28], an acute effect of ischemia on tissue passive constitutive behavior has not clearly been established [29]. The data showed that after 3 hours of reperfusion following acute ischemia, contractile recovery was still incomplete, which was confirmed by our simulations which demonstrated a good agreement with the data for $NCVF$=0.2. This persistent dysfunction which follows reperfusion after a short-term period of ischemia has been attributed to myocardial stunning [30]. While it is known that stunning involves complex abnormalities at the cellular level including decreased calcium responsiveness [31], which are not explicitly described in our model, parameter $NCVF$ captured the mechanics during stunning relatively well.

3.4.3 Two-compartment model reproduces regional mechanics during prolonged ischemia and reperfusion

Our simulations of prolonged ischemia and subsequent reperfusion demonstrated that k_{ECM} was increased between 15 minutes and 4 hours of ischemia and was even further increased after 15 minutes of subsequent reperfusion (Figure 3.6-3.7, Table 3.3). This increased stiffness during prolonged ischemia and reperfusion is in agreement with measurements of compliance performed in the experiment, and was linked to tissue edema as reflected by increased myocardial water content [23]. The occurrence of interstitial edema and associated increases of myocardial stiffness during the necrotic phase have also been suggested in other studies [29]. At the same time, $L_{s0,pas}$ was increased between our simulations of 15 minutes and 4 hours of ischemia, which may indicate early infarct expansion [29]. For the simulation of subsequent reperfusion, however, $L_{s0,pas}$ was again reduced, potentially indicating compaction of the necrotic region during the infarct healing process.

3.4.4 $NCVF$ as measure of ischemia-induced contractile dysfunction

Parameter $NCVF$ is defined in the model as the relative volume of the non-contractile compartment, and increasing $NCVF$ therefore leads to increased contractile dysfunction. In the experimental dataset of acute ischemia and subsequent reperfusion, contractile recovery occurred, which was reflected by a reduction of $NCVF$ in the model. In the dataset of prolonged ischemia and reperfusion, however, there was no contractile recovery, and contractile dysfunction remained at the same level ($NCVF$ = 1). Similarly, the patient-specific $NCVF$ estimations demonstrated that this parameter was increased in segments with systolic stretching or reduced peak systolic strain. Interestingly, in this patient cohort, among all segments with LGE>25% six months after MI, $NCVF$ values decreased substantially in most segments from baseline to 6-month follow-up (Figure 3.10), suggesting partial recovery of myocardial contractile function over time. A possible explanation for this observed contractile recovery in the majority of segments is that most segments had non-transmural infarction at 6-month follow-up (LGE<50%), and non-transmural infarcts have been associated with functional recovery following revascularization [32]. Increased

values of $NCVF$ were found especially in segments with LGE>25% after six months, but were not limited to those LGE-positive segments. It is likely that non-scarred segments with increased $NCVF$ in the acute phase after MI were dysfunctional due to myocardial stunning [30]. Increased $NCVF$ values in non-scarred regions at 6-month follow-up could potentially be related to adverse myocardial remodeling. When we compare our obtained strain data and $NCVF$ estimations with other modeling [5] and clinical studies [33-37] of strain in MI, we notice a common finding that transmural MI causes significant transmural strain abnormalities, including systolic stretching, a reduction of peak systolic strain, and post-systolic shortening. For subendocardial MI, Leong et al. [5] found in their model that strain was affected in the subendocardial layers, but that mid-myocardial and subepicardial strains were preserved. A similar conclusion was reached in a clinical study by Becker et al. [35], who showed that non-transmural infarction led to greater functional impairment of the endocardial than of the epicardial layer. While this transmural heterogeneity in function may exist, multiple studies using strain or strain rate imaging have successfully differentiated subendocardial MI from normal myocardium [33,34] and thereby suggest that abnormal strains can be found in segments with subendocardial MI. The same suggestion holds for segments adjacent to an MI region, which have been shown to have lower peak strain than segments remote from MI [38]. From these and our own observations we conclude that $NCVF$ is a functional parameter which effectively indicates the degree of ischemia-induced contractile dysfunction and that therefore its use could enhance current diagnostics in patients with cardiovascular disease. At the same time, however, $NCVF$ alone seems to be unable to differentiate between underlying types of ischemic dysfunction and therefore it is not suitable to replace LGE. Rather, it could provide useful diagnostic information on its own or it could be used in addition to LGE.

3.4.5 Limitations

The experimental measurements of Lyseggen et al. [23] used in our study were acquired by ultrasonic crystals which were aligned parallel to the LV long axis, thereby closely resembling LV longitudinal strain. In our model, however, we use the one-fiber model to simulate myofiber strain within a spherical LV geometry, and therefore there can be a systematic discrepancy between simulated and experimental strain values. In the patient-specific optimizations, we corrected for this model discrepancy by normalization of measured and simulated strains to global strain amplitude, but global strain values were not measured in the experiment and hence no correction was performed. However, the temporal behavior of the experimental and simulated strains was similar and we therefore expect that this potential mismatch could have had consequences for the quantitative values of calibrated parameters, but that qualitative results remained unaffected. We also assumed that the measurements were obtained from the anterior portion of the LV free wall, implying that we compared these data to simulated strains in the ischemic region located within the LV free wall, thereby disregarding septal deformation. This assumption, if not fully valid, could additionally have

caused a minor mismatch in the strain data between model and experiment. Furthermore, a sensitivity analysis (data not shown) demonstrated that correlations between $NCVF$ and passive material properties ($L_{s0,pas}$ and k_{ECM}) are very small or even absent and that $NCVF$ is the parameter that most significantly determines contractile function. Since $L_{s0,pas}$ and k_{ECM} are parameters which are modified in the non-contractile compartment only, they merely modify end-diastolic sarcomere length and amplitude of systolic stretch, respectively, of the non-contractile compartment, thereby not impacting intrinsic myocardial contractility. Future research is needed to investigate whether and how $L_{s0,pas}$ and k_{ECM} are identifiable from regional strain measurements. The patient data used for this study were retrospectively obtained, and no arterial pressure measurements were available. We assumed that none of the patients had hypertension and we set pressures in the model to default values. Since strain is known to depend on pre- and afterload [39-41], this assumption on the patients' blood pressures could have influenced the strain signals. Furthermore, in our optimization protocol, the number of estimated parameters was limited. We did not estimate for example the timing of mechanical activation, which potentially could also differ regionally in patients with MI due to slower electrical conduction in scar tissue [27]. Future research is required to determine whether the set of estimated parameters was sufficient or could potentially be improved. In addition, we only used systolic and early diastolic strain for optimization in this study since we considered late diastolic strain to be relatively inaccurate due to the effects of e.g. drift compensation. While we believe that the strain interval used is large enough for estimating the relevant parameters in this study, future studies could evaluate whether late diastolic strain adds relevant information to the objective function.

3.5 CONCLUSION

We successfully used a two-compartment model for simulation of ventricular pump and myocardial tissue mechanics in ischemic heart disease. Patient-specific optimizations using regional myocardial deformation successfully estimated $NCVF$ in a small cohort of MI patients in the acute and chronic phase after MI while estimated $NCVF$ values closely approximated the extent of myocardial scar at follow-up. In future studies, this approach can facilitate deformation imaging-based estimation of myocardial tissue properties in patients with cardiovascular disease.

REFERENCES

1. Fomovsky GM, Macadangdang JR, Ailawadi G, Holmes JW (2011). Model-based design of mechanical therapies for myocardial infarction. *J. Cardiovasc. Transl. Res.* 4(1), 82-91.
2. Fomovsky GM, Rouillard AD, Holmes JW (2012). Regional mechanics determine collagen fiber structure in healing myocardial infarcts. *J. Mol. Cell. Cardiol.* 52(5), 1083-1090.
3. Rouillard AD, Holmes JW (2014). Coupled agent-based and finite-element models for predicting scar structure following myocardial infarction. *Prog. Biophys. Mol. Biol.* 115(2-3), 235-243.
4. Veress AI, Fung GSK, Lee TS, Tsui BMW, Kicska GA, Segars WP, Gullberg GT (2015). The direct incorporation of perfusion defect information to define ischemia and infarction in a finite element model of the left ventricle. *J. Biomech. Eng.* 137(5), 1-10.
5. Leong CN, Lim E, Andriyana A, Al Abed A, Lovell NH, Hayward C, Hamilton-Craig C, Dokos S (2017). The role of infarct transmural extent in infarct extension: A computational study. *Int. J. Numer. Method. Biomed. Eng.* 33(2), 1-18.
6. Haddad SMH, Samani A (2018). A finite element model of myocardial infarction using a composite material approach. *Comput. Methods Biomech. Biomed. Engin.* 21(1), 33-46.
7. Wang H *et al.* (2018). Effects of hydrogel injection on borderzone contractility post-myocardial infarction. *Biomech. Model. Mechanobiol.* 17(5), 1533-1542.
8. Chan BT, Ahmad Bakir A, Al Abed A, Dokos S, Leong CN, Ooi EH, Lim R, Lim E (2019). Impact of myocardial infarction on intraventricular vortex and flow energetics assessed using computational simulations. *Int. J. Numer. Method. Biomed. Eng.* 35(6), 1-17.
9. Fan Y, Ronan W, Teh I, Schneider JE, Varela CE, Whyte W, McHugh P, Leen S, Roche E (2019). A comparison of two quasi-static computational models for assessment of intra-myocardial injection as a therapeutic strategy for heart failure. *Int. J. Numer. Method. Biomed. Eng.* 35(9), e3213.
10. Zhuan X, Luo X, Gao H, Ogden RW (2019). Coupled agent-based and hyperelastic modelling of the left ventricle post-myocardial infarction. *Int. J. Numer. Method. Biomed. Eng.* 35(1), 1-18.
11. Estrada AC, Yoshida K, Clarke SA, Holmes JW (2019). Longitudinal Reinforcement of Acute Myocardial Infarcts Improves Function by Transmurally Redistributing Stretch and Stress. *J. Biomech. Eng.* 142(2), 0210091-02100910.
12. Zhang Y, Wang VY, Morgan AE, Kim J, Ge L, Guccione JM, Weinsaft JW, Ratcliffe MB (2020). A Novel MRI-Based Finite Element Modeling Method for Calculation of Myocardial Ischemia Effect in Patients With Functional Mitral Regurgitation. *Front. Physiol.* 11, 1-13.
13. Zhang Y *et al.* (2021). Finite-element based optimization of left ventricular passive stiffness in normal volunteers and patients after myocardial infarction: Utility of an inverse deformation gradient calculation of regional diastolic strain. *J. Mech. Behav. Biomed. Mater.* 119, 104431.
14. Moulton MJ, Hong BD, Secomb TW (2017). Simulation of Left Ventricular Dynamics Using a Low-Order Mathematical Model. *Cardiovasc. Eng. Technol.* 8(4), 480-494.
15. Holmes JW, Lumens J (2018). Clinical Applications of Patient-Specific Models: The Case for a Simple Approach. *J. Cardiovasc. Transl. Res.* 11(2), 71-79.
16. Arts T, Delhaas T, Bovendeerd P, Verbeek X, Prinzen FW (2004). Adaptation to mechanical load determines shape and properties of heart and circulation: the CircAdapt model. *Am. J. Physiol. Heart Circ. Physiol.* 288(4):

H1943-H1954.

17. Lumens J, Delhaas T, Kirn B, Arts T (2009). Three-wall segment (TriSeg) model describing mechanics and hemodynamics of ventricular interaction. *Ann. Biomed. Eng.* 37(11), 2234-2255.
18. Walmsley J, Arts T, Derval N, Bordachar P, Cochet H, Ploux S, Prinzen FW, Delhaas T, Lumens J (2015). Fast Simulation of Mechanical Heterogeneity in the Electrically Asynchronous Heart Using the MultiPatch Module. *PLoS Comput. Biol.* 11(7), 1-23.
19. Sunagawa K, Maughan WL, Sagawa K (1982). Effect of Regional Ischemia on the Left Ventricular End-Systolic Pressure-Volume Relationship of Isolated Canine Hearts. *Circ. Res.* 52(2), 170-179.
20. Arts T, Bovendeerd P, Delhaas T, Prinzen F (2003). Modeling the relation between cardiac pump function and myofiber mechanics. *J. Biomech.* 36(5), 731-736.
21. Lumens J *et al.* (2015). Differentiating Electromechanical from Non-Electrical Substrates of Mechanical Discoordination to Identify Responders to Cardiac Resynchronization Therapy. *Circ. Cardiovasc. Imaging.* 8(9), 1-12.
22. Voigt JU *et al.* (2015). Definitions for a common standard for 2D speckle tracking echocardiography: consensus document of the EACVI/ASE/Industry Task Force to standardize deformation imaging. *Eur. Heart J. Cardiovasc. Imaging.* 16(1), 1-11.
23. Lyseggen E, Skulstad H, Helle-Valle T, Vartdal T, Urheim S, Rabben SI, Opdahl A, Ihlen H, Smiseth OA (2005). Myocardial strain analysis in acute coronary occlusion: A tool to assess myocardial viability and reperfusion. *Circulation*. 112(25), 3901-3910.
24. Cerqueira MD *et al.* (2002). Standardized myocardial segmentation and nomenclature for tomographic imaging of the heart. A statement for healthcare professionals from the Cardiac Imaging Committee of the Council on Clinical Cardiology of the American Heart Association. *Int. J. Cardiovasc. Imaging.* 18(1), 539-542.
25. van Osta N, Kirkels F, Lyon A, Koopsen T, van Loon T, Cramer MJ, Teske AJ, Delhaas T, Lumens J (2021). Electromechanical substrate characterization in arrhythmogenic cardiomyopathy using imaging-based patient-specific computer simulations. *Europace.* 23, i153-i160.
26. van Osta N *et al.* (2020). Parameter subset reduction for patient-specific modelling of arrhythmogenic cardiomyopathy-related mutation carriers in the CircAdapt model. *Phil. Trans. R. Soc. A*. 378(2173), 20190347.
27. Richardson WJ, Clarke SA, Quinn TA, Holmes JW (2015). Physiological implications of myocardial scar structure. *Compr. Physiol.* 5(4), 1877-1909.
28. Theroux P, Ross J, Franklin D, Covell JW, Bloor CM (1977). Regional myocardial function and dimensions early and late after myocardial infarction in the unanesthetized dog. *Circ. Res.* 40(2), 158-165.
29. Holmes JW, Borg TK, Covell JW (2005). Structure and Mechanics of Healing Myocardial Infarcts. *Annu. Rev. Biomed. Eng.* 7(1), 223-253.
30. Braunwald E, Kloner RA (1982). The stunned myocardium: Prolonged, postischemic ventricular dysfunction. *Circulation*. 66(6), 1146-1149.
31. Gao WD, Atar D, Backx PH, Marban E (1995). Relationship between intracellular calcium and contractile force in stunned myocardium. Direct evidence for decreased myofilament Ca2+ responsiveness and altered diastolic function in intact ventricular muscle. *Circ. Res.* 76(6), 1036-1048.
32. Ugander M, Cain PA, Johnsson P, Palmer J, Arheden H (2010). Chronic non-transmural infarction has a delayed recovery of function following revascularization. *BMC Cardiovasc. Disord.* 10, 4.

33. Zhang Y *et al.* (2005). Strain rate imaging differentiates transmural from non-transmural myocardial infarction: A validation study using delayed-enhancement magnetic resonance imaging. *J. Am. Coll. Cardiol.* 46(5), 864-871.
34. Chan J, Hanekom L, Wong C, Leano R, Cho GY, Marwick TH (2006). Differentiation of Subendocardial and Transmural Infarction Using Two-Dimensional Strain Rate Imaging to Assess Short-Axis and Long-Axis Myocardial Function. *J. Am. Coll. Cardiol.* 48(10), 2026-2033.
35. Becker M *et al.* (2009). Impact of infarct transmurality on layer-specific impairment of myocardial function: A myocardial deformation imaging study. *Eur. Heart J.* 30(12), 1467-1476.
36. Kihlberg J, Haraldsson H, Sigfridsson A, Ebbers T, Engvall JE (2015). Clinical experience of strain imaging using DENSE for detecting infarcted cardiac segments. *J. Cardiovasc. Magn. Reson.* 17(1), 1-9.
37. Huttin O *et al.* (2016). Temporal deformation pattern in acute and late phases of ST-elevation myocardial infarction: incremental value of longitudinal post-systolic strain to assess myocardial viability. *Clin. Res. Cardiol.* 105(10), 815-826.
38. McComb C, Carrick D, McClure JD, Woodward R, Radjenovic A, Foster JE, Berry C (2015). Assessment of the relationships between myocardial contractility and infarct tissue revealed by serial magnetic resonance imaging in patients with acute myocardial infarction. *Int. J. Cardiovasc. Imaging.* 31(6), 1201-1209.
39. Skulstad H, Edvardsen T, Urheim S, Rabben SI, Stugaard M, Lyseggen E, Ihlen H, Smiseth OA (2002). Postsystolic shortening in ischemic myocardium: Active contraction or passive recoil? *Circulation*. 106(6), 718-724.
40. Ferferieva V *et al.* (2012). The relative value of strain and strain rate for defining intrinsic myocardial function. *Am. J. Physiol. Heart Circ. Physiol.* 302(1), 188-195.
41. Reant P *et al.* (2016). Impact of Afterload Increase on Left Ventricular Myocardial Deformation Indices. *J. Am. Soc. Echocardiogr.* 29(12), 1217-1228.

SUPPLEMENTARY MATERIAL

Patient-specific *NCVF* estimation (PATIENT 3-6)

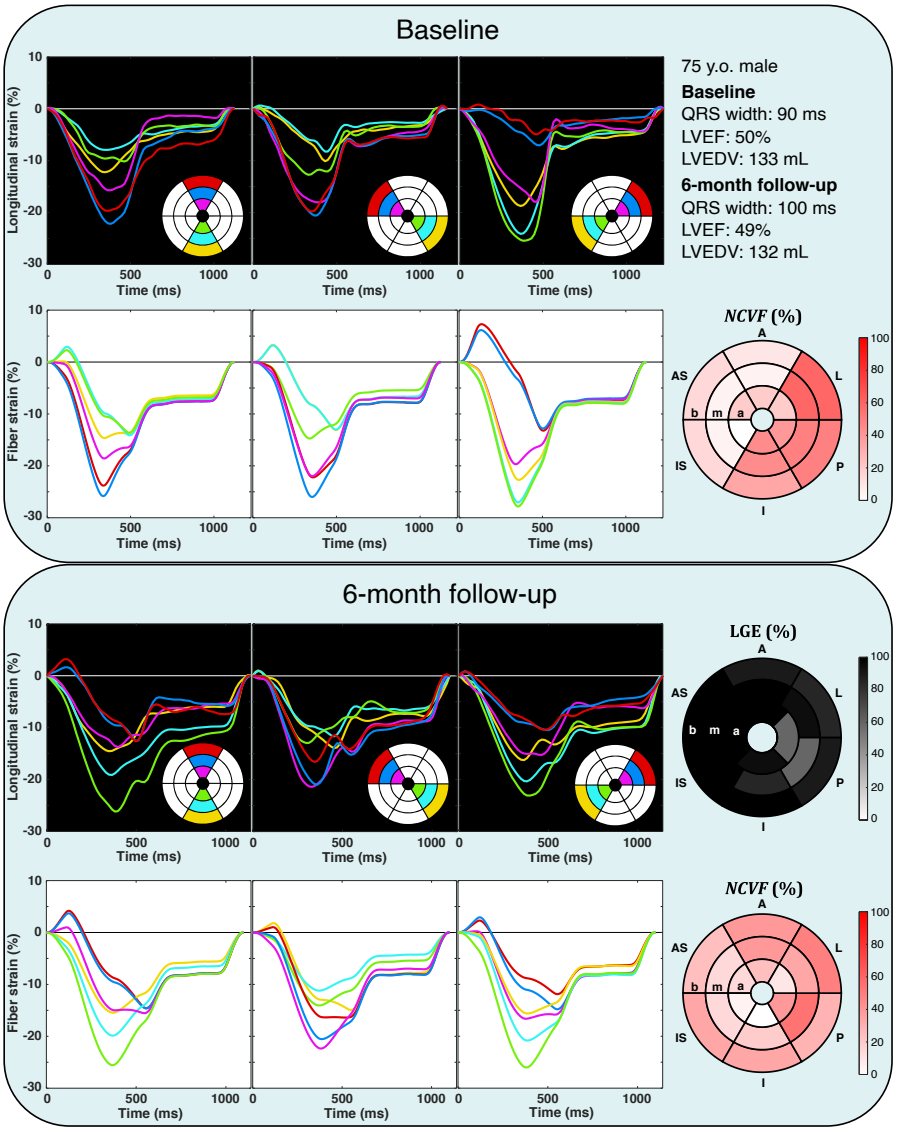

Figure S3.1: Echocardiographic strain measurements (black panels), simulated strain patterns obtained using an optimization algorithm (white panels), and corresponding estimated $NCVF$ values (bullseye plots, red color) at baseline and 6-month follow-up, together with late gadolinium enhancement (LGE) at 6-month follow-up (bullseye plot, grey color) in one patient from the DEFI-MI subcohort (PATIENT 3, a 75-year-old male).

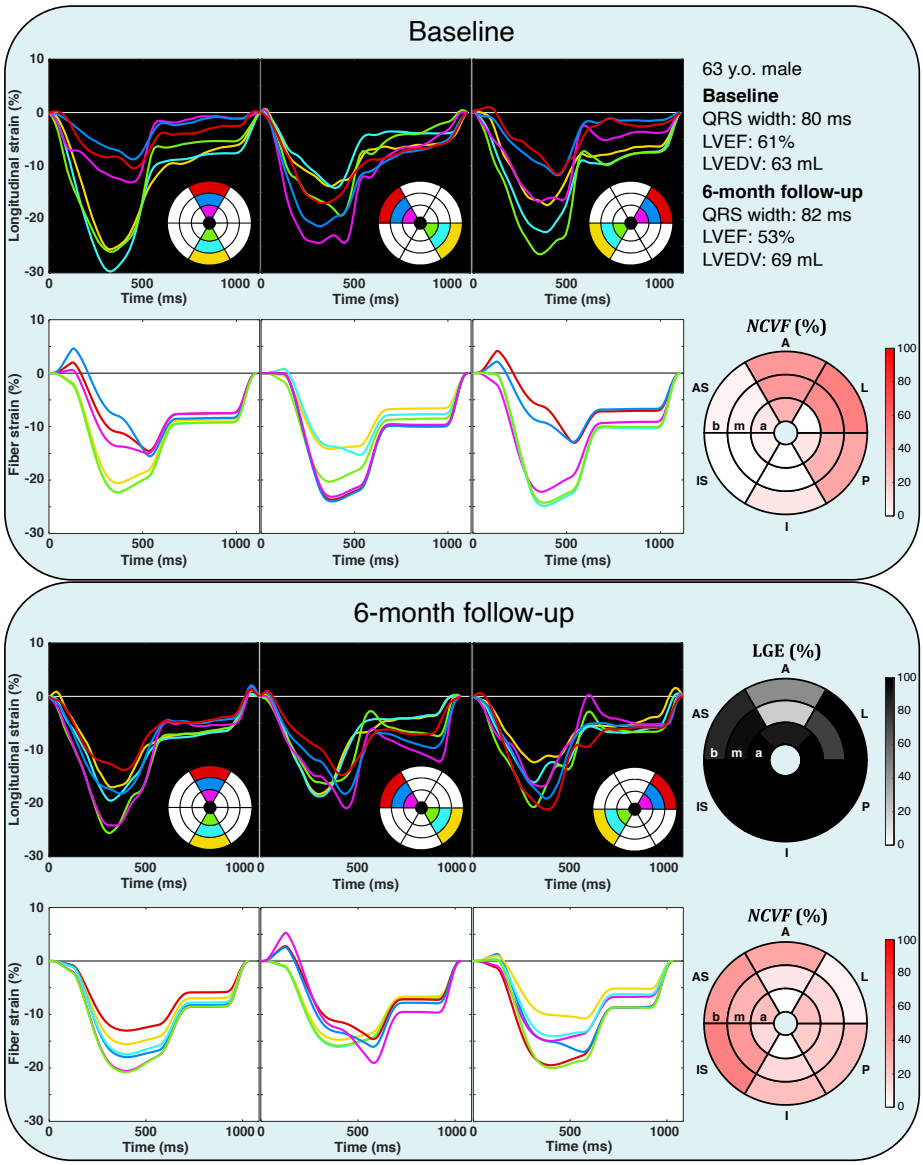

Figure S3.2: Echocardiographic strain measurements (black panels), simulated strain patterns obtained using an optimization algorithm (white panels), and corresponding estimated $NCVF$ values (bullseye plots, red color) at baseline and 6-month follow-up, together with late gadolinium enhancement (LGE) at 6-month follow-up (bullseye plot, grey color) in one patient from the DEFI-MI subcohort (PATIENT 4, a 63-year-old male).

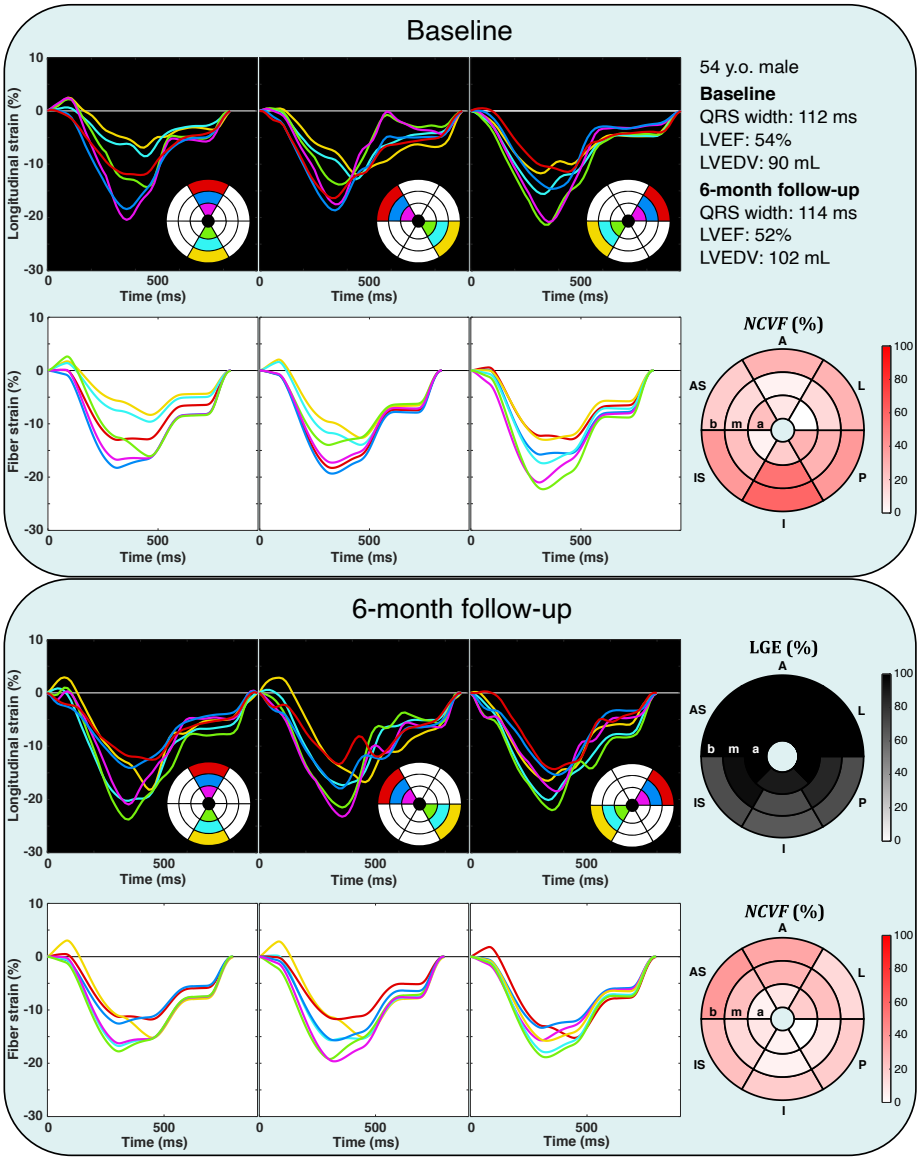

Figure S3.3: Echocardiographic strain measurements (black panels), simulated strain patterns obtained using an optimization algorithm (white panels), and corresponding estimated $NCVF$ values (bullseye plots, red color) at baseline and 6-month follow-up, together with late gadolinium enhancement (LGE) at 6-month follow-up (bullseye plot, grey color) in one patient from the DEFI-MI subcohort (PATIENT 5, a 54-year-old male).

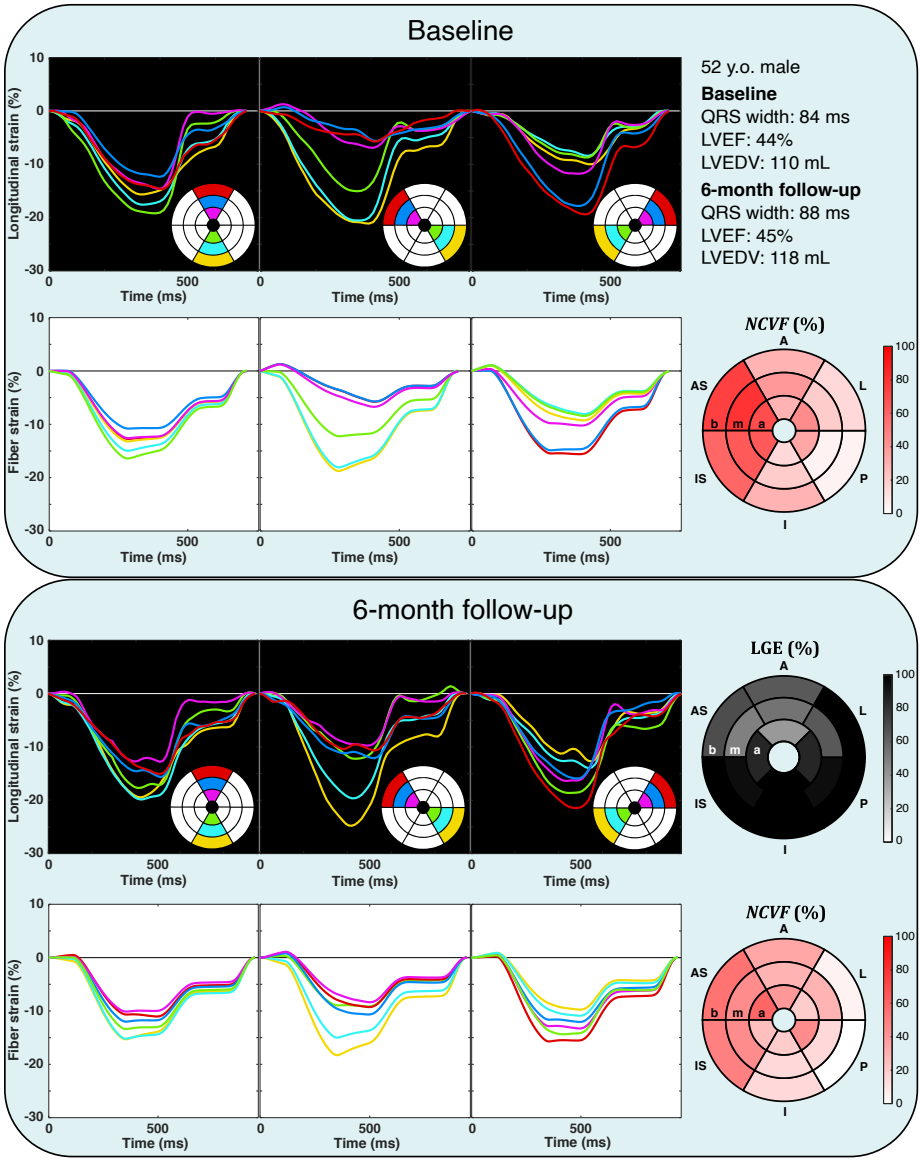

Figure S3.4: Echocardiographic strain measurements (black panels), simulated strain patterns obtained using an optimization algorithm (white panels), and corresponding estimated $NCVF$ values (bullseye plots, red color) at baseline and 6-month follow-up, together with late gadolinium enhancement (LGE) at 6-month follow-up (bullseye plot, grey color) in one patient from the DEFI-MI subcohort (PATIENT 6, a 52-year-old male).

4

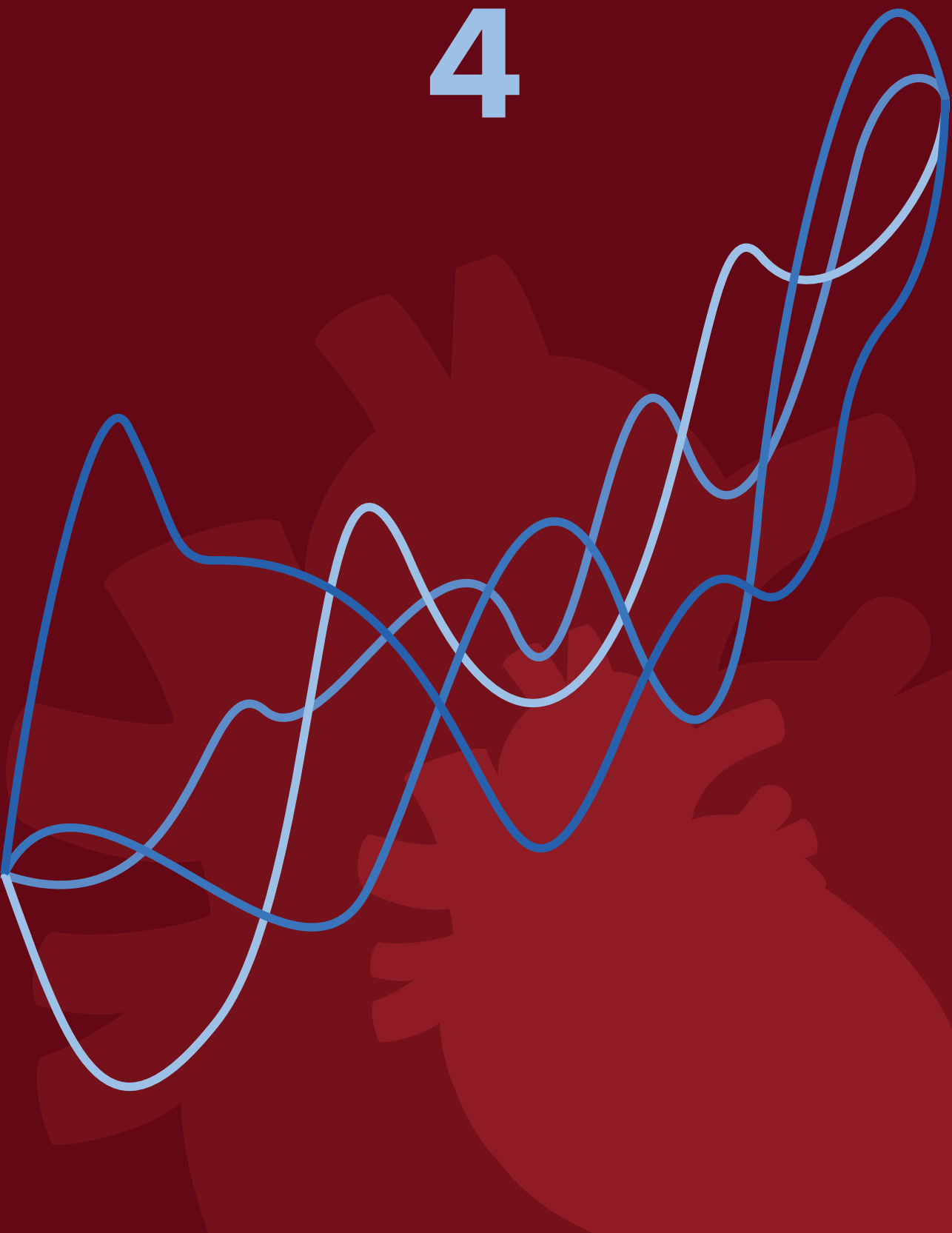

Parameter Subset Reduction for Imaging-Based Digital Twin Generation of Patients with Left Ventricular Mechanical Discoordination

T. Koopsen, N. van Osta, T. van Loon, R. Meiburg, W. Huberts, A.S. Beela, F.P. Kirkels, B.R. van Klarenbosch, A.J. Teske, M.J. Cramer, G.P. Bijvoet, A. van Stipdonk, K. Vernooy, T. Delhaas, and J. Lumens, “Parameter Subset Reduction for Imaging-Based Digital Twin Generation of Patients with Left Ventricular Mechanical Discoordination”,

Biomed. Eng. Online 2024.

ABSTRACT

Integration of a patient's non-invasive imaging data in a Digital Twin (DT) of the heart can provide valuable insight into the myocardial disease substrates underlying left ventricular (LV) mechanical discoordination. However, when generating a DT, model parameters should be identifiable to obtain robust parameter estimations. In this study, we used the CircAdapt model of the human heart and circulation to find a subset of parameters which were identifiable from LV cavity volume and regional strain measurements of patients with different substrates of left bundle branch block (LBBB) and myocardial infarction (MI). To this end, we included seven patients with heart failure with reduced ejection fraction (HFrEF) and LBBB (study ID: 2018-0863, registration date: 2019-10-07), of which four were non-ischemic (LBBB-only) and three had previous MI (LBBB-MI), and six narrow QRS patients with MI (MI-only) (study ID: NL45241.041.13, registration date: 2013-11-12). Morris Screening Method (MSM) was applied first to find parameters which were important for LV volume, regional strain, and strain rate indices. Second, this parameter subset was iteratively reduced based on parameter identifiability and reproducibility. Parameter identifiability was based on the diaphony calculated from quasi-Monte Carlo simulations and reproducibility was based on the intraclass correlation coefficient (ICC) obtained from repeated parameter estimation using dynamic multi-swarm particle swarm optimization. Goodness-of-fit was defined as the mean squared error (χ^2) of LV myocardial strain, strain rate, and cavity volume.

A subset of 270 parameters remained after MSM which produced high-quality DTs of all patients (χ^2<1.6), but minimum parameter reproducibility was poor (ICC_{min}=0.01). Iterative reduction yielded a reproducible (ICC_{min}=0.83) subset of 75 parameters, including cardiac output, global LV activation duration, regional mechanical activation delay, and regional LV myocardial constitutive properties. This reduced subset produced patient-resembling DTs (χ^2<2.2), while septal-to-lateral wall workload imbalance was higher for the LBBB-only DTs than for the MI-only DTs (p<0.05).

By applying sensitivity and identifiability analysis, we successfully determined a parameter subset of the CircAdapt model which can be used to generate imaging-based DTs of patients with LV mechanical discoordination. Parameters were reproducibly estimated using particle swarm optimization, and derived LV myocardial work distribution was representative for the patient's underlying disease substrate. This DT technology enables patient-specific substrate characterization and can potentially be used to support clinical decision making.

4.1 BACKGROUND

Left ventricular (LV) mechanical discoordination is defined by the reciprocal shortening and stretching of myocardium within the LV wall [1-3]. Myocardial stretching during systole involves wasted work and is therefore detrimental for cardiac pump function [4]. Mechanical discoordination is often caused by an electrical conduction disturbance, such as left bundle branch block (LBBB), but it can also be induced by myocardial ischemia or infarction [2]. The underlying disease substrates of mechanical discoordination determine its progression and the potential effects of cardiac resynchronization therapy (CRT) [2,5].

To increase insight into a patient's underlying disease substrates of mechanical discoordination, a Digital Twin (DT) of the patient's heart can be developed by integrating patient-specific measurements into a biophysical computational model [6]. Previous studies have demonstrated that LV regional strain measurements reveal different characteristic patterns in hearts with LBBB [7,8] and myocardial infarction (MI) [9], as well as in hearts with combined LBBB-MI substrates [5,10]. Myocardial strain measurements are therefore valuable to generate a DT. Furthermore, supplementing strain with LV cavity volume measurements, which are derived from routine non-invasive imaging, provides more information on LV systolic and diastolic function.

The CircAdapt model of the human heart and circulation [11] is a suitable model to generate DTs based on these non-invasive imaging data. CircAdapt has previously been shown to realistically simulate myocardial mechanics during LBBB and MI [12,13]. Furthermore, the model is able to simulate regional mechanics at the same spatial scale as current non-invasive strain imaging technologies and at low computational cost.

However, personalization of CircAdapt is challenged by its large number of model parameters, of which only a subset is identifiable from LV cavity volume and regional strain measurements. Determining these identifiable parameters is important to ensure robust parameter estimations of the DT [14]. To personalize a cardiovascular model with many parameters, several techniques of sensitivity and identifiability analysis have been described before [15,16]. Van Osta et al. [17] combined these techniques into a framework of parameter subset reduction, which consisted of Morris Screening Method (MSM) [18], quasi-Monte Carlo sampling, and particle swarm optimization (PSO) [19,20].

In the current study, we utilize and expand upon this framework of parameter subset reduction to determine a subset of identifiable parameters which can be used to generate DTs of patients with LV mechanical discoordination based on their LV cavity volume and regional strain measurements. We also assess the credibility of these DTs by comparing their LV myocardial work distribution against the patient's electrocardiographic characteristics and location of MI.

4.2 RESULTS

4.2.1 Sensitivity analysis

Seven consecutive iterations of MSM were performed using a 6-segment LV model, with the last iteration including a subset of important parameters only. Computational time was 4.6 ± 2.7 h per MSM iteration with an average of 2,143 ± 1,069 trajectories. The results of the first and last iteration are shown in Supplementary Figure 4.1 and 4.2. The final subset after MSM consisted of $D = 108$ parameters, of which $D_{MT} = 94$ were myocardial tissue parameters, subdivided over the LV ($D_{MT,LV} = 84$), left atrium ($D_{MT,LA} = 7$) and right ventricle ($D_{MT,RV} = 3$). The other 14 parameters included general hemodynamic parameters ($D_{GH} = 3$), pulmonary and systemic circulation parameters ($D_{PS} = 3$), and mechanical activation parameters ($D_{MA} = 8$). Success rates of evaluated trajectories in all iterations were 11.4%, 13.0%, 18.9%, 18.9%, 20.2%, 19.7%, and 20.6%, respectively.

4.2.2 Parameter estimation and identifiability analysis

The transition from a 6-segment LV model, which was used for the sensitivity and identifiability analyses, to an 18-segment LV model, which was used for patient-specific parameter estimation (PE), resulted in a three-fold increase of the number of segmental model parameters. As a result, the total number of model parameters increased from $D = 108$ to $D = 270$ (par-270; Supplementary Table 4.1). Figure 4.1a and 4.1b demonstrate the propagation of ICC_{min} vs. mean and standard deviation of χ^2 of the patient population while performing iterations of parameter subset reduction. The parameters included in all different subsets evaluated are shown in Supplementary Table 4.1. After twelve iterations of subset reduction, all parameters in the subset satisfied the criterium for reproducibility ($ICC_{min} = 0.83$). This final subset (par-75) consisted of cardiac output ($q0$), atrioventricular delay ($dTauAv$), global LV activation duration (ADO_{LV}), and four regional parameters for each of the 18 LV segments: mechanical activation delay (dT), reference wall area ($AmRef$), zero-passive stress sarcomere length ($Ls0Pas$), and stiffness coefficient ($k1$).

While ICC_{min} increased with reducing parameter subset size, goodness-of-fit decreased as reflected by an increase of the mean χ^2 of the population from 0.81 ± 0.45 (par-270) to 1.23 ± 0.56 (par-75). One additional iteration of parameter subset reduction (par-74) demonstrated that χ^2 increased to 1.47 ± 0.67, while ICC_{min} remained similar ($ICC_{min} = 0.83$).

Obtained χ^2 values including the different contributors of χ^2 for all DTs generated using par-75 are shown in Table 4.1. Out of all 13 DTs, Figure 4.2 and 4.3 show the best and least good DT according to χ^2, respectively. The least good DT (LBBB-only patient 2) visually agreed well with the strain measurements.

4.2.3 Digital Twin credibility evaluation

All LBBB-only DTs demonstrated an increased workload on the LV free wall as compared to the septum (Figure 4.4). LBBB-MI DTs 2 and 3 showed a similar characteristic LV workload

pattern which was relatively unaffected by their MI substrates. In the DT of patient 1, however, LV workload showed to be more homogeneous. There was no consistent pattern of septal-to-lateral workload imbalance in the MI-only DTs. However, in MI-only DTs 1,2,4 and 6, segments with increased LGE showed reduced normalized work ($W_{norm,i}$). Septal-to-lateral work difference $\Delta W_{norm,LW-S}$ (Figure 4.5) was positive in all LBBB-only and LBBB-MI DTs, indicating that more work was performed by the lateral wall than by the septum. In the MI-only group, both positive and negative values of $\Delta W_{norm,LW-S}$ were found, reflecting a non-consistent septal-to-lateral pattern of workload imbalance. Comparison between subgroups revealed that $\Delta W_{norm,LW-S}$ was higher for the LBBB-only DTs than for the MI-only DTs ($p<0.05$). Average $\Delta W_{norm,LW-S}$ of LBBB-MI DTs also seemed to be higher than that of MI-only DTs, however, no significant difference between these groups was found.

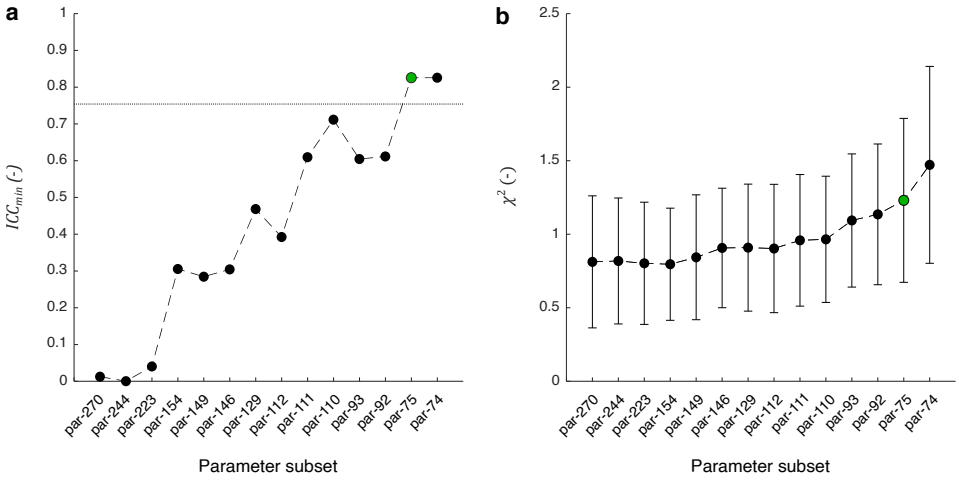

Figure 4.1: Propagation of (**a**) minimum intraclass correlation coefficient (ICC_{min}) of estimated model parameters versus (**b**) mean and standard deviation of cost function value (χ^2) of the population while performing iterations of parameter subset reduction. The green dot (par-75) indicates the parameter subset which was most extensive while satisfying the criterium of ICC_{min} > 0.75.

Table 4.1: Results of parameter estimation using the final parameter subset (par-75) for all 13 Digital Twins generated. χ^2, total cost function value; $V_{ED,mea}$, measured LV end-diastolic volume; EF_{mea}, measured LV ejection fraction; $\chi^2_{V_{ED}}$, LV end-diastolic volume contributor; χ^2_{EF}, LV ejection fraction contributor; $\overline{\chi^2_{\varepsilon}}$, strain contributor; $\chi^2_{\dot{\varepsilon}}$, strain rate contributor.

Patient subgroup	Patient number	χ^2 (-)	$V_{ED,mea}$ (mL)	EF_{mea} (%)	$\chi^2_{V_{ED}}$ (-)	χ^2_{EF} (-)	$\overline{\chi^2_{\varepsilon}}$ (-)	$\chi^2_{\dot{\varepsilon}}$ (-)
MI-only	1	0.57	132	49	<0.1	0.3	3.8	17.6
	2	1.06	69	53	2.7	0.6	6.6	30.5
	3	0.64	95	49	1.0	1.9	3.7	17.8
	4	1.47	69	54	0.2	0.5	9.0	46.1
	5	1.12	102	52	0.8	0.6	8.2	32.8
	6	0.51	118	45	0.7	0.5	4.0	14.1

Table 4.1: Continued

Patient subgroup	Patient number	χ^2 (-)	$V_{ED,mea}$ (mL)	EF_{mea} (%)	$\chi^2_{V_{ED}}$ (-)	χ^2_{EF} (-)	$\overline{\chi^2_\varepsilon}$ (-)	$\chi^2_{\tilde{\varepsilon}}$ (-)
LBBB-only	1	1.22	147	30	<0.1	0.1	9.9	36.5
	2	2.18	179	40	<0.1	0.1	18.3	64.5
	3	1.09	190	26	<0.1	0.3	6.8	34.2
	4	0.95	200	27	<0.1	<0.1	7.7	28.6
LBBB-MI	1	1.10	122	35	0.4	0.8	6.0	34.4
	2	2.09	230	27	1.7	0.8	19.6	57.5
	3	1.98	94	47	1.2	0.4	13.1	60.7

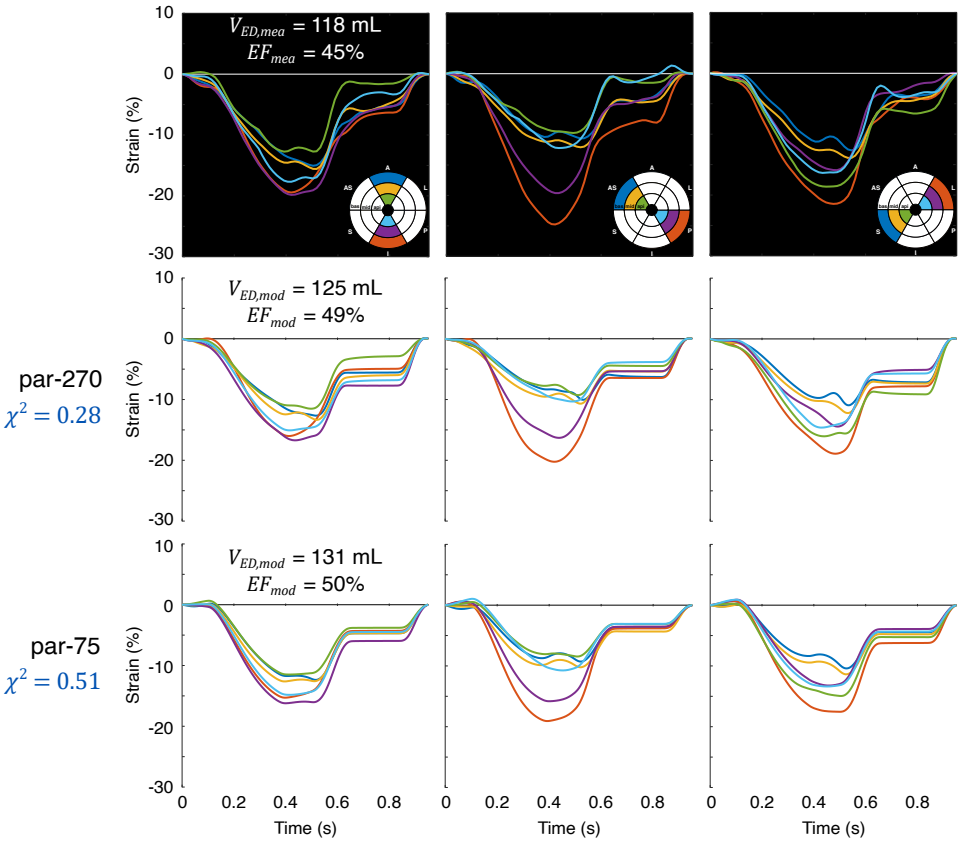

Figure 4.2: Best fit of par-75 in the patient population according to χ^2. The upper panels show the echocardiographic strain and volume measurements, while the middle and lower panels show the strains and volumes of the DT for par-270 and par-75, respectively.

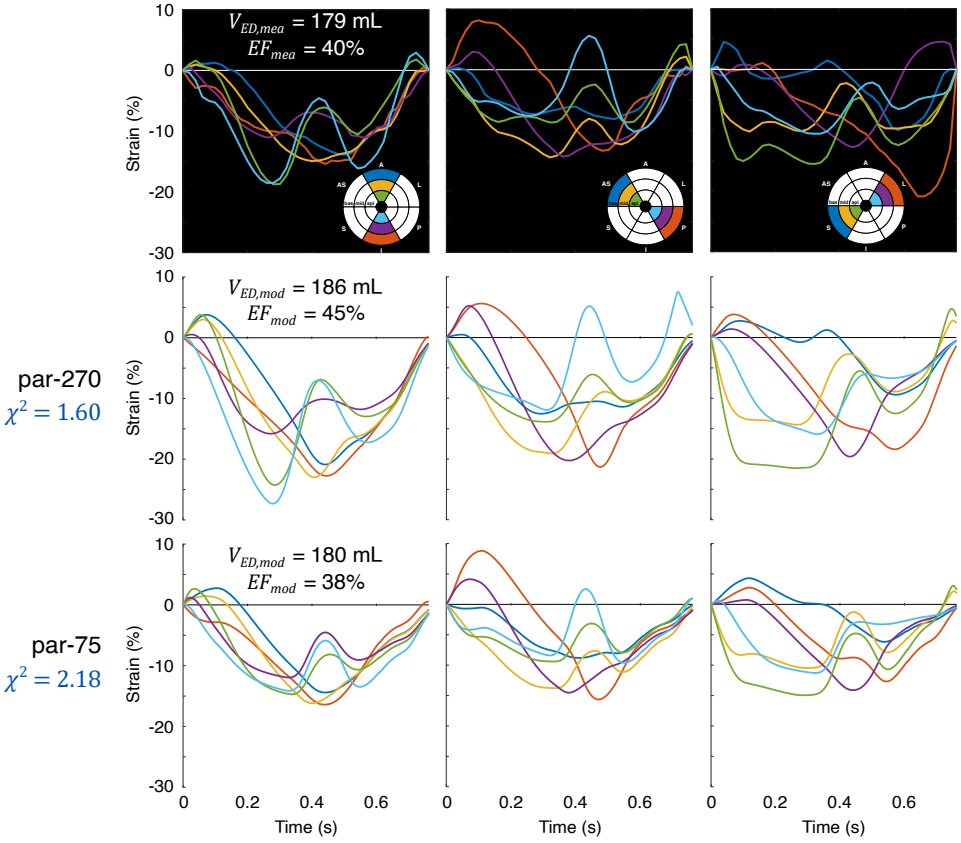

Figure 4.3: Least good fit of par-75 in the patient population according to χ^2. The upper panels show the echocardiographic strain and volume measurements, while the middle and lower panels show the strains and volumes of the DT for par-270 and par-75, respectively.

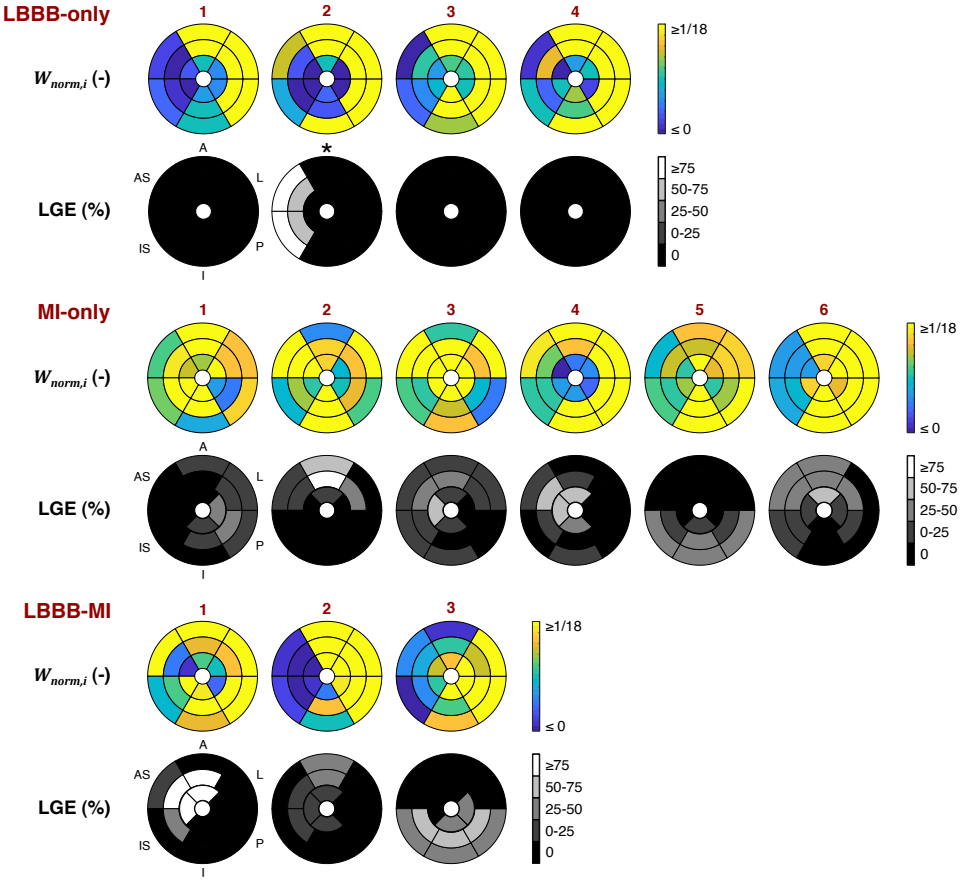

Figure 4.4: Regional LV normalized work ($W_{norm,i}$) of all DTs generated using par-75, and segmental late gadolinium enhancement (LGE) percentage as quantified using cardiac magnetic resonance imaging. All LBBB-only and LBBB-MI DTs demonstrated a larger amount of work performed by the lateral wall as compared to the septum. This typical pattern of septal-to-lateral wall workload imbalance was not observed in the MI-only DTs. In LBBB-MI DT 1 and in MI-only DTs 1,2, 4 and 6, regions of increased LGE demonstrated reduced $W_{norm,i}$. *LGE pattern was interpreted as non-ischemic by an experienced cardiologist.

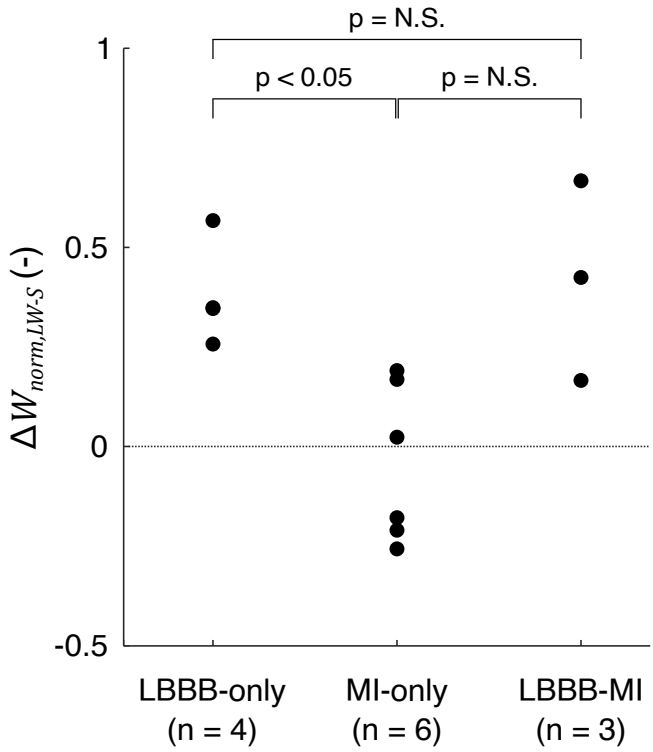

Figure 4.5: Normalized septal-to-lateral wall workload imbalance ($\Delta W_{norm,LW-S}$) for the DTs of the three patient subgroups generated using the final subset (par-75). Workload imbalance was significantly higher for the LBBB-only DTs than for the MI-only DTs ($p<0.05$) but there was no significant difference between LBBB-only and LBBB-MI DTs. While $\Delta W_{norm,LW-S}$ of LBBB-MI DTs also seemed to be higher than that of MI-only DTs, there was no significant difference between these two subgroups.

4.3 DISCUSSION

We utilized and expanded upon an existing framework for parameter subset reduction to determine a subset of parameters of the CircAdapt model which were identifiable from LV cavity volume and regional strain measurements of patients with LV mechanical discoordination. The obtained parameter subset included cardiac output, global LV activation duration, regional mechanical activation delay, and regional LV myocardial constitutive properties. This subset was used to personalize the CircAdapt model, resulting in the generation of a Digital Twin (DT). We created DTs of LBBB patients with and without MI and of narrow-QRS patients with MI. All DTs had similar LV cavity volumes and regional strain patterns as measured in the patients. Moreover, LV myocardial work distribution of the DT was found to provide insight into the patient's underlying myocardial disease substrate. We hypothesize that the proposed DT methodology can serve as a clinical support tool in patients with LV mechanical discoordination.

The complexity of the cardiovascular system provides a challenge for creating DTs of the heart and circulation, especially since available measurement data is often practically limited [14]. Complexity of developed cardiovascular models is highly variable and depends on the level of detail included to describe cardiac geometry, electromechanics, and hemodynamics [21]. When model complexity is too high for personalization, a reduced-order model can provide a useful alternative. For example, models with lower dimensionality can be developed [22,23], or models can be reparameterized to reduce their number of parameters [24]. During our iterations of parameter subset reduction, we simplified the CircAdapt MultiPatch model by grouping regional LV parameters into global LV parameters, thereby simulating homogeneity of all LV wall segments. The observed non-continuous increase of ICC (Figure 4.1a) showed that identifiability of these global parameters differed from their regional parameter definitions.

The methods which we used for sensitivity and identifiability analysis were chosen based on their strengths for our optimization problem as well as on their computational feasibility [15], but they are not the only techniques to determine parameter sensitivity and identifiability. While we applied MSM, which has previously been used for sensitivity analysis in cardiovascular models with many parameters [16,25], variance-based sensitivity analysis [15] and polynomial chaos expansion [16,26] provide powerful methods for lower-dimensional problems. Furthermore, we used diaphony as an index of identifiability, but other identifiability analysis methods have previously been described, such as profile likelihood analysis [27,28]. This method was considered too computationally demanding, but might provide more insight into the robustness of the final parameter subset. To allow more extensive sensitivity and identifiability analyses in future evaluations, surrogate models could provide interesting alternatives to reduce computational cost [29].

In evaluating parameter identifiability, structural and practical identifiability are commonly distinguished [27,28]. This distinguishment is important since practical identifiability may be improved by including more or other measurements [27,28]. We did not differentiate between structural and practical identifiability since we focused on the use of LV cavity volume and regional strain measurements. However, if future studies reveal that relevant diagnostic parameters are missing, the set of measurements should be extended.

The use of Monte Carlo techniques to calculate diaphony was previously shown to be applicable for relatively large parameter sets [17]. While Van Osta et al. [17] applied this methodology to a CircAdapt configuration with five ventricular wall segments, in the current study, seven or nineteen ventricular wall segments were included. Hereby, the cost function was dominated by the strain and strain rate components (equations (4.1), (4.11)). Our sensitivity analysis showed, however, that certain model parameters such as $q0_i$ were particularly sensitive to the volume components. We therefore also calculated diaphony for each individual component of the cost function to assess parameter identifiability.

Patients with LV mechanical discoordination are generally associated with reduced pump function resulting from underlying myocardial tissue abnormalities. Our final parameter

subset (par-75) included global LV pump function parameters as well as parameters determining regional myocardial activation and constitutive properties and therefore seems to include a relevant set of parameters also to describe the pathophysiology of mechanical discoordination. In the current patient population, which was limited in size, we identified relatively consistent patterns of estimated parameter values associated with the underlying pathologies of LBBB and MI. In DTs of LBBB patients, mechanical activation was on average later in the LV free wall than in the septum, while in DTs of MI patients a selection of myocardial segments with increased LGE had a reduced zero-passive stress length, representing a reduced contractility, or an increased stiffness coefficient. As expected, we observed that mechanical activation delay was non-identifiable in hypocontractile segments, which complicated the interpretation of segmental activation delay in most DTs. At the same time, the population size was too small to link abnormal constitutive behavior of the myocardium to increased LGE.

Future studies could investigate whether the parameters included in par-75 sufficiently represent the underlying myocardial tissue properties of the patient. This validation of parameter values is especially important since the framework of parameter subset reduction produces a single subset of reproducible parameters. While this parameter subset is the optimal solution of this framework, it may not be the only reproducible subset that allows generation of patient-resembling DTs based on the integrated measurement information. As part of this validation, parameter estimation in healthy control subjects could be performed.

Credibility of DTs generated using par-75 was supported by regional myocardial work which provides a more integrative measure than individual model parameters. Together, estimated parameter values define the myocardium's active and passive stress-strain relations which determine regional myocardial work. When calculated in experimental or clinical studies, work is often approximated using non-invasive pressure measurements [30]. These DTs provide a potential advantage here, since they include myocardial stress calculations which allow quantifying work as the enclosed area of the myocardial stress-strain loop.

In agreement with experimental findings [31], our DTs of LBBB-only patients demonstrated a septal-to-lateral imbalance of workload, which was not typically observed in our DTs of MI-only patients (Figure 4.4). This observation supports the credibility of our DTs generated. However, while it may have been expected that septal-to-lateral workload imbalance was lower in the LBBB-MI DTs as compared to the LBBB-only DTs [10], no significant difference between these subgroups was found (Figure 4.5). We note that our subgroup sizes were currently limited and that statistical significance may have been different when more patients would have been included.

Although in our study there was no consistent spatial match between regions of increased LGE in the patient and reduced LV myocardial work in the DT, our DTs did show reduced myocardial work in infarcted regions (Figure 4.4). Clinical studies using strain measurements to detect non-transmural and transmural infarction have found variable

correlations between infarct transmurality and LGE, even in the absence of LBBB [32,33]. The non-consistent match between reduced myocardial work and increased LGE in our study may therefore be considered in line with previous findings.

Comparing our results with other personalized modeling studies in patients with LV mechanical discoordination, Owashi et al. [34] similarly included HFrEF patients with LBBB, and were able to reproduce the measured strain patterns by fitting a similar set of myocardial tissue parameters as included in our final subset. Mineroff et al. [35] additionally personalized parameters determining systemic and pulmonary arterial dimensions as well as valvular dimensions. However, to be able to, they included additional measurements which increased the identifiability of these parameters in their study. As mentioned before, future studies could investigate whether our parameter subset is extensive enough to support clinical decision making or that measurements should be added to identify relevant parameters which are currently missing.

Computational cost presented limitations to the methodologies used in this study. For the initial parameter set, we considered the number of parameter interactions in the 18-segment LV model too high to perform MSM within a feasible time frame. Therefore, we used a 6-segment LV model as a computationally simpler alternative. Following the same reasoning, we also performed Sobol sampling in a 6-segment LV model. Evaluation of three million Sobol simulations took approximately 24 hours. A higher-dimensional space as associated with the 18-segment model would have required an exponential increase of the number of simulations to obtain a similar sampling density. We expect that the sensitivity and identifiability of parameters within the 6-segment LV model did not significantly differ from that in the 18-segment model, but we note that this assumption was not verified. Furthermore, in PE, a maximum of five repeated optimization protocols were performed, while a larger number of optimizations would have further improved accuracy of ICC estimations. Repeated optimizations started with a different random seed and ran independent of each other in parallel. Each DMS-PSO evaluation took between 18 and 36 hours on a single core, which limited the feasibility of performing more repetitions. During the first iterations of subset reduction, moreover, multiple parameters were removed simultaneously. Reducing per single parameter during all iterations would have been optimal since removing one parameter could increase identifiability of other parameters. By performing DMS-PSO during each iteration, however, we did assess the effect of a simultaneous removal of parameters on χ^2 so that important parameters were not accidentally removed.

While DMS-PSO is an effective optimization algorithm, it yields a single point estimate of parameter values. Future studies could investigate whether other optimization algorithms based on e.g. Bayesian inference [36] could be used to obtain parameter distributions, which can have important implications when using the DT to support clinical decision making.

To aid in clinical decision making, the DT provides several potential strategies. One strategy is to directly use estimated parameter values as diagnostic or prognostic indices [37]. Second, since the DT is integrated into a model of the heart and circulation, many other

indices representing the hemodynamic state of the patient can be derived from the DT and potentially be used as markers of interest. The septal-to-lateral workload imbalance which was quantified in this study is an example of such a derived index and has been used as a marker to predict the effect of pacemaker therapy [38]. Third, the DT may be used for *in silico* therapy testing, thereby simulating the effect of an intervention. An example would be to simulate pacing therapy in dyssynchronous heart failure patients considered for CRT [39].

4.4 CONCLUSIONS

By applying sensitivity and identifiability analysis, we successfully determined a parameter subset of the CircAdapt model which can be used to generate imaging-based Digital Twins of patients with LV mechanical discoordination. The subset included cardiac output, global LV activation duration, regional mechanical activation delay, and regional LV myocardial constitutive properties. In all patients, these parameters were reproducibly estimated using particle swarm optimization. The Digital Twin-derived LV myocardial work distribution seemed to provide insight into the patient's underlying myocardial disease substrate. This DT technology may be used for automatic substrate characterization of patients with LV mechanical discoordination, while future studies should investigate the potential of these DTs to support clinical decision making.

4.5 METHODS

4.5.1 Patient data

Patient cohort

A total of 13 patients were retrospectively included. Seven patients with heart failure with reduced ejection fraction (HFrEF) and LBBB were recruited at Maastricht University Medical Center (MUMC), all having LVEF<35% and QRS width≥130 ms. Patients were selected based on availability of late gadolinium enhancement (LGE) cardiac magnetic resonance (CMR) exams, thereby including four non-ischemic patients (LBBB-only) and three patients with prior MI (LBBB-MI). Patients were furthermore selected based on having good quality of echocardiographic images as assessed by an experienced cardiologist. Furthermore, six post-MI patients with narrow QRS (<120 ms) (MI-only) were selected from the DEFI-MI (DEtection of Cardiac FIbrosis by LGE-MRI and circulating biomarkers in patients with Myocardial Infarction) cohort, which was established at University Medical Center Utrecht (UMCU) [40] and which included patients with first-time MI. To include patients with sufficient myocardial dysfunction, we selected those DEFI-MI patients with a minimum LV infarct size of 10% of LV wall mass and a minimum LGE transmurality of 25% in at least one LV myocardial segment [12]. The clinical characteristics of these patients are summarized in Table 4.2.

Table 4.2: Clinical characteristics of the patient population and subpopulations

	All patients (n=13)	LBBB-only (n=4)	MI-only (n=6)	LBBB-MI (n=3)
Age (years)	62 ± 11	61 ± 13	58 ± 10	70 ± 6
Male gender (%, n)	85, 11	100, 4	83, 5	67, 2
QRS width (ms)	124 ± 33	153 ± 11	92 ± 13	150 ± 5
LVEF (%)	41 ± 11	31 ± 6	50 ± 3	37 ± 9
LVEDV (%)	134 ± 52	186 ± 34	98 ± 26	139 ± 55

Echocardiography

All patients had an echocardiographic exam in the context of the corresponding study where all images were digitally stored and analyzed offline. LBBB-only and LBBB-MI patients were scanned before cardiac resynchronization therapy device implantation using the EPIQ 7 ultrasound system (Philips Medical Systems, Best, The Netherlands). MI-only patients were scanned six months after the MI event using a Vivid E9 Ultrasound system (GE Healthcare, Horten, Norway). LV end-diastolic and end-systolic volumes were reassessed by an experienced cardiologist using biplane Simpson's method (Table 4.2).

Cardiac magnetic resonance

All patients underwent CMR with 2D LGE imaging for visualization of myocardial infarct tissue. All exams were performed on a 1.5 T clinical MR system (Ingenia; Philips Healthcare, Best, The Netherlands). Images were reviewed at the MUMC on a dedicated workstation (Sectra IDS7, Linköping, Sweden), and segmental LGE transmurality was determined by visual assessment of an experienced cardiologist. At the UMCU, images were analyzed offline using Philips ISP9 software (Philips Healthcare, Best, The Netherlands). Using the RV insertion points to the interventricular septum as anatomical landmarks, the heart was subdivided into 16 segments according to the model of the American Heart Association (AHA) [41], excluding the apical cap. The LGE was quantitatively assessed using the full width at half maximum (FWHM) method, providing a percentage for each of the analyzed segments and the total infarct size (global %) of the whole LV.

Myocardial strain imaging

Using QLAB advanced quantification software 13 for Philips ultrasound systems (MUMC) or EchoPac version 201 for GE (UMCU), good quality two-chamber, three-chamber and four-chamber echocardiographic acquisitions were used for speckle tracking to obtain 18-segment LV longitudinal strain. Regions of interest were automatically tracked and manually adjusted to both the endo- and epicardial border following the standard recommendations [42]. The first frame in which the mitral valve was closed was manually selected as zero-strain reference.

4.5.2 Computational model: the CircAdapt model of the human heart and circulation

The CircAdapt model of the human heart and circulation is a closed-loop lumped-parameter model which simulates beat-to-beat hemodynamics and mechanics of the heart and blood vessels [11]. The pulmonary and systemic circulation are modeled using a three-element model of resistive wave impedance, compliance and peripheral resistance [43]. Cardiac walls are modelled as spherical shells, and the left and right ventricular walls are coupled through the interventricular septum using the TriSeg module [44]. Simulation of myocardial active and passive tissue mechanics is based on the three-element Hill contraction model. When walls have homogeneous tissue properties, the model includes a total number of $D = 100$ parameters eligible for personalization. These parameters describe global hemodynamics ($D_{GH} = 3$), pulmonary and systemic vessels ($D_{PS} = 12$), valves ($D_V = 8$), pericardium ($D_P = 3$), mechanical activation ($D_{MA} = 4$), and myocardial tissue properties ($D_{MT} = 70$). Myocardial tissue properties are subdivided over the septum and left ventricular free wall ($D_{MT,LV} = 28$), right ventricle ($D_{MT,RV} = 14$), left atrium ($D_{MT,LA} = 14$), and right atrium ($D_{MT,RA} = 14$).

18-segment and 6-segment LV model

Walls are subdivided into different segments to simulate heterogeneity of myocardial tissue properties within the walls [13]. To match the spatial scale of the available echocardiographic strain measurements, an 18-segment LV model was used for parameter estimation in this study. To reduce computational cost during sensitivity and identifiability analysis, however, a simplified 6-segment LV model was used.

Using the 6- or 18-segment LV model influences the total number of parameters. The number of LV myocardial tissue parameters $D_{MT,LV}$ increases from 28 in the TriSeg model to $14 \cdot n_{seg}$, with n_{seg} the number of wall segments in the septum and LV free wall. Additionally, a mechanical activation parameter is added for each extra segment. These changes lead to a total number of $D = 160$ parameters and $D = 340$ parameters in the 6- and 18-segment model, respectively.

Global LV myocardial tissue properties

We hypothesized that LV parameters which were regionally non-identifiable were potentially identifiable on a global LV scale. To check the sensitivity and identifiability of these global LV parameters, we defined these as global offset (GO) parameters, meaning a global reference value for all LV segments. Adding these GO parameters increased the initial number of parameters for the 6-segment model to $D = 174$ (Supplementary Table 4.2).

4.5.3 Framework for parameter subset reduction

The framework for parameter subset reduction used in this study has been introduced elsewhere [17]. The framework includes a two-step approach (Figure 4.6), consisting of sensitivity analysis (SA) followed by a combination of PE and identifiability analysis (IA). This section briefly describes the framework and elaborates on a few extensions to the

previously published framework.

The methodology used for SA is the Morris Screening Method (MSM) [16,18] (Step 1), which is a suitable method for models with many parameters. MSM ranks model parameters in order of sensitivity to the model output of interest, represented by the absolute average elementary effect μ^*. During each iteration of MSM, parameters with below-average μ^* for all outputs of interest are removed from the subset (i.e., fixed to their reference value). MSM iterations are repeated until all parameters in the subset have equal to- or above-average μ^* for at least one output of interest.

In the second step, the parameter subset is iteratively reduced based on parameter identifiability. To first evaluate identifiability of the current subset, five independent DTs are generated for each patient using dynamic multi-swarm particle swarm optimization (DMS-PSO) [45] (Step 2a). Reproducibility of parameter estimations is then assessed by calculating the intraclass correlation coefficient (ICC) (Step 2b). In case of insufficient reproducibility, parameter identifiability is more precisely quantified by Sobol low-discrepancy sampling-derived diaphony (Step 2c). Finally, based on ICC and diaphony, a reduced parameter subset is proposed (Step 2d). This iterative process was stopped when all parameters were identifiable as based on reproducible parameter estimations.

Given the sampling range used for each parameter, the diaphony indicates on a 0-to-1 scale to what extent a parameter has a preferred value within this range. A diaphony close to 1 means that the parameter has a high preference and is likely identifiable. Parameters with the lowest diaphony are therefore removed from the subset (Step 2d).

The current study expanded upon the existing framework by not only selecting the samples used for calculating diaphony based on the total cost function value, but also based on the individual components of the cost function. Moreover, the number of parameters removed within one iteration was chosen to depend on the size of the subset. When this subset size was below a certain threshold, in addition, the effect on the value of the cost function was compared between removing a parameter with the lowest diaphony or ICC. The following paragraphs will discuss the methodologies of the framework in more detail.

Sensitivity analysis

Input space

The input space $\Omega = \mathbb{R}^D$ used for MSM was initially defined by the uncertainty ranges of all $D = 174$ parameters of the 6-segment LV model (Supplementary Table 4.2). These ranges aimed to include a wide spectrum of cardiovascular abnormalities which could be found in patients with LV mechanical discoordination.

To simulate relevant pathophysiological activation patterns rather than random activation patterns, a fixed direction of mechanical activation was defined, oriented from the anterior septum (S1) towards the LV posterior wall (LV4). Thereby, mechanical activation ranged from a normal to an LBBB-like activation pattern [7] (Supplementary Figure 4.3). Parameters τ_{VV} and τ_{SL} defined inter- and intraventricular delay, respectively, while parameters α_1, α_2, β_1

and β_2 determined activation times of the intermediately activated segments.

Furthermore, to simulate the functional consequences of MI, LV active myocardial tissue parameters $SfAct$, $vMax$, $LDAD$, and $LDCI$, and LV passive myocardial tissue parameters $SfPas$ and $k1$ were assigned wider ranges in segments S1, LV1, and LV3 (Supplementary Table 4.2). This definition allowed for a relatively large regional variation of contractile function and stiffness while preserving a minimum degree of LV global contractile function and limiting LV global stiffness.

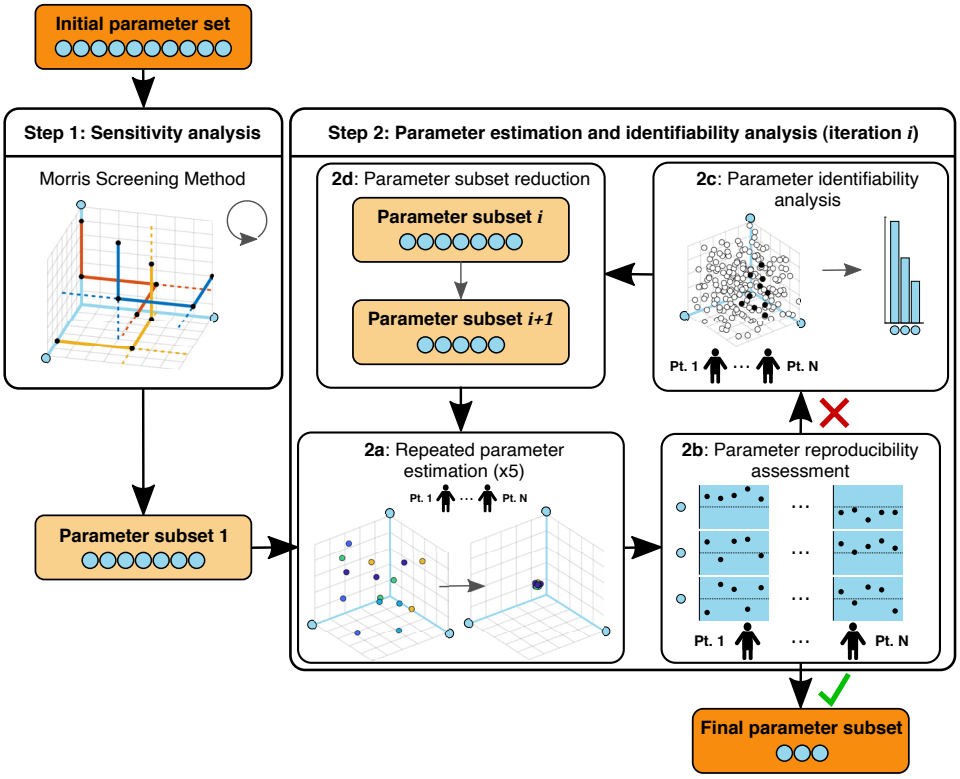

Figure 4.6: Framework for parameter subset reduction used, based on previous work by van Osta et al. [17]. The framework includes a two-step approach. In Step 1, sensitivity analysis using Morris Screening Method is performed iteratively to find parameters which are important for the model output of interest. In Step 2, using patient-specific measurements, five repeated evaluations of parameter estimation (Step 2a) are performed to assess parameter reproducibility (Step 2b), after which, in case of insufficient parameter reproducibility, identifiability analysis is performed (Step 2c) to further reduce the parameter subset (Step 2d).

Outputs of interest

We defined a set of scalar model outputs Y_j representing the available LV cavity volume and regional strain measurements. The volume outputs included LV end-diastolic volume (EDV) and LV stroke volume (SV). A total of 12 strain indices were calculated for each segment (Figure 4.7a): peak strain (ε_{min}), peak systolic strain ($\varepsilon_{min,sys}$), post-systolic shortening ($\Delta\varepsilon_{post}$), pre-ejection stretch ($\Delta\varepsilon_{pre}$), ejection stretch ($\Delta\varepsilon_{ej}$), mean systolic strain ($\bar{\varepsilon}_{sys}$), mean ejection strain ($\bar{\varepsilon}_{ej}$), time to 10% shortening ($t_{sh,10}$), time to 50% shortening ($t_{sh,50}$), time to 90% shortening ($t_{sh,90}$), time to 10% re-lengthening ($t_{rel,10}$), and time to 50% re-lengthening ($t_{rel,50}$). Furthermore, 4 regional strain rate indices were calculated (Figure 4.7b): peak systolic strain rate ($\dot{\varepsilon}_{min,sys}$), peak ejection strain rate ($\dot{\varepsilon}_{min,ej}$), mean systolic strain rate ($\bar{\dot{\varepsilon}}_{sys}$), and mean ejection strain rate ($\bar{\dot{\varepsilon}}_{ej}$). It was assumed that these strain and strain rate indices together sufficiently described the morphology and amplitude of the strain signals.

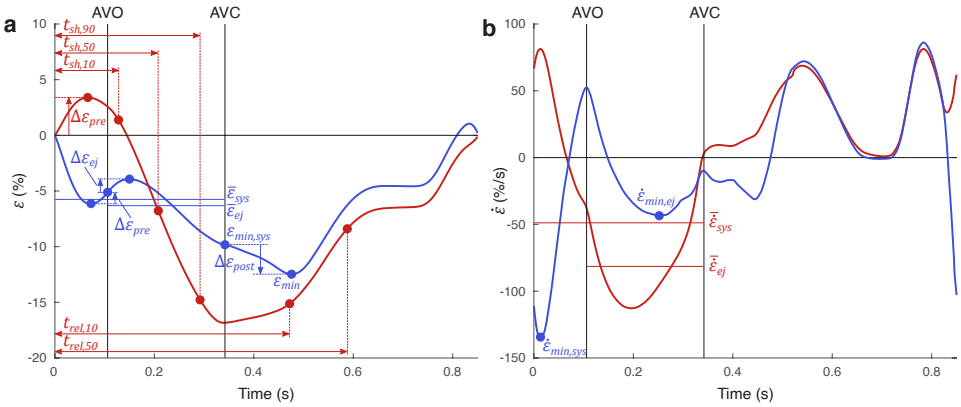

Figure 4.7: Strain (**a**) and strain rate (**b**) indices calculated as model output in MSM. ε_{min}, peak strain; $\varepsilon_{min,sys}$, peak systolic strain; $\Delta\varepsilon_{post}$, post-systolic shortening; $\Delta\varepsilon_{pre}$, pre-ejection stretch; $\Delta\varepsilon_{ej}$, ejection stretch; $\bar{\varepsilon}_{sys}$, mean systolic strain; $\bar{\varepsilon}_{ej}$, mean ejection strain; $\dot{\varepsilon}_{min,sys}$, peak systolic strain rate; $\dot{\varepsilon}_{min,ej}$, peak ejection strain rate; $\bar{\dot{\varepsilon}}_{sys}$, mean systolic strain rate; $\bar{\dot{\varepsilon}}_{ej}$, mean ejection strain rate; $t_{sh,10}$, time to 10% shortening; $t_{sh,50}$, time to 50% shortening; $t_{sh,90}$, time to 90% shortening; $t_{rel,10}$, time to 10% re-lengthening; $t_{rel,50}$, time to 50% re-lengthening. AVO, aortic valve opening; AVC, aortic valve closure.

MSM settings

The D-dimensional input space was normalized and discretized into a z-level grid (z=8) with normalized parameter values $x_i \in \left\{0, \frac{1}{z-1}, \ldots, 1\right\}$ where $i \in \{1,2,\ldots,D\}$. Each trajectory started at a randomly chosen point on the grid and parameter values were changed one-at-a-time in a random order with step size $\Delta = \frac{1}{2}\frac{z}{z-1}$, such that all points on the grid were equally likely to be included. At each parameterization $\boldsymbol{x}$ the model was evaluated and all outputs Y_j were calculated. Per iteration we computed a minimum of 1,000 successful trajectories, after which we calculated μ^* for all input-output relations.

Convergence was checked through a leave-one-out cross-validation, meaning that parameter importance was not changed upon leaving out any of the trajectories. If convergence was not met, an additional 100 successful trajectories were calculated until the leave-one-out condition was satisfied. To limit computational cost, a maximum number of 3,000 successful trajectories were calculated, after which confidence intervals were calculated using bootstrapping if convergence was not met. A parameter was then assumed to be non-important for a given output if the 95% confidence interval of μ^* was below the average μ^* of all parameters.

Parameter estimation and identifiability analysis

During PE, model parameters were estimated in the 18-segment LV model to simulate all clinically measured strain signals. Regional LV parameters which were important during MSM in at least one LV segment were estimated for all 18 segments, while important LV GO parameters were estimated only if the parameter was not estimated regionally. This parameter subset was iteratively reduced (Figure 4.6, Step 2) to obtain a subset of identifiable parameters.

Step 2a: Repeated parameter estimation

The initial particle positions for DMS-PSO were determined by generating 1,000 Monte Carlo (MC) simulations sampled from a uniform distribution with the same ranges as in MSM, but with additional restrictions on severity of electrical dyssynchrony, global LV contractility and stiffness to prevent unrealistic simulations. The initial particle positions were then defined by the best MC simulations based on the cost function χ^2, which was defined as the mean squared error:

$$\chi^2 = \frac{\chi^2_{V_{ED}} + \chi^2_{EF} + \chi^2_{\varepsilon} + \chi^2_{\dot{\varepsilon}}}{2 + n_{seg} \cdot 2} \tag{4.1}$$

With dimensionless contributors:

$$\chi^2_{V_{ED}} = \left(\frac{V_{ED,mod} - V_{ED,mea}}{\sigma_{V_{ED}}}\right)^2, \tag{4.2}$$

$$\chi^2_{EF} = \left(\frac{EF_{mod} - EF_{mea}}{\sigma_{EF}}\right)^2, \tag{4.3}$$

$$\chi^2_{\varepsilon} = \sum_{i=1}^{n_{seg}} \left(\frac{1}{n_{dp}} \sum_{k=1}^{n_{dp}} \left(\frac{\varepsilon_{i,mod}(k) - \varepsilon_{i,mea}(k)}{\sigma_{\varepsilon_i}} \right)^2 \right), \tag{4.4}$$

$$\chi^2_{\dot{\varepsilon}} = \sum_{i=1}^{n_{seg}} \left(\frac{1}{n_{dp}} \sum_{k=1}^{n_{dp}} \left(\frac{\dot{\varepsilon}_{i,mod}(k) - \dot{\varepsilon}_{i,mea}(k)}{\sigma_{\dot{\varepsilon}_i}} \right)^2 \right). \tag{4.5}$$

In these equations, $V_{ED,mod}$ and $V_{ED,mea}$ are the simulated and measured LV end-diastolic volume, respectively, while EF_{mod} and EF_{mea} represent the simulated and measured LV ejection fraction. Measurement uncertainties $\sigma_{V_{ED}}$ and σ_{EF} were assumed to be proportional to the measured value and equaled $0.13 \cdot V_{ED,mea}$ and $0.14 \cdot EF_{mea}$, respectively [46]. The number n_{seg} equals the number of myocardial segments, while n_{dp} is the number of data points used for comparing the simulated and measured strain and strain rate signals. Only strain from mitral valve closure till 10% global re-lengthening + 50 ms was included in the cost function, thereby excluding late diastolic strain. Simulated strain signals $\varepsilon_{i,mod}$ were obtained by scaling simulated fiber strain $\varepsilon_{i,mod,f}$ to the amplitude of the longitudinal strain measurements of the patient:

$$\varepsilon_{i,mod,f}(t) = \frac{L_{s,i}(t) - L_{s,i}(t_0)}{L_{s,i}(t_0)} \cdot 100\%, \tag{4.6}$$

$$\varepsilon_{i,mod} = \frac{\varepsilon_{glob,mea}}{\varepsilon_{glob,mod,f}} \cdot \varepsilon_{i,mod,f}. \tag{4.7}$$

Here, $L_{s,i}(t)$ is the sarcomere length of segment i at time t, while t_0 is the timing of mitral valve closure. Furthermore, $\varepsilon_{glob,mea}$ and $\varepsilon_{glob,mod,f}$ are the measured and simulated peak values of the global strain signal, i.e., the average strain signal of all 18 LV segments. Simulated strains and strain rates were also resampled to the sampling frequency of ε_{mea}. Measurement uncertainties σ_{ε} and $\sigma_{\dot{\varepsilon}}$ were chosen to equal 2% and 20%/s, respectively. Cycle time within the model ($tCycle$) was fixed to the average cycle time t_{cycle} of all three echocardiographic acquisitions. Five independent estimations were obtained by repeating DMS-PSO with different starting points as derived from a new set of MC simulations.

DMS-PSO settings

A total of 60 particles were used, subdivided into 20 swarms of three particles. Every 20 iterations, swarms were randomly regrouped. An input space was defined based on the input space used for MC sampling with extended parameter boundaries (Supplementary Table 4.1) to improve algorithm performance. For particles outside these boundaries, the cost function was infinite. Particle velocities were limited to 25% of the input space width to prevent particles from oscillating outside the input space. DMS-PSO was stopped when normalized particle energies were lower than 10^{-4}, meaning no parameter changed more than 1% of its MC input space width within one iteration, or when a maximum number of 2,000 iterations were completed.

Step 2b: Parameter reproducibility assessment

Intraclass correlation coefficient (ICC) was calculated for all estimated parameters by [47]:

$$ICC = \frac{MS_{between} - MS_{within}}{MS_{between} + (m-1) \cdot MS_{within}}, \tag{4.8}$$

with:

$$MS_{between} = \frac{m \cdot \sum_{i=1}^{n} (S_i - \bar{x})^2}{n-1}, \tag{4.9}$$

and:

$$MS_{within} = \frac{\sum_{i=1}^{n} \sum_{j=1}^{m} (x_{ij} - S_i)^2}{n \cdot (m-1)}. \tag{4.10}$$

In these equations, n is the number of subjects and m equals the number of observations (i.e., repeated optimizations). For a regional LV parameter, n equaled the total number of myocardial segments multiplied by the number of patients, while for a global LV parameter n equaled the number of patients. The term x_{ij} represents the i,j-th component of the $n \times k$ matrix of all data, while S_i is the mean value for each subject and $\bar{x}$ is the total mean value of all measured values x_{ij}. The minimum ICC of all parameters in the subset (ICC_{min}) was used as a criterion for accepting or rejecting the current parameter subset. The subset was accepted when ICC_{min}>0.75, corresponding with good reproducibility [48].

Step 2c: Parameter identifiability analysis

Using the 6-segment LV model, three million simulations were drawn from a Sobol low-discrepancy sampler using the same parameter ranges as in MSM [49]. Measured strains were averaged in the apex-to-base dimension, and $n_{seg} = 6$ was used to calculate the strain- and strain rate-based components of the cost function as well as the total cost function value (equations (4.4), (4.5), (4.1)). To cover all patients in one set of simulations, $tCycle$ was added as a parameter to allow for variation in heart rate. For each patient dataset s, the best N_{best} simulations were selected according to χ^2_{IA}, which was based on the original χ^2 with an additional term describing deviation of cycle time with doubled weight to increase importance:

$$\chi^2_{IA} = \frac{\chi^2_{V_{ED}} + \chi^2_{EF} + \chi^2_{\varepsilon} + \chi^2_{\dot{\varepsilon}} + 2 \cdot \chi^2_{t_{cycle}}}{4 + n_{seg} \cdot 2}, \tag{4.11}$$

with:

$$\chi^2_{t_{cycle}} = \left(\frac{tCycle - t_{cycle,mea}}{\sigma_{t_{cycle}}} \right)^2 \tag{4.12}$$

where $\sigma_{t_{cycle}} = 50\ ms$, and $tCycle$ and $t_{cycle,mea}$ are the modeled and measured cycle time, respectively. Furthermore, the best N_{best} simulations were selected for each individual component of χ^2_{IA}, meaning $\chi^2_{V_{ED}}$, χ^2_{EF}, $\chi^2_{t_{cycle}}$, and the strain- and strain rate-based components per segment $\chi^2_{\varepsilon_i}$ and $\chi^2_{\dot{\varepsilon}_i}$. Diaphony d was then calculated for all parameters p and for all sixteen outputs q per patient dataset s:

$$d_{p,q}(s) = \left|\frac{1}{N_{best}} \sum_{x_p \in X_{best}(s)} e^{i2\pi x_p}\right|, \tag{4.13}$$

with $X_{best}(s)$ the set of the best $N_{best} = 2 \cdot n_{par}$ samples for dataset s, with n_{par} the number of parameters in the current subset. Parameters p were ranked based on their maximum diaphony over all patient datasets s and outputs q. For a regional LV parameter, the maximum diaphony of all six segments was used in this ranking.

Step 2d: Parameter subset reduction

Initially, parameters with the lowest diaphony were removed from the subset. A regional LV parameter removed from the subset was returned into the subset as a global LV parameter, while global LV parameters removed were fixed to their reference values. Using this reduction approach, regional LV parameters determining the same tissue property in different LV segments were grouped into one parameter group, which was considered to be removed from the subset. When using the term 'parameter group' in this section, we therefore mean either a non-LV parameter, a global LV parameter, or a group of regional LV parameters. A total of 10, 5 or 3 parameter groups were simultaneously removed from the current subset when more than 30 groups were in the subset, between 16 and 30, or between 11 and 15, respectively. When 10 or fewer parameter groups were in the subset, only one parameter group was removed per iteration. Moreover, two reduced subsets were proposed based on removing the group with lowest diaphony or lowest ICC. The removal which caused the lowest maximal increase of χ^2 out of all patients in PE was chosen as the best option.

4.5.4 Digital Twin credibility evaluation

Experimental models of LBBB have demonstrated an asymmetrical distribution of myocardial work between the septum and LV lateral wall [31]. To evaluate credibility of the DTs generated using the reduced parameter subset, we tested whether the DTs corroborated this observation by calculating a normalized index of septal-to-lateral wall workload imbalance. Specifically, it was hypothesized that this index was higher for both the LBBB-only and LBBB-MI DTs than for the MI-only DTs, while it was also hypothesized that this index was higher for the LBBB-only than for the LBBB-MI DTs [10]. To calculate the index, first, myocardial work W_i in each of 18 LV segments i was calculated as the area enclosed by the regional stress-strain loop, multiplied with segmental wall volume. Segmental normalized work $W_{norm,i}$ was then calculated as W_i normalized by the summed

W_i of all 18 LV segments:

$$W_{norm,i} = \frac{W_i}{\sum_{j=1}^{18} W_j} \tag{4.14}$$

Hereafter, septal-to-LV lateral wall workload imbalance $\Delta W_{norm,LW-S}$ was calculated as the difference in summed $W_{norm,i}$ of the six LV posterolateral wall segments (LW) and summed $W_{norm,i}$ of the six septal segments (S):

$$\Delta W_{norm,LW-S} = \sum_{j \in LW} W_{norm,j} - \sum_{j \in S} W_{norm,j} \tag{4.15}$$

Statistical tests were performed using SPSS Statistics 24 (IBM, Chicago, IL, USA). To test the null hypotheses, the non-parametric Kruskal-Wallis test was performed with post-hoc Bonferroni correction to calculate p-values.

4.5.5 Implementation

Equations were linearized using the Newton-Raphson method and were time-integrated using the Adams-Bashford method with a variable timestep Δt with $\max(\Delta t) = 2$ ms. All computations were performed using a C++ implementation of the CircAdapt model as published before [17]. All other codings for SA, PE and IA were performed in MATLAB 2019a (MathWorks, Natick, MA, United States). Simulations were run in parallel on an AMD Ryzen Threadripper 3970X.

REFERENCES

1. Shimamoto S, Ito T, Nogi S, Kizawa S, Ishizaka N (2014). Left ventricular mechanical discoordination in nonischemic hearts: Relationship with left ventricular function, geometry, and electrical dyssynchrony. *Echocardiography*. 31(9), 1077-1084.
2. Lumens J *et al.* (2015). Differentiating Electromechanical from Non-Electrical Substrates of Mechanical Discoordination to Identify Responders to Cardiac Resynchronization Therapy. *Circ. Cardiovasc. Imaging.* 8(9), 1-12.
3. Wouters PC, Leenders GE, Cramer MJ, Meine M, Prinzen FW, Doevendans PA, De Boeck BWL (2021). Acute recoordination rather than functional hemodynamic improvement determines reverse remodelling by cardiac resynchronisation therapy. *Int. J. Cardiovasc. Imaging.* 37(6), 1903-1911.
4. Russell K, Eriksen M, Aaberge L, Wilhelmsen N, Skulstad H, Gjesdal O, Edvardsen T, Smiseth OA (2013). Assessment of wasted myocardial work: a novel method to quantify energy loss due to uncoordinated left ventricular contractions. *Am. J. Physiol. Circ. Physiol.* 305(7), H996-H1003.
5. Leenders GE, Lumens J, Cramer MJ, De Boeck BWL, Doevendans PA, Delhaas T, Prinzen FW (2011). Septal Deformation Patterns Delineate Mechanical Dyssynchrony and Regional Differences in Contractility: Analysis of Patient Data Using a Computer Model. *Circ. Heart Fail.* 5(1), 87-96.
6. Corral-Acero J *et al.* (2020). The 'Digital Twin' to enable the vision of precision cardiology. *Eur. Heart J.* 41(48), 4556-4564.
7. Risum N *et al.* (2015). Identification of Typical Left Bundle Branch Block Contraction by Strain Echocardiography Is Additive to Electrocardiography in Prediction of Long-Term Outcome after Cardiac Resynchronization Therapy. *J. Am. Coll. Cardiol.* 66(6), 631-641.
8. Gorcsan J, Anderson CP, Tayal B, Sugahara M, Walmsley J, Starling RC, Lumens J (2019). Systolic Stretch Characterizes the Electromechanical Substrate Responsive to Cardiac Resynchronization Therapy. *JACC Cardiovasc. Imaging*. 12(9), 1741-1752.
9. Lyseggen E, Skulstad H, Helle-Valle T, Vartdal T, Urheim S, Rabben SI, Opdahl A, Ihlen H, Smiseth OA (2005). Myocardial strain analysis in acute coronary occlusion: A tool to assess myocardial viability and reperfusion. *Circulation*. 112(25), 3901-3910.
10. Aalen JM *et al.* (2019). Mechanism of Abnormal Septal Motion in Left Bundle Branch Block: Role of Left Ventricular Wall Interactions and Myocardial Scar. *JACC Cardiovasc. Imaging.* 12(12), 2402-2413.
11. Arts T, Delhaas T, Bovendeerd P, Verbeek X, Prinzen FW (2004). Adaptation to mechanical load determines shape and properties of heart and circulation: the CircAdapt model. *Am. J. Physiol. Heart Circ. Physiol.* 288(4): H1943-H1954.
12. Koopsen T *et al.* (2022). A Lumped Two-Compartment Model for Simulation of Ventricular Pump and Tissue Mechanics in Ischemic Heart Disease. *Front. Physiol.* 13, 1-17.
13. Walmsley J, Arts T, Derval N, Bordachar P, Cochet H, Ploux S, Prinzen FW, Delhaas T, Lumens J (2015). Fast Simulation of Mechanical Heterogeneity in the Electrically Asynchronous Heart Using the MultiPatch Module. *PLoS Comput. Biol.* 11(7), 1-23.
14. Gray RA, Pathmanathan P (2018). Patient-specific cardiovascular computational modeling: Diversity of personalization and challenges. *J. Cardiovasc. Transl. Res.* 11(2), 80-88.

15. Eck VG, Donders WP, Sturdy J, Feinberg J, Delhaas T, Hellevik LR, Huberts W (2016). A guide to uncertainty quantification and sensitivity analysis for cardiovascular applications. *Int. J. Numer. Method. Biomed. Eng.* 32(8), e02755.
16. Donders W, Huberts W, van de Vosse F, Delhaas T (2015). Personalization of models with many model parameters: an efficient sensitivity analysis approach. *Int J. Numer. Method. Biomed. Eng.* 31(10), e02727.
17. van Osta N *et al.* (2020). Parameter subset reduction for patient-specific modelling of arrhythmogenic cardiomyopathy-related mutation carriers in the CircAdapt model. *Phil. Trans. R. Soc. A*. 378(2173), 20190347.
18. Morris MD (1991). Factorial sampling plans for preliminary computational experiments. *Technometrics*. 33, 161-174.
19. Kennedy J, Eberhart R (1995). Particle swarm optimization. *Proc. Int. Conf. Neural Networks*. 27, 1942-1948.
20. Shi Y, Eberhart R (1998). A modified particle swarm optimizer. *IEEE Int. Conf. Evol. Comput. Proc.*, 69-73.
21. Niederer SA, Lumens J, Trayanova NA (2019). Computational models in cardiology. *Nat. Rev. Cardiol.* 16(2), 100-111.
22. Zhang X, Wu D, Miao F, Liu H, Li Y (2020). Personalized Hemodynamic Modeling of the Human Cardiovascular System: A Reduced-Order Computing Model. *IEEE Trans. Biomed. Eng.* 67(10), 2754-2764.
23. Zhou Y, He Y, Wu J, Cui C, Chen M, Sun B (2022). A method of parameter estimation for cardiovascular hemodynamics based on deep learning and its application to personalize a reduced-order model. *Int. J. Numer. Method. Biomed. Eng.* 38(1), 1-23.
24. Cheung SYA, Majid O, Yates JWT, Aarons L (2012). Structural identifiability analysis and reparameterisation (parameter reduction) of a cardiovascular feedback model. *Eur. J. Pharm. Sci.* 46(4), 259-271.
25. Colebank MJ, Umar Qureshi M, Olufsen MS (2021). Sensitivity analysis and uncertainty quantification of 1-D models of pulmonary hemodynamics in mice under control and hypertensive conditions. *Int. J. Numer. Method. Biomed. Eng.* 37(11), e3242.
26. Quicken S, Donders WP, van Disseldorp EMJ, Gashi K, Mees BME, van de Vosse FN, Lopata RGP, Delhaas T, Huberts W (2016). Application of an Adaptive Polynomial Chaos Expansion on Computationally Expensive Three-Dimensional Cardiovascular Models for Uncertainty Quantification and Sensitivity Analysis. *J. Biomech. Eng.* 138(12), 1-11.
27. Raue A, Kreutz C, Maiwald T, Bachmann J, Schilling M, Klingmüller U, Timmer J (2009). Structural and practical identifiability analysis of partially observed dynamical models by exploiting the profile likelihood. *Bioinformatics*. 25(15), 1923-1929.
28. Colebank MJ, Chesler NC (2022). An in-silico analysis of experimental designs to study ventricular function: A focus on the right ventricle. *PLoS Comput. Biol.* 18(9), 1-29.
29. Karabelas E *et al.* (2022). Global Sensitivity Analysis of Four Chamber Heart Hemodynamics Using Surrogate Models. *IEEE Trans. Biomed. Eng.* 69(10), 3216-3223.
30. Russell K *et al.* (2012). A novel clinical method for quantification of regional left ventricular pressure-strain loop area: a non-invasive index of myocardial work. *Eur. Heart J.* 33(6), 724-733.
31. Prinzen FW, Hunter WC, Wyman BT, McVeigh ER (1999). Mapping of regional myocardial strain and work during ventricular pacing: Experimental study using magnetic resonance imaging tagging. *J. Am. Coll. Cardiol.* 33(6), 1735-1742.
32. Kihlberg J, Haraldsson H, Sigfridsson A, Ebbers T, Engvall JE (2015). Clinical experience of strain imaging using DENSE for detecting infarcted cardiac segments. *J. Cardiovasc. Magn. Reson.* 17(1), 1-9.

33. Huttin O *et al.* (2016). Temporal deformation pattern in acute and late phases of ST-elevation myocardial infarction: incremental value of longitudinal post-systolic strain to assess myocardial viability. *Clin. Res. Cardiol.* 105(10), 815-826.
34. Owashi K, Taconné M, Courtial N, Simon A, Garreau M, Hernandez A, Donal E, Le Rolle V, Galli E (2022). Desynchronization Strain Patterns and Contractility in Left Bundle Branch Block through Computer Model Simulation. *J. Cardiovasc. Dev. Dis.* 9(2), 53.
35. Mineroff J, McCulloch AD, Krummen D, Ganapathysubramanian B, Krishnamurthy A (2019). Optimization Framework for Patient-Specific Cardiac Modeling. *Cardiovasc. Eng. Technol.* 10(4), 553-567.
36. van Osta N *et al.* (2021). Uncertainty Quantification of Regional Cardiac Tissue Properties in Arrhythmogenic Cardiomyopathy Using Adaptive Multiple Importance Sampling. *Front. Physiol.* 12, 1-15.
37. van Osta N, Kirkels F, Lyon A, Koopsen T, van Loon T, Cramer MJ, Teske AJ, Delhaas T, Lumens J (2021). Electromechanical substrate characterization in arrhythmogenic cardiomyopathy using imaging-based patient-specific computer simulations. *Europace.* 23, i153-i160.
38. Duchenne J *et al.* (2020). Acute redistribution of regional left ventricular work by cardiac resynchronization therapy determines long-term remodelling. *Eur. Heart J. Cardiovasc. Imaging.* 21(6), 619-628.
39. Sermesant M *et al.* (2012). Patient-specific electromechanical models of the heart for the prediction of pacing acute effects in CRT: A preliminary clinical validation. *Med. Image Anal.* 16(1), 201-215.
40. Ellenbroek GHJM *et al.* (2017). Leukocyte-Associated Immunoglobulin-like Receptor-1 is regulated in human myocardial infarction but its absence does not affect infarct size in mice. *Sci. Rep.* 7(1), 1-13.
41. Cerqueira MD *et al.* (2002). Standardized myocardial segmentation and nomenclature for tomographic imaging of the heart. A statement for healthcare professionals from the Cardiac Imaging Committee of the Council on Clinical Cardiology of the American Heart Association. *Int. J. Cardiovasc. Imaging.* 18(1), 539-542.
42. Voigt JU *et al.* (2015). Definitions for a common standard for 2D speckle tracking echocardiography: consensus document of the EACVI/ASE/Industry Task Force to standardize deformation imaging. *Eur. Heart J. Cardiovasc. Imaging.* 16(1), 1-11.
43. Arts T, Reesink K, Kroon W, Delhaas T (2012). Simulation of adaptation of blood vessel geometry to flow and pressure: Implications for arterio-venous impedance. *Mech. Res. Commun.* 42, 15-21.
44. Lumens J, Delhaas T, Kirn B, Arts T (2009). Three-wall segment (TriSeg) model describing mechanics and hemodynamics of ventricular interaction. *Ann. Biomed. Eng.* 37(11), 2234-2255.
45. Liang JJ, Suganthan PN (2005). Dynamic multi-swarm particle swarm optimizer. *Proc. 2005 IEEE Swarm Intell. Symp.* 124-129.
46. Otterstad JE, Froeland G, St John Sutton M, Holme I (1997). Accuracy and reproducibility of biplane two-dimensional echocardiographic measurements of left ventricular dimensions and function. *Eur. Heart J.* 18(3), 507-513.
47. Liljequist D, Elfving B, Roaldsen KS (2019). Intraclass correlation – A discussion and demonstration of basic features. *PLoS ONE*. 14(7), e0219854.
48. Koo TK, Li MY (2016). A Guideline of Selecting and Reporting Intraclass Correlation Coefficients for Reliability Research. *J. Chiropr. Med.* 15(2), 155-163.
49. Sobol IM (1967). Point distribution in a cube and approximate evaluation of integrals. *USSR Comput. Math. Math. Phys.* 7(4), 86-112.

Supplementary Table 4.1: Parameters included in the different subsets evaluated, and their boundaries used during dynamic multi-swarm particle swarm optimization. Units are the same as in **Supplementary Table 4.2**. Abbreviations: Sy, systemic; Seg, segmental; GO, global offset; LA, left atrium; RV, right ventricle; S, septal segments; LV, LV free wall segments.

Parameter	Location	par-270	par-244	par-223	par-154	par-149	par-146	par-129	par-112	par-111	par-110	par-93	par-92	par-75	par-74	Lower bound	Upper bound
$q0$	-	X	X	X	X	X	X	X	X	X	X	X	X	X	X	1	20
$p0$	-	X	X	X	X	X										50	150
k	Sy	X														[0.08, 0.1]	[80, 100]
$p0$	Sy	X														[0.12, 0.001]	[122,1.4]
$A0$	Sy	X														[0.05, 0.05]	[50, 50]
$dTauAv$	-	X	X	X	X	X	X	X	X	X	X	X	X	X	X	-0.100	0.200
dT	Seg	X	X	X	X	X	X	X	X	X	X	X	X	X	X	-0.060 (S) -0.060 (LV)	0.120 (S), 0.200 (LV)
	LA	X	X													-0.030	0.150
$VWall$	Seg	X	X	X												1.1 (S) 1.6 (LV)	16.2 (S) 24.0 (LV)
	GO				X	X										26	385
	LA	X														3	47
$AmRef$	Seg	X	X	X	X	X	X	X	X	X	X	X	X	X	X	1.6 (S) 1.6 (LV)	24.4 (S) 24.5 (LV)
	GO															29	441
	RV	X	X	X	X											26	389
	LA	X	X													14	208
$SfAct$	Seg	X	X	X	X	X	X									0	1000
	GO							X	X	X						0	1000
	RV	X														0	1000
	LA	X	X	X	X											0	1000
TR	Seg	X	X	X	X	X	X	X								0	1
	GO								X							0	1
	RV	X														0	1

Supplementary Table 4.1: Continued.

Parameter	Location	par-270	par-244	par-223	par-154	par-149	par-146	par-129	par-112	par-111	par-110	par-93	par-92	par-75	par-74	Lower bound	Upper bound
	LA	X														0	1
TD	Seg	X	X	X	X	X	X	X	X	X	X					0	1
	GO											X				0	1
$vMax$	Seg	X	X	X												0.5	50
	GO				X											0.5	50
$dLsPas$	Seg	X														0.01	10
	GO		X													0.01	10
$LenSE$	GO	X														0	0.2
$k1$	Seg	X	X	X	X	X	X	X	X	X	X	X	X	X	X	0	100
	GO															0	100
	LA	X	X	X	X											0	100
$Ls0Pas$	Seg	X	X	X	X	X	X	X	X	X	X	X	X	X	X	0	3
	GO															0	3
	LA	X	X													0	3
$SfPas$	Seg	X	X	X												0	1000
	GO				X	X										0	1000
ADO	Seg	X	X	X	X	X	X	X	X	X	X	X	X			0	$2*t_{cycle,mea}$
	GO													X		0	$2*t_{cycle,mea}$
	LA	X														0	$2*t_{cycle,mea}$
$LDAD$	Seg	X	X													0	2
	GO			X												0	2
$LDCI$	Seg	X	X	X												0	50
	GO				X											0	50

Supplementary Table 4.2: All model parameters and ranges used in the Morris Screening Method, based on the 6-segment model. Abbreviations: Sy, systemic; Pu, pulmonary; MV, mitral valve; AV, aortic valve; TV, tricuspid valve; PV, pulmonary valve; GO, global offset; S, septal segments; LV, left ventricular free wall segments; RV, right ventricle; LA, left atrium; RA, right atrium.

	Nr.	Parameter	Location	Physiological meaning	Unit	Lower bound	Upper bound
Global hemodynamics (D_{GH} = 3)	1	$q0$	-	Cardiac output	L/min	2.1	5.5
	2	$p0$	-	Mean arterial pressure	mmHg	69	114
	3	$tCycle$	-	Cycle time	s	0.66	1.24
Arterio-venous system (D_{AV} = 12)	4	k	Sy	Stiffness exponent [inlet, outlet]	-	[6.4, 8.0]	[9.6, 12.0]
	5		Pu				
	6	Len	Sy	Characteristic length [inlet, outlet]	m	[0.32, 0.32]	[0.48, 0.48]
	7		Pu			[0.16, 0.16]	[0.24, 0.24]
	8	$p0$	Sy	Reference working pressure [inlet, outlet]	kPa	[9.7, 0.11]	[14.6, 0.17]
	9		Pu			[2.0, 0.40]	[3.0, 0.61]
	10	$A0$	Sy	Reference cross-sectional area [inlet, outlet]	cm^2	[4.0, 4.0]	[6.0, 6.0]
	11		$\overline{Pu}$			[3.8, 4.1]	[5.6, 6.2]
	12	$AWall$	Sy	Cross-sectional wall area [inlet, outlet]	cm^2	[0.91, 0.37]	[1.37, 0.55]
	13		Pu			[0.71, 0.39]	[1.06, 0.58]
	14	kAV	Sy	Resistance exponent	-	0.8	1.2
	15		Pu			1.6	2.4
Pericardium (D_P = 3)	16	k	-	Stiffness exponent	-	8	12
	17	$VRef$	-	Reference volume	L	0.53	0.80
	18	$pAdapt$	-	Adaptation pressure	mmHg	80	120

Supplementary Table 4.2: Continued.

	Nr.	Parameter	Location	Physiological meaning	Unit	Lower bound	Upper bound
Valves ***(D_V = 8)***	19	$AOpen$	MV	Opening area	cm^2	6.0	9.0
	20		AV			4.0	6.0
	21		TV			5.6	8.4
	22		PV			3.8	5.6
	23	Len	MV	Characteristic length	m	0.013	0.020
	24		AV				
	25		TV				
	26		PV				
Mechanical activation ***(D_{MA} = 8)***	27	$dTauAv$	-	Atrioventricular delay with respect to reference	s	-0.050	0.130
	28	τ_{VV}	-	Interventricular delay	s	-0.030	0.030
	29	τ_{SL}	-	Maximum intraventricular delay (septum to LV lateral wall)	s	0	0.120
	30	α_1	-	Delay factor LV1	-	1/6	3/6
	31	α_2		Delay factor LV3		3/6	5/6
	32	β_1		Delay factor S2		1/6	3/6
	33	β_2		Delay factor LV2		3/6	5/6
	34	dT	LA	Delay of mechanical activation	s	-0.010	0.050

Supplementary Table 4.2: Continued.

	Nr.	Parameter	Location	Physiological meaning	Unit	Lower bound	Upper bound
Myocardial tissue (D_{MT} = 140)	35	$VWall$	GO	Wall volume	mL	103	154
	36-37		S1-2			10	23
	38-41		LV1-4			15	35
	42		RV			50	76
	43		LA			12	19
	44		RA			5.1	7.7
	45	$AmRef$	GO	Reference wall area	cm^2	118	176
	46-47		S1-2			16	35
	48-51		LV1-4			16	35
	52		RV			104	156
	53		LA			55	83
	54		RA			48	72
	55	$SfAct$	GO	Active stress constant	kPa	60	144
	56, 57, 58		S1, LV1, LV3			0	173
	59, 60, 61		S2, LV2, LV4			48	173
	62		RV			60	144
	63		LA			42	101
	64		RA				
	65	TR	GO	Contractility rise time constant	s	0.20	0.30
	66-67, 68-71		S1-2, LV1-4			0.16	0.36
	72		RV			0.20	0.30
	73		LA			0.32	0.48
	74		RA				
	75	TD	GO	Contractility decay time constant	s	0.20	0.30
	76-77, 78-81		S1-2, LV1-4			0.16	0.36
	82		RV			0.20	0.30
	83		LA			0.32	0.48
	84		RA				

Supplementary Table 4.2: Continued.

	Nr.	Parameter	Location	Physiological meaning	Unit	Lower bound	Upper bound
***Myocardial tissue* (D_{MT} = 140)**	85	$vMax$	GO	Maximum sarcomere shortening velocity	µm/s	5.6	8.4
	86, 87, 88		S1, LV1, LV3			2.8	10.1
	89, 90, 91		S2, LV2, LV4			4.5	10.1
	92		RV			5.6	8.4
	93		LA			11.2	16.8
	94		RA				
	95	$dLsPas$	GO	Titin stiffness exponent	-	0.48	0.72
	96-97, 98-101		S1-2, LV1-4			0.38	0.86
	102		RV			0.48	0.72
	103		LA				
	104		RA				
	105	$LenSE$	GO	Series elastic element length	µm	0.032	0.048
	106-107, 108-111		S1-2, LV1-4			0.026	0.058
	112		RV			0.032	0.048
	113		LA				
	114		RA				
	115	$k1$	GO	ECM stiffness exponent	-	8	12
	116, 117, 118		S1, LV1, LV3			6.4	36
	119, 120, 121		S2, LV2, LV4			6.4	14.4
	122		RV			8	12
	123		LA				
	124		RA				
	125	$Ls0Pas$	GO	Zero-passive stress sarcomere length	µm	1.71	1.89
	126-127, 128-131		S1-2, LV1-4			1.63	1.99
	132		RV			1.71	1.89
	133		LA				
	134		RA				

Supplementary Table 4.2: Continued.

	Nr.	Parameter	Location	Physiological meaning	Unit	Lower bound	Upper bound
***Myocardial tissue* (D_{MT} = 140)**	135	$SfPas$	GO	Passive stress coefficient	kPa	17.8, 17.7*	26.8, 26.5*
	136		S1			14.1	265
	137, 138		LV1, LV3			14.3	268
	139		S2			14.1	31.8
	140, 141		LV2, LV4			14.3	32.1
	142		RV			18.2	27.3
	143		LA			40.8	61.2
	144		RA			42.0	63.0
	145	ADO	GO	Activation duration offset	s	0.52	0.78
	146-147, 148-151		S1-2, LV1-4			0.42	0.94
	152		RV			0.52	0.78
	153		LA				
	154		RA				
	155	$LDAD$	GO	Length dependency of activation duration	s	0.85	1.27
	156, 157, 158		S1, LV1, LV3			0.42	1.52
	159, 160, 161		S2, LV2, LV4			0.68	1.52
	162		RV			0.85	1.27
	163		LA				
	164		RA				
	165	$LDCI$	GO	Length dependency of contractility increase	-	7.3	10.9
	166, 167, 168		S1, LV1, LV3			3.6	13.1
	169, 170, 171		S2, LV2, LV4			5.8	13.1
	172		RV			7.3	10.9
	173		LA				
	174		RA				

* The LV free wall (LV) and septum (S) have different values for $SfPas$, therefore this number represents the values of LV, S

Supplementary Figure 4.1: Result of the first iteration of Morris Screening Method. Parameters (shown on x-axis, numbers corresponding with those in **Supplementary Table 4.2**) were ranked based on their maximum absolute average elementary effect μ^* out of all given outputs of interest (shown on y-axis). All parameters which are left of the black vertical line have normalized μ^*>1 for at least one output of interest and are therefore considered important.

Supplementary Figure 4.2: Result of the final iteration of Morris Screening Method. Parameter numbers shown on the x-axis again correspond with those in **Supplementary Table 4.2**. Note that no parameter could be removed based on absolute average elementary effect μ^*. Parameters not included in this final iteration were fixed and therefore had zero elementary effect.

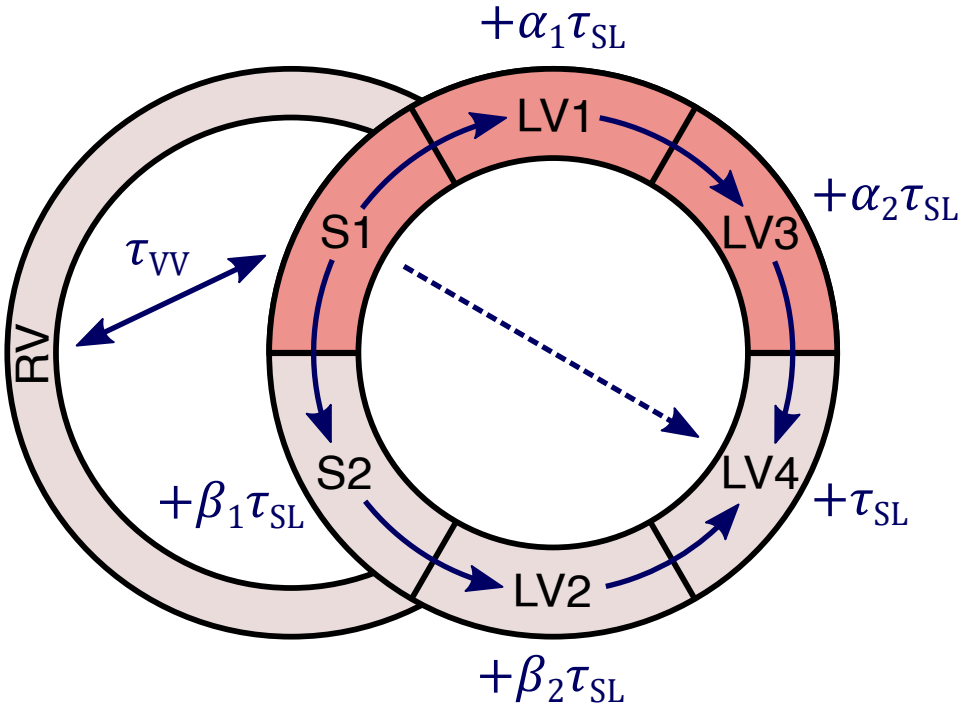

Supplementary Figure 4.3: 6-segment LV model. The blue arrows indicate the sequence of activation as was assumed during Morris Screening Method (MSM) to mimic a left bundle branch block activation pattern. Furthermore, the red segments (S1, LV1, LV3) were assigned wider parameter ranges during MSM to simulate the functional consequences of myocardial infarction.

5

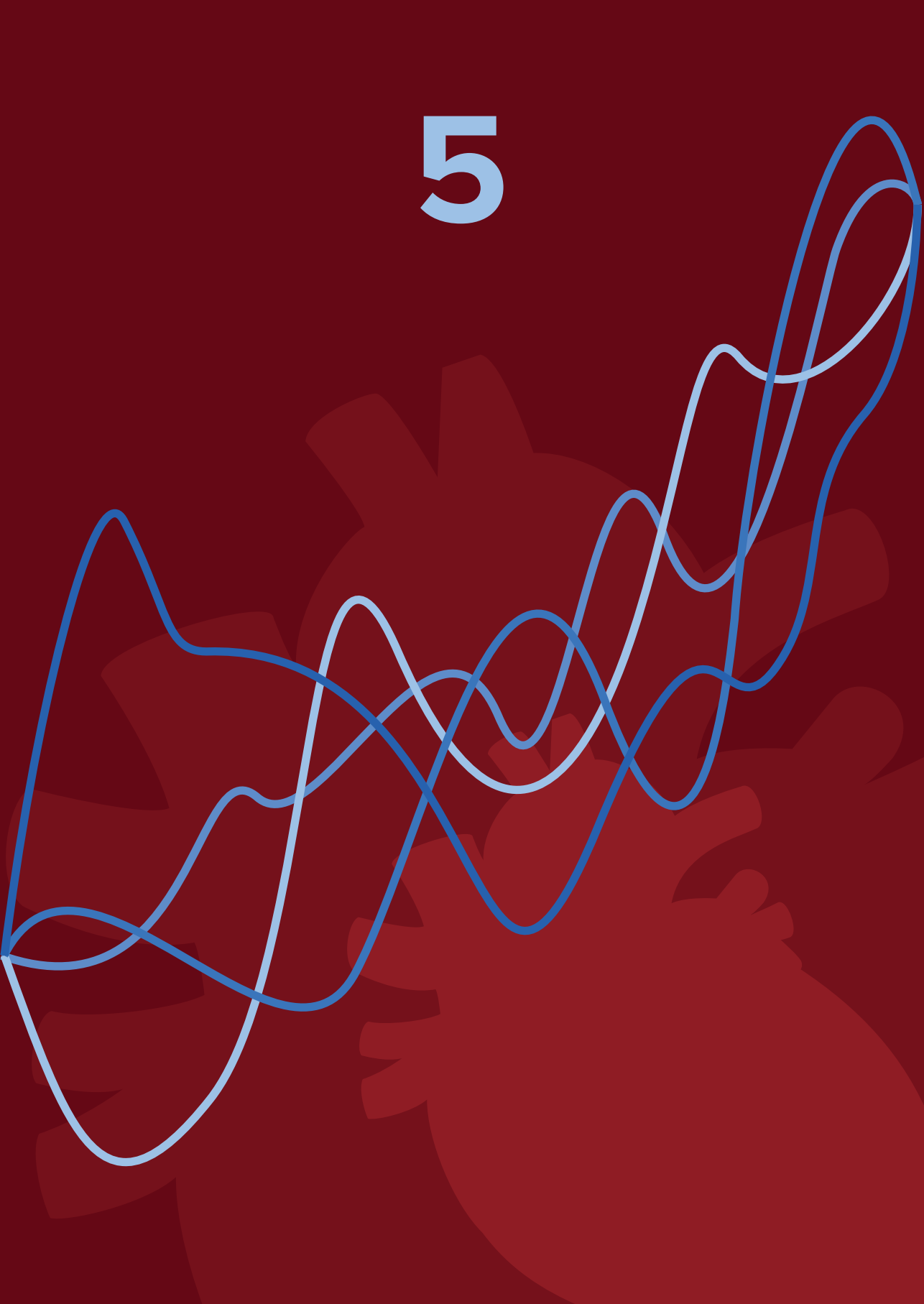

Virtual Pacing of a Patient's Digital Twin to Predict Left Ventricular Reverse Remodelling after Cardiac Resynchronization Therapy

T. Koopsen, W. Gerrits, N. van Osta, T. van Loon, P. Wouters, F.W. Prinzen, K. Vernooy, T. Delhaas, A.J. Teske, M. Meine, M.J. Cramer, and J. Lumens, "Virtual Pacing of a Patient's Digital Twin to Predict Left Ventricular Reverse Remodelling after Cardiac Resynchronization Therapy",

EP Europace 2024;26(1):1-8.

ABSTRACT

Identifying heart failure (HF) patients who will benefit from cardiac resynchronization therapy (CRT) remains challenging. We evaluated whether virtual pacing in a Digital Twin (DT) of the patient's heart could be used to predict the degree of left ventricular (LV) reverse remodeling post-CRT.

Forty-five HF patients with wide QRS complex (≥ 130 ms) and reduced LV ejection fraction (≤35%) receiving CRT were retrospectively enrolled. Echocardiography was performed before (baseline) and six months after CRT implantation to obtain LV volumes and 18-segment longitudinal strain. A previously developed algorithm was used to generate 45 DTs by personalizing the CircAdapt model to each patient's baseline measurements. From each DT, baseline septal-to-lateral myocardial work difference ($MW_{LW\text{-}S,DT}$) and maximum rate of LV systolic pressure rise ($dP/dt_{max,DT}$) were derived. Biventricular pacing was then simulated using patient-specific atrioventricular delay and lead location. Virtual pacing-induced changes $\Delta MW_{LW\text{-}S,DT}$ and $\Delta dP/dt_{max,DT}$ were correlated with real-world LV end-systolic volume change at six-month follow-up (ΔLVESV).

The DT's baseline $MW_{LW\text{-}S,DT}$ and virtual pacing-induced $\Delta MW_{LW\text{-}S,DT}$ were both significantly associated with the real patient's reverse remodelling ΔLVESV ($r=-0.60$, $P<0.001$ and $r=0.62$, $P<0.001$, respectively), while correlation between $\Delta dP/dt_{max,DT}$ and ΔLVESV was considerably weaker ($r=-0.34$, $P=0.02$).

Our results suggest that the reduction of septal-to-lateral work imbalance by virtual pacing in the DT can predict real-world post-CRT LV reverse remodelling. This DT approach could prove to be an additional tool in selecting HF patients for CRT and has the potential to provide valuable insights in optimization of CRT delivery.

GRAPHICAL ABSTRACT

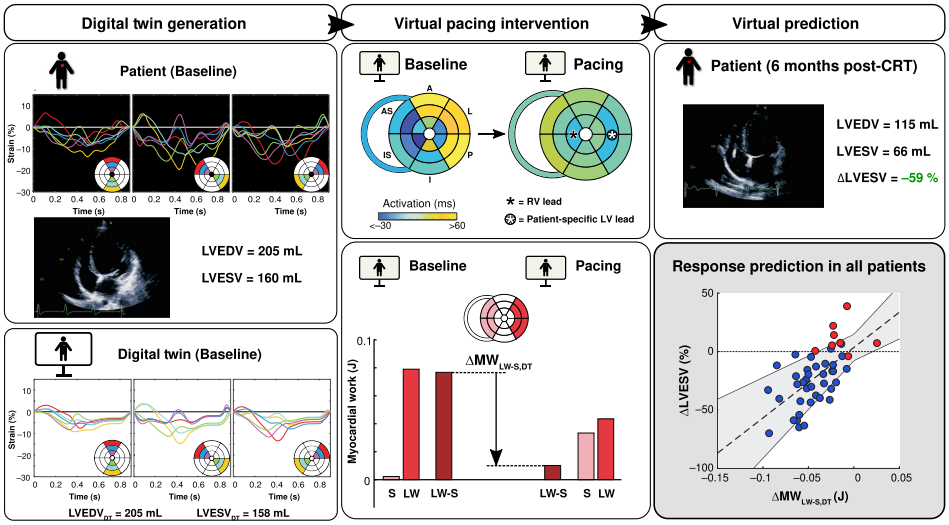

5.1 INTRODUCTION

The goal of cardiac resynchronization therapy (CRT) is to improve left ventricular ejection fraction (LVEF), reduce symptoms and improve survival of patients with dyssynchronous heart failure (HF) [1,2]. However, despite the importance of CRT as a HF treatment, a substantial number of implanted patients show no improvements [3]. At the same time, CRT is widely underutilized in eligible patients [4]. Uncertainty of which patients will benefit remains a challenge which affects the full potential of this HF therapy [4,5]. To improve patient selection, by taking into account more than the standard LVEF and electrocardiographic characteristics [6], a personalized modelling approach using the patient's Digital Twin (DT) may provide important insights [7].

The DT is a virtual representation of the patient's heart, obtained from integrating a set of patient-specific measurements into a computer model [8]. Thereby, the DT describes the unique pathophysiology of the patient and can function as a platform to evaluate the effect of therapeutic interventions. Based on the diagnostic value of myocardial strain measurements in dyssynchronous HF patients [9-11], we have previously developed an algorithm which uses left ventricular (LV) strain and volume measurements to generate a DT [12].

In this study, we evaluate whether virtual pacing of these DTs can be used to predict the degree of post-CRT LV reverse remodelling. Hereto, we retrospectively perform simulations of biventricular pacing as clinically administered in a population of dyssynchronous HF patients, including personalized atrioventricular (AV) delay and lead location. Based on previous findings suggesting that acute recoordination is more strongly associated with long-term LV reverse remodelling than baseline dyssynchrony only [13-14], we quantify the pacing-induced reduction of septal-to-lateral work difference in the DT as a potential predictor of LV reverse remodelling, as well as acute hemodynamic improvement.

5.2 METHODS

5.2.1 Study population

We retrospectively included 45 HF patients with a QRS width ≥120 ms and a reduced LVEF (≤35%), all previously selected for CRT device implantation. Patients were randomly selected from three different studies [13,15,16] based on availability and quality of all three echocardiographic views to allow derivation of 18-segment longitudinal strain. All three studies were approved by the institutional review boards or local medical ethics committees of the participating centres, and informed consent was obtained from all study participants. Characteristics of the patient population are shown in Table 5.1.

Table 5.1: Clinical characteristics of the patient population (n=45). ACE, angiotensin converting enzyme; AT2, angiotensin-2.

Age (yrs)	66 ± 10
Male gender (%, n)	62%, 28
QRS duration (ms)	171 ± 21
LBBB morphology* (%, n)	84%, 38
CRT Class I indication (%, n)	82%, 37
Atrial fibrillation (%, n)	11%, 5
Ischemic heart disease (%, n)	33%, 15
LVEDV (mL)	217 ± 83
LVESV (mL)	172 ± 81
LVEF (%)	23 ± 9
ACE-inhibitor/AT2 (%, n)	93%, 42
Beta-blocker (%, n)	67%, 30
Diuretics (%, n)	96%, 43
Spironolacton/Eplerenon (%, n)	51%, 23

*based on the Strauss criteria for LBBB [17].

5.2.2 Echocardiography

Routine echocardiographic imaging was performed at baseline and six months after CRT device implantation (mean follow-up: 6.4 ± 1.4 months) using a Vivid E9 or E95 Ultrasound system (GE Healthcare, Horten, Norway). All images were digitally stored and analysed offline. LV end-diastolic and end-systolic volumes were calculated using biplane Simpson's method and were used to calculate the relative change of LV end-systolic volume from baseline to follow-up (ΔLVESV). Good quality baseline two-chamber, three-chamber and four-chamber echocardiographic acquisitions were used for speckle tracking analysis (EchoPac version 203) to obtain LV 18-segment longitudinal strain. Regions of interest were automatically tracked and manually adjusted to the endo- and epicardial border following the standard recommendations [18]. Timing of mitral valve closure was derived from Doppler flow tracings and selected as the moment of zero-strain reference.

5.2.3 Cardiac resynchronization therapy

CRT devices were implanted according to local implantation protocols under local anaesthesia [13,15,16]. Right ventricular and right atrial leads were placed transvenously at conventional positions. Taking into account adequate pacing thresholds and absence of phrenic nerve stimulation, the LV lead was preferably placed in a lateral or posterolateral vein. Right ventricular (RV) leads were positioned preferably in the RV apex. Although no uniform AV and ventriculo-ventricular (VV) delays were mandated, paced AV delay was set to 90-130 ms, and VV delay was set to either 0 or -40 ms (LV-first).

5.2.4 Digital Twin generation algorithm

For each patient, a DT was automatically generated using a previously developed algorithm

which personalized the CircAdapt cardiovascular model [12]. Details on the Digital Twin generation algorithm and on the model, equations can be found in the Supplementary material. In short, this algorithm used the patient's baseline measurements of LV 18-segment longitudinal strain, end-diastolic volume (EDV), and end-systolic volume (ESV), and was blinded to follow-up data. The algorithm utilized dynamic multi-swarm particle swarm optimization (DMS-PSO) to minimize the mean squared error between measured and simulated LV strain and volumes. To calculate this mean squared error, the difference between measured and simulated strain and strain rate as well as the difference between measured and simulated LVEDV and LVEF were normalized to their expected measurement uncertainties. In total, 75 model parameters describing cardiac output, global LV activation duration, atrioventricular delay, and LV regional myocardial constitutive properties were selected based on an objective parameter subset reduction pipeline [12] and optimized to personalize parameter values (Figure 5.1). As a result, the patient's unique DT was obtained.

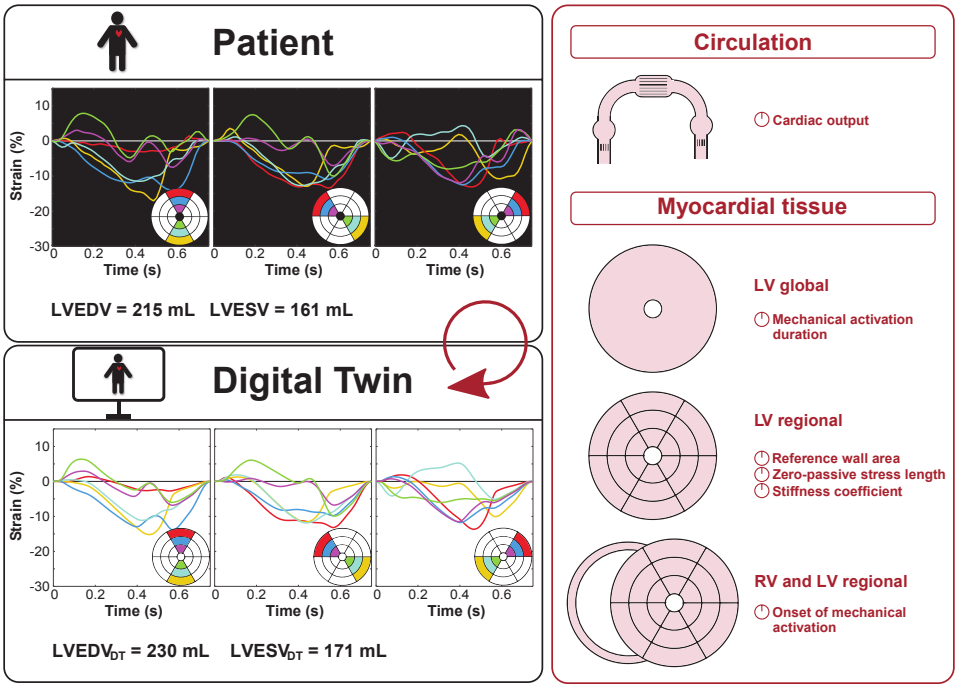

Figure 5.1: Overview of the input and output of the Digital Twin (DT) generation algorithm [12]. Left ventricular (LV) 18-segment longitudinal strain, end-diastolic volume (LVEDV) and end-systolic volume (LVESV) measurements of the patient (upper left panel) were used to automatically estimate cardiac output, global LV mechanical activation duration, regional LV myocardial constitutive properties, and regional LV and right ventricular (RV) onset of mechanical activation (right panel). As a result, a personalized model (Digital Twin) was obtained which resembled the patient (lower left panel).

5.2.5 Digital Twin: baseline indices

Maximum rate of LV systolic pressure rise ($dP/dt_{max,DT}$) and septal-to-lateral myocardial work difference ($MW_{LW\text{-}S,DT}$) of the baseline DT were calculated. Segmental myocardial work (MW) was calculated as the area of the regional stress-strain loop multiplied with segmental wall volume. Value of $MW_{LW\text{-}S,DT}$ was calculated as the absolute difference between average MW of the four basal and mid-ventricular lateral and posterior wall segments and average MW of the four basal and mid-ventricular anteroseptal and inferoseptal segments.

5.2.6 Virtual pacing and derived indices

Starting from the baseline DT, a patient-specific biventricular pacing intervention was simulated in which activation propagated radially from the location of the RV and LV lead with an intersegmental delay of 15 ms (Figure 5.2). While the location of the RV lead was similar in all patients and therefore fixed, LV lead location differed between patients. Therefore, four different patient-specific LV lead locations were simulated, i.e. anterolateral (AL), lateral (L), posterolateral (PL), and posterior (P). Furthermore, AV delay was set to either 130 [16] or 100 ms [13,15] depending on the pacing protocol of the original study. During pacing, activation of the RV wall was assumed to equal the average activation time of the septum. Absolute changes of $MW_{LW\text{-}S,DT}$ ($\Delta MW_{LW\text{-}S,DT}$) and $dP/dt_{max,DT}$ ($\Delta dP/dt_{max,DT}$) were calculated.

5.2.7 Statistical analysis

Analysis was performed using MATLAB R2022b (MathWorks, Natick, MA, USA). The relations between baseline $MW_{LW\text{-}S,DT}$, $\Delta MW_{LW\text{-}S,DT}$, $\Delta dP/dt_{max,DT}$, and $\Delta LVESV$ were assessed by univariate linear regression analysis with calculation of Pearson's correlation coefficient (r) and associated p-values.

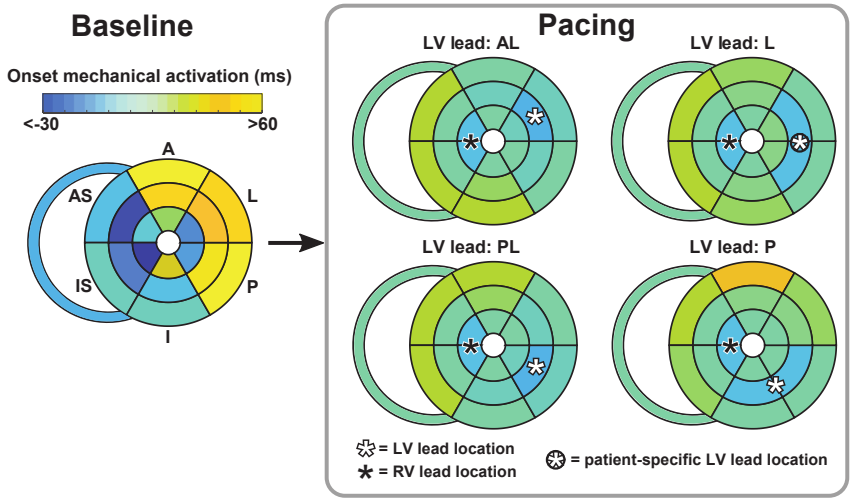

Figure 5.2: Bullseye plots of right ventricular (RV) and left ventricular (LV) regional mechanical activation at baseline and during virtual biventricular pacing in the Digital Twin. Starting from the baseline Digital Twin with automatically estimated onset of activation in the RV wall and LV wall segments (Baseline), a personalized pacing configuration was simulated in which activation was initiated at the location of the RV and patient-specific LV lead, indicated by the black and white asterisks, respectively (Pacing). From the pacing lead locations, activation propagated radially with an intersegmental delay of 15 ms. The patient illustrated here had a lateral (L) LV lead location, indicated by the circled asterisk. Furthermore, patient-specific atrioventricular delay was set to 130 ms based on the pacing protocol of the original study. Note that definition of myocardial segment location differs slightly from that of LV lead location. A, anterior; AL, anterolateral; L, lateral; PL, posterolateral; P, posterior; I, inferior; IS, inferoseptal; AS, anteroseptal.

5.3 RESULTS

5.3.1 Digital Twin generation

The patient's echocardiographic volume and strain data were well-reproduced by their DTs. In summary, LVEDV and LVESV differed from the measurements by 8 ± 7 mL and 5 ± 5 mL, respectively, while average deviation of strain per measurement point during the cardiac cycle was 1.5 ± 0.7 %.

5.3.2 Virtual pacing and work redistribution

For a single patient, Figure 5.3 shows the LV volumes and regional strain of the baseline DT, as well as its $MW_{LW\text{-}S,DT}$ at baseline and after simulating pacing. It can be observed that the septum produced almost zero work at baseline, while the LV lateral wall generated a large amount of positive work. Consequently, $MW_{LW\text{-}S,DT}$ had a large positive value at baseline. During pacing, septal work was increased while LV lateral wall work was reduced, leading to a relatively large reduction of $MW_{LW\text{-}S,DT}$. During clinical follow-up, the patient demonstrated a ΔLVESV of -59%.

For the whole patient population, baseline $MW_{LW\text{-}S,DT}$ and $\Delta MW_{LW\text{-}S,DT}$ correlated moderately with ΔLVESV (r=-0.60, P<0.001 and r=0.62, P<0.001 respectively) (Figure 5.4). At the same time, $\Delta dP/dt_{max,DT}$ correlated weaker with ΔLVESV (r=-0.34, P=0.02).

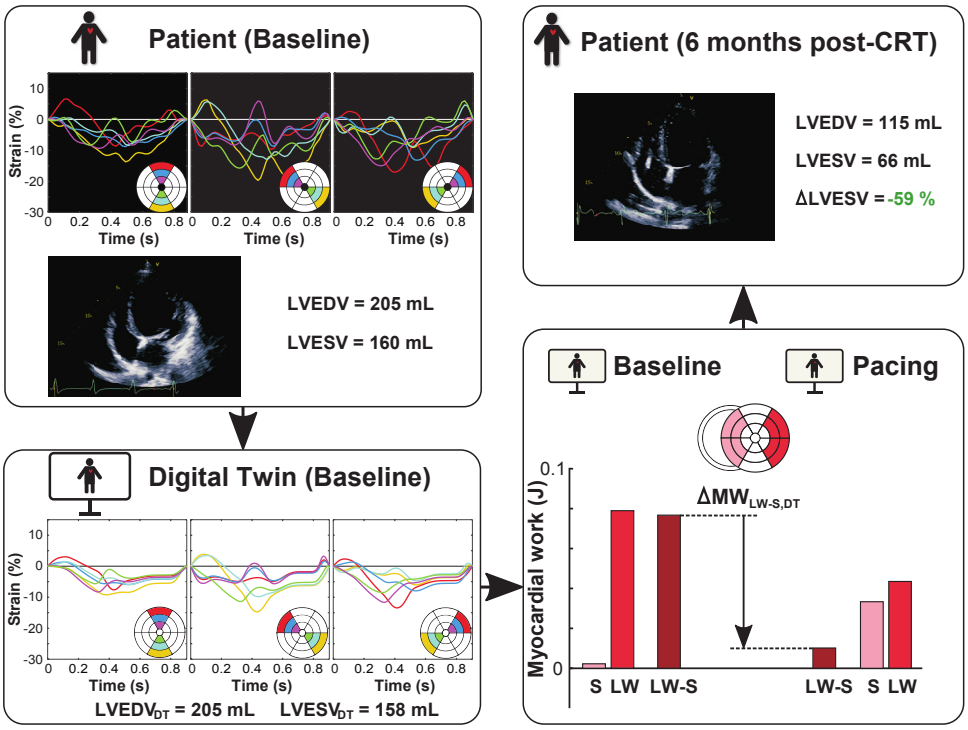

Figure 5.3: The association between septal-to-lateral work imbalance reduction by virtual pacing in the Digital Twin and long-term clinical LV reverse remodelling after CRT device implantation, illustrated for a single patient with lateral LV lead location. The Digital Twin of this patient demonstrated a relatively large pacing-induced reduction of septal-to-lateral myocardial work difference ($\Delta MW_{LW\text{-}S,DT}$), which corresponded with a relatively large reduction of LV end-systolic volume (ΔLVESV) in the patient at clinical follow-up. LVEDV, left ventricular end diastolic volume; LW, lateral wall; S, septum.

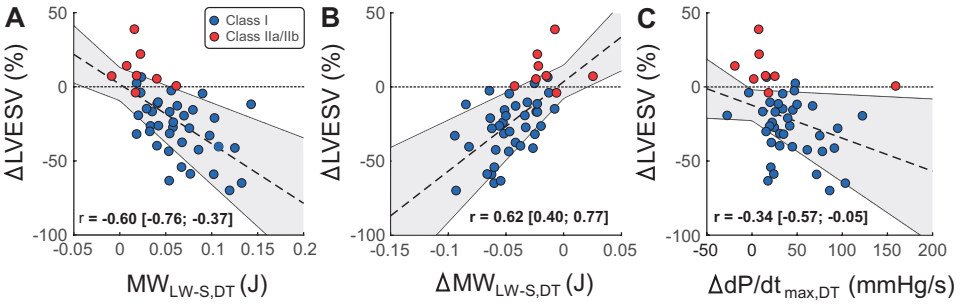

Figure 5.4: Correlation plots of relative LV volume change six months after CRT in the patient (ΔLVESV) vs. baseline Digital Twin (DT) septal-to-lateral myocardial work difference ($MW_{LW\text{-}S,DT}$) (**A**) and indices derived from virtual pacing of the DT: absolute change in $MW_{LW\text{-}S,DT}$ ($\Delta MW_{LW\text{-}S,DT}$) (**B**), and absolute change of maximum rate of LV systolic pressure rise ($\Delta dP/dt_{max,DT}$) (**C**). The blue dots (n=37) represent patients with a Class I indication for CRT, while the red dots (n=8) represent patients with a Class IIa or IIb indication for CRT, according to the Strauss criteria for LBBB [17]. Indices $MW_{LW\text{-}S,DT}$ and $\Delta MW_{LW\text{-}S,DT}$ were significantly associated with ΔLVESV (r=-0.60, P<0.001 and r=0.62, P<0.001, respectively), while $\Delta dP/dt_{max,DT}$ correlated considerably weaker with ΔLVESV (r=-0.34, P=0.02).

5.4 DISCUSSION

The present study investigated whether virtual pacing in Digital Twins (DTs) of heart failure (HF) patients, generated using baseline echocardiographic imaging data, could be used to predict the degree of LV reverse remodelling six months after CRT. It was found that the virtual pacing-induced reduction of septal-to-lateral work difference in the DT was significantly associated with the patient's LV end-systolic volume reduction at clinical follow-up. This DT technology could prove to be an additional tool in selecting HF patients for CRT and has the potential to provide valuable insights in optimization of CRT delivery.

Virtual pacing of our DTs revealed that the DT's acute mechanical recoordination was more strongly associated with the patient's LVESV reduction than the DT's acute hemodynamic improvement. This result agrees with the findings of recent clinical studies [13,14] and suggests that mechanical recoordination can be an effective target for optimizing pacing delivery, also in the DT. Acute hemodynamic improvement represents the acute success of resynchronization but its predictive value for long-term LV reverse remodelling varies among studies [19,20].

The DT's baseline septal-to-lateral work imbalance as well as its change after virtual pacing correlated well with real-world LV reverse remodelling (Figure 5.4). Firstly, this corroborates previous clinical studies showing that baseline septal-to-lateral work imbalance is a marker of CRT response potential [14,21]. Secondly, this finding suggests that our virtual pacing interventions were representative for clinical CRT, thereby strengthening the credibility of our DT technology.

Interestingly, the DTs of the few patients with Class II indications according to the 2013

ESC guidelines on cardiac pacing and CRT [22] showed a small reduction of septal-to-lateral work difference by virtual pacing as compared to the DTs of the patients with a Class I indication. Even more interestingly, the virtual pacing effect appeared to have additional prognostic value in patients with a Class I indication for CRT. Within this subgroup, there was significant heterogeneity in the degree of LV reverse remodelling which was strongly associated with the virtual pacing-induced work redistribution in their DTs.

The comparison of DT-derived indices with measures of long-term LV reverse remodelling is supported by the good correlation of LVESV reduction with mortality [23]. Furthermore, a similar association between acute myocardial work redistribution by CRT and LV reverse remodelling has previously been established in clinical studies [13,14]. These observations strengthen the current validation approach which was based on LV remodelling indices. However, the correlation of the DT with other response measures, such as hard clinical endpoints, remains to be investigated in future studies.

Future studies will also investigate the predictive value of the DT at individual patient level, i.e. by virtual optimization of pacing settings (e.g. sites and delays). Investigating the effects of LV lead location was beyond the scope of the current manuscript and may require a prospective study setup where multiple LV lead locations are tested in the same patient. A previous modeling study suggested that LV lead position sensitively determines the distribution of myocardial work, particularly in hearts with LBBB and myocardial scar, where a balanced position remote from both the scar and the RV lead was associated with the most homogeneous distribution of MW [24].

As far as we know, this is the first patient-specific modelling study that calculates the pacing-induced change of septal-to-lateral work imbalance as a predictor of CRT response. Calculation of acute hemodynamic response has been more common and shows conflicting results between modelling studies. In contrast to our findings, acute improvement of LV dP/dt_{max} was predictive for long-term LV reverse remodelling in other personalized heart models [25,26]. However, another study showed that the simulated shortening of QRS duration, which may be closely related to acute LV dP/dt_{max} improvement [27], correlated poorly with LV reverse remodelling in ischemic LBBB patients [28].

While our current DT approach relied on mechanical input information only, this approach should be considered in combination with available electrical measurements of the patient. Baseline QRS area has been shown to have a strong association with echocardiographic response to CRT [16,29] and may e.g. be combined in a multivariate analysis with the degree of septal-to-lateral work reduction in the DT. Another index which quantifies electrical dyssynchrony at baseline is the standard deviation of electrical activation times, which has been shown to be predictive for post-CRT LVEF improvement [30]. Although regional RV and LV activation times were automatically estimated by the DT algorithm, it should be noted that this activation represents mechanical rather than electrical activation.

Besides the use of electrical measurements to supplement the DT's response prediction, these measurements could also be integrated into the DT itself. While the

current model implementation is not capable to do so, integration of electrical information into the DT to better characterize the patient's electrical activation pattern could further improve prediction of the effects of pacing. This electrical characterization may especially be important in ischemic patients which have abnormal conduction in scarred areas [31]. When also combining such a DT with models of electrical wave propagation to simulate different pacing conditions [32], the interaction between the patient's electrical and non-electrical tissue characteristics may be more closely investigated.

5.4.1 Clinical implications

The DTs generated by our algorithm reveal the unique myocardial disease substrates of the patient and may thereby support CRT patient selection as well as therapy delivery. In the first place, the DT's baseline septal-to-lateral work imbalance provides a marker of CRT response potential. Furthermore, identification of hypocontractile segments in the DT which may indicate ischemia or scar could guide LV lead location during implantation and potentially present an alternative to the use of late gadolinium enhancement magnetic resonance imaging (MRI) techniques [21,33]. This study focused on the effects of MW since these have been associated with response to CRT. However, more mechanistic insight might be concealed in the estimated DT tissue characteristics. Future research should try to reveal these insights, which may further improve the predictive power of the DT technology for CRT response.

Based on the interaction of the DT with virtual pacing, moreover, more insight into the mechanisms by which a patient does or does not positively respond to CRT can be obtained. This interaction between the DT and pacing intervention may at the same time provide a platform for therapy optimization in individual HF patients. For example, manipulation of virtually paced AV- and VV-delay settings and lead location in the DT could allow personalization of pacing delivery. In contrast to using default pacemaker settings, or guiding lead location by e.g. hemodynamic optimization during the implantation procedure [20], virtual pacing may identify one or several adequate lead locations prior to pacemaker device implantation. Similarly, the technology could facilitate optimization of pacemaker settings during later stages of CRT delivery, potentially based on generation of a new DT at clinical follow-up.

Application of this DT technology requires data obtained using routine echocardiography and could therefore be relatively easily implemented in clinical practice. Prior to being eligible as a clinical tool to support patient selection and therapy delivery, however, further validation of this technology is essential. This validation could explore how potential errors of currently used clinical data propagate in the DT technology and whether other imaging modalities, such as Doppler echo or cine MRI, are of additional or alternative diagnostic value. Generation of the patient's DT currently consumed between 12 and 24 hours and was thereby by far more time-consuming than the virtual pacing, which was performed within seconds. Evaluation of different pacing conditions using the current approach would therefore be highly feasible.

5.4.2 Limitations

The current study did not compare predictivity of pacing-induced septal-to-lateral work imbalance reduction in the DT with already existing indices to predict the effect of CRT. Our primary focus currently was to present a novel methodology and to demonstrate its potential for clinical application. However, future research should investigate whether this DT technology improves clinical decision making in dyssynchronous HF patients.

Furthermore, our patient population included eight patients with a Class IIa or IIb indication for CRT. These patients demonstrated a relatively low response to CRT in terms of LV reverse remodelling. Although we found a similarly negative result for these patients by virtual pacing of their DT, i.e., a relatively low workload imbalance reduction, it remains essential to test this technology in more patients with a Class IIa or IIb indication for CRT.

Due to the incomplete documentation of personalized AV- and VV-delay settings as applied in these patients during clinical CRT, we chose to simulate representative population-based AV- and VV-delay settings as derived from the original studies. This choice may have influenced the correlations obtained in this study. However, we hypothesize that simulation of these general AV- and VV-delay settings will rather have worsened than improved these correlations.

5.5 CONCLUSION

We successfully used virtual biventricular pacing interventions in Digital Twins of dyssynchronous heart failure patients to predict response to CRT. Our results suggest that the reduction of septal-to-lateral work imbalance by virtual pacing in the Digital Twin can predict the patient's post-CRT LV reverse remodelling. This Digital Twin approach could prove to be an additional tool in selecting HF patients for CRT and has the potential to provide valuable insights in optimization of CRT delivery.

REFERENCES

1. Cleland JGF, Daubert JC, Erdmann E, Freemantle N, Gras D, Kappenberger L, Tavazzi L (2005). The Effect of Cardiac Resynchronization on Morbidity and Mortality in Heart Failure. *N. Engl. J. Med.* 352(15), 1539-1549.
2. Moss AJ *et al.* (2009). Cardiac-Resynchronization Therapy for the Prevention of Heart-Failure Events. *N. Engl. J. Med.* 361(14), 1329-1338.
3. Daubert C, Behar N, Martins RP, Mabo P, Leclercq C (2017). Avoiding non-responders to cardiac resynchronization therapy: A practical guide. *Eur. Heart J.* 38(19), 1463-1472.
4. Mullens W *et al.* (2020). Optimized implementation of cardiac resynchronization therapy: a call for action for referral and optimization of care: A joint position statement from the Heart Failure Association (HFA), European Heart Rhythm Association (EHRA), and European Association. *Eur. J. Heart Fail.* 22(12), 2349-2369.
5. Auricchio A, Prinzen FW (2017). Enhancing Response in the Cardiac Resynchronization Therapy Patient: The 3B Perspective—Bench, Bits, and Bedside. *JACC Clin. Electrophysiol.* 3(11), 1203-1219.
6. McDonagh TA *et al.* (2021). 2021 ESC Guidelines for the diagnosis and treatment of acute and chronic heart failure. *Eur. Heart J.* 42(36), 3599-3726.
7. Niederer SA, Lumens J, Trayanova NA (2019). Computational models in cardiology. *Nat. Rev. Cardiol.* 16(2), 100-111.
8. Corral-Acero J *et al.* (2020). The 'Digital Twin' to enable the vision of precision cardiology. *Eur. Heart J.* 41(48), 4556-4564.
9. Gorcsan J, Anderson CP, Tayal B, Sugahara M, Walmsley J, Starling RC, Lumens J (2019). Systolic Stretch Characterizes the Electromechanical Substrate Responsive to Cardiac Resynchronization Therapy. *JACC Cardiovasc. Imaging*. 12(9), 1741-1752.
10. Leenders GE, Lumens J, Cramer MJ, De Boeck BWL, Doevendans PA, Delhaas T, Prinzen FW (2011). Septal Deformation Patterns Delineate Mechanical Dyssynchrony and Regional Differences in Contractility: Analysis of Patient Data Using a Computer Model. *Circ. Heart Fail.* 5(1), 87-96.
11. Aalen JM *et al.* (2019). Mechanism of Abnormal Septal Motion in Left Bundle Branch Block: Role of Left Ventricular Wall Interactions and Myocardial Scar. *JACC Cardiovasc. Imaging.* 12(12), 2402-2413.
12. Koopsen T *et al.* (2024). Parameter Subset Reduction for Imaging-Based Digital Twin Generation of Patients with Left Ventricular Mechanical Discoordination. *Biomed. Eng. Online*. 23(1), 46.
13. Wouters PC, Leenders GE, Cramer MJ, Meine M, Prinzen FW, Doevendans PA, De Boeck BWL (2021). Acute recoordination rather than functional hemodynamic improvement determines reverse remodelling by cardiac resynchronisation therapy. *Int. J. Cardiovasc. Imaging.* 37(6), 1903-1911.
14. Duchenne J *et al.* (2020). Acute redistribution of regional left ventricular work by cardiac resynchronization therapy determines long-term remodelling. *Eur. Heart J. Cardiovasc. Imaging.* 21(6), 619-628.
15. van Everdingen WM *et al.* (2018). Can we use the intrinsic left ventricular delay (QLV) to optimize the pacing configuration for cardiac resynchronization therapy with a quadripolar left ventricular lead? *Circ. Arrhythmia Electrophysiol.* 11(3), 1-12.
16. Maass AH *et al.* (2018). Refining success of cardiac resynchronization therapy using a simple score predicting the amount of reverse ventricular remodelling: Results from the Markers and Response to CRT (MARC) study. *Europace*. 20(2), e1-e10.

17. Strauss DG, Selvester RH, Wagner GS (2011). Defining left bundle branch block in the era of cardiac resynchronization therapy. *Am. J. Cardiol.* 107(6), 927-934.
18. Voigt JU *et al.* (2015). Definitions for a common standard for 2D speckle tracking echocardiography: consensus document of the EACVI/ASE/Industry Task Force to standardize deformation imaging. *Eur. Heart J. Cardiovasc. Imaging.* 16(1), 1-11.
19. Bogaard MD, Houthuizen P, Bracke FA, Doevendans PA, Prinzen FW, Meine M, van Gelder BM (2011). Baseline left ventricular dP/dt max rather than the acute improvement in dP/dt max predicts clinical outcome in patients with cardiac resynchronization therapy. *Eur. J. Heart Fail.* 13(10), 1126-1132.
20. de Roest GJ, Allaart CP, Kleijn SA, Delnoy PPHM, Wu L, Hendriks ML, Bronzwaer JGF, van Rossum AC, de Cock CC (2013). Prediction of long-term outcome of cardiac resynchronization therapy by acute pressure-volume loop measurements. *Eur J. Heart Fail.* 15, 299-307.
21. Aalen JM *et al.* (2020). Imaging predictors of response to cardiac resynchronization therapy: Left ventricular work asymmetry by echocardiography and septal viability by cardiac magnetic resonance. *Eur. Heart J.* 41(39), 3813-3823.
22. Brignole M *et al.* (2013). 2013 ESC Guidelines on cardiac pacing and cardiac resynchronization therapy. *Eur. Heart J.* 34(29), 2281-2329.
23. Stankovic I *et al.* (2017). The association of volumetric response and long-term survival after cardiac resynchronization therapy. *Eur. Heart J. Cardiovasc. Imaging*. 18(10), 1109-1117.
24. Huntjens PR, Walmsley J, Ploux S, Bordachar P, Prinzen FW, Delhaas T, Lumens J (2014). Influence of left ventricular lead position relative to scar location on response to cardiac resynchronization therapy: A model study. *Europace*. 16, iv62-iv68.
25. Okada J *et al.* (2017). Multi-scale, tailor-made heart simulation can predict the effect of cardiac resynchronization therapy. *J. Mol. Cell. Cardiol.* 108, 17-23.
26. Isotani A, Yoneda K, Iwamura T, Watanabe M, Okada J, Washio T, Sugiura S, Hisada T, Ando K (2020). Patient-specific heart simulation can identify non-responders to cardiac resynchronization therapy. *Heart Vessels*. 35(8), 1135-1147.
27. Crozier A *et al.* (2016). Analysis of lead placement optimization metrics in cardiac resynchronization therapy with computational modelling. *Europace*. 18, iv113-iv120.
28. Oomen PJA, Phung TKN, Weinberg SH, Bilchick KC, Holmes JW (2022). A rapid electromechanical model to predict reverse remodeling following cardiac resynchronization therapy. *Biomech. Model. Mechanobiol.* 21(1), 231-247.
29. van Stipdonk AMW *et al.* (2018). QRS Area Is a Strong Determinant of Outcome in Cardiac Resynchronization. *Circ. Arrhythmia Electrophysiol.* 11(12), e006497.
30. Gage RM, Curtin AE, Burns KV, Ghosh S, Gillberg JM, Bank AJ (2017). Changes in electrical dyssynchrony by body surface mapping predict left ventricular remodeling in patients with cardiac resynchronization therapy. *Heart Rhythm*. 14(3), 392-399.
31. Lee AWC *et al.* (2021). Non-invasive simulated electrical and measured mechanical indices predict response to cardiac resynchronization therapy. *Comput. Biol. Med.* 138, 104872.
32. Meiburg R *et al.* (2023). Comparison of novel ventricular pacing strategies using an electro-mechanical simulation platform. *Europace*. 25(6), 1-11.

33. Taylor RJ, Umar F, Panting JR, Stegemann B, Leyva F (2016). Left ventricular lead position, mechanical activation, and myocardial scar in relation to left ventricular reverse remodeling and clinical outcomes after cardiac resynchronization therapy: A feature-tracking and contrast-enhanced cardiovascular magnetic resonance study. *Heart Rhythm*. 13(2), 481-489.

SUPPLEMENTARY MATERIAL

Digital Twin generation algorithm

A total of 75 model parameters were personalized to generate the Digital Twin. These 75 parameters included three global parameters and four parameters estimated in eighteen LV wall segments. The four segmental parameters included mechanical activation delay dT, reference mid-wall area $A_{w,ref}$, zero-passive stress length $L_{s0,pas}$, and stiffness coefficient k. Furthermore, cardiac output q_0 was personalized, as well as global LV activation duration offset ADO and atrioventricular (AV) delay relative to the model intrinsic delay τ_{AV}. In the section 'The CircAdapt model of the human heart and circulation' of this Supplementary material, these parameters are explained further based on the model governing equations.

Parameters were optimized by minimizing the mean squared error χ^2, which was defined as the mean squared error in end diastolic volume $\chi^2_{V_{ED}}$, ejection fraction χ^2_{EF}, 18 strain traces χ^2_{ε}, and 18 strain rate traces $\chi^2_{\dot{\varepsilon}}$:

$$\chi^2 = \frac{\chi^2_{V_{ED}} + \chi^2_{EF} + \chi^2_{\varepsilon} + \chi^2_{\dot{\varepsilon}}}{38} \tag{S5.1}$$

Error contributor $\chi^2_{V_{ED}}$ describes the error between modelled and measured end diastolic volume $V_{ED,mod}$ and $V_{ED,mea}$, respectively) weighted by $\sigma_{V_{ED}}$:

$$\chi^2_{V_{ED}} = \left(\frac{V_{ED,mod} - V_{ED,mea}}{\sigma_{V_{ED}}}\right)^2, \tag{S5.2}$$

Error contributor χ^2_{EF} describes the error between modelled and measured ejection fraction (EF_{mod} and EF_{mea}, respectively) weighted by σ_{EF}:

$$\chi^2_{EF} = \left(\frac{EF_{mod} - EF_{mea}}{\sigma_{EF}}\right)^2, \tag{S5.3}$$

Normalization constants $\sigma_{V_{ED}}$ and σ_{EF} were assumed to be proportional to the measured value and equaled $0.13 \cdot V_{ED,mea}$ and $0.14 \cdot EF_{mea}$, respectively [1].

Error contributor χ^2_{ε} describes the error between modelled and measured strain $\varepsilon_{i,mod}$ and $\varepsilon_{i,mea}$, respectively) weighted by σ_{ε_i} and averaged over all data points n_{dp}.

$$\chi^2_{\varepsilon} = \sum_{i=1}^{n_{seg}} \left(\frac{1}{n_{dp}} \sum_{k=1}^{n_{dp}} \left(\frac{\varepsilon_{i,mod}(k) - \varepsilon_{i,mea}(k)}{\sigma_{\varepsilon_i}} \right)^2 \right), \tag{S5.4}$$

Error contributor $\chi^2_{\dot{\varepsilon}}$ describes the error between modelled and measured strain rate ($\dot{\varepsilon}_{i,mod}$ and $\dot{\varepsilon}_{i,mea}$, respectively) weigthed by $\sigma_{\dot{\varepsilon}_i}$ and averaged over all data points n_{dp}.

$$\chi_{\dot{\varepsilon}}^2 = \sum_{i=1}^{n_{seg}} \left(\frac{1}{n_{dp}} \sum_{k=1}^{n_{dp}} \left(\frac{\dot{\varepsilon}_{i,mod}(k) - \dot{\varepsilon}_{i,mea}(k)}{\sigma_{\dot{\varepsilon}_i}} \right)^2 \right). \quad \text{(S5.5)}$$

Only strain from mitral valve closure till 10% global re-lengthening + 50 ms was included in the cost function, thereby excluding late diastolic strain. Simulated strain signals $\varepsilon_{i,mod}$ were obtained by scaling simulated fiber strain $\varepsilon_{i,mod,f}$ to the amplitude of the longitudinal strain measurements of the patient:

$$\varepsilon_{i,mod,f}(t) = \frac{L_{s,i}(t) - L_{s,i}(t_0)}{L_{s,i}(t_0)} \cdot 100\%, \quad \text{(S5.6)}$$

$$\varepsilon_{i,mod} = \frac{\varepsilon_{glob,mea}}{\varepsilon_{glob,mod,f}} \cdot \varepsilon_{i,mod,f}. \quad \text{(S5.7)}$$

Here, $L_{s,i}(t)$ is the sarcomere length of segment i at time t, while t_0 is the timing of mitral valve closure. Furthermore, $\varepsilon_{glob,mea}$ and $\varepsilon_{glob,mod,f}$ are the measured and simulated peak values of the global strain signal, i.e., the average strain signal of all 18 LV segments. Simulated strains and strain rates were also resampled to the sampling frequency of ε_{mea}. Measurement uncertainties σ_ε and $\sigma_{\dot{\varepsilon}}$ were chosen to equal 2% and 20%/s, respectively. Cycle time within the model (t_{cycle}) was fixed to the average cycle time t_{cycle} of all three echocardiographic acquisitions.

The optimization algorithm used was dynamic multi-swarm particle swarm optimization (DMS-PSO) [2]. A total of 60 particles were used, subdivided into 20 swarms of three particles. Every 20 iterations, swarms were randomly regrouped. The initial particle positions were determined by performing 1,000 Monte Carlo (MC) simulations using the ranges shown in Supplementary Table 5.1. To prevent non-realistic simulations, however, additional restrictions on the severity of electrical dyssynchrony, global LV contractility and stiffness were imposed. The 60 particles with the lowest cost function values χ^2 were selected as initial particle positions.

During iterations of DMS-PSO, extended parameter boundaries were used (Supplementary Table 5.1) as compared to those for MC simulations to improve algorithm performance. For particles outside these boundaries, the cost function was infinite. Particle velocities were limited to 25% of the input space width to prevent particles from oscillating outside the input space. DMS-PSO was stopped when normalized particle energies were lower than 10^{-4}, meaning no parameter changed more than 1% of its input space width within one iteration, or when a maximum number of 2,000 iterations were completed.

The CircAdapt model of the human heart and circulation

The CircAdapt model of the human heart and circulation is a closed-loop lumped-parameter model which simulates beat-to-beat hemodynamics and mechanics of the heart and blood vessels [3]. In this paper, we used the model build as described by Walmsley et al. [4] which

later was implemented in c++ to improve performance [5]. The pulmonary and systemic circulation are modeled using a three-element model of resistive wave impedance, compliance, and peripheral resistance [6]. Cardiac walls are modelled as spherical shells, and the left and right ventricular walls are coupled through the interventricular septum in the TriSeg geometry [7]. In this geometry, wall tension T_w was linearized based on the mid-wall surface area A_w:

$$T_w(t) = \frac{V_w \cdot \sigma_f(t)}{2 \cdot A_w(t)} \tag{S5.8}$$

Here, V_w is the wall volume, while $\sigma_f(t)$ represents myofiber stress which is a function of natural myofiber strain $\varepsilon_f(t)$. Furthermore, z is a dimensionless curvature parameter which is closely related to the ratio of wall thickness to radius of curvature. The relation between $\varepsilon_f(t)$ and $A_w(t)$ is determined by a reference wall area $A_{w,ref}$, which is defined as the area at a reference sarcomere length $L_{s,ref} = 2\ \mu m$:

$$\varepsilon_f(t) = \frac{1}{2}\ln\left(\frac{A_w(t)}{A_{w,ref}}\right) \tag{S5.9}$$

Natural myofiber strain $\varepsilon_f(t)$ determines sarcomere length $L_s(t)$ by:

$$L_s(t) = L_{s,ref} \cdot e^{\varepsilon_f(t)} \tag{S5.10}$$

Active and passive myofiber stress $\sigma_{f,act}(t)$ and $\sigma_{f,pas}(t)$ are calculated based on $L_s(t)$ using a three-element Hill contraction model. In this model, $\sigma_{f,act}(t)$ is calculated by:

$$\sigma_{f,act}(t) = S_{f,act} \cdot C(t) \cdot \left(L_{si}(t) - L_{si,0}\right) \cdot \frac{L_{se}(t)}{L_{se,iso}} \tag{S5.11}$$

where $S_{f,act}$ scales active stress development, while $C(t)$ is a state variable representing the density of cross-bridge formation. Furthermore, $L_{si}(t)$ represents the contractile element length, which has a zero-active stress reference length $L_{si,0} = 1.51\ \mu m$. Variable $L_{se}(t)$ is the length of the series elastic element, which is scaled with a reference length of $L_{se,iso} = 0.04\ \mu m$ defined at the onset of isovolumetric contraction. Variable $C(t)$ is described by the following differential equation:

$$\frac{dC}{dt} = \frac{1}{\tau_r} C_L(L_{si}(t)) \cdot F_{rise}(t) - \frac{1}{\tau_d} \cdot C(t) \cdot g(X) \tag{S5.12}$$

In this differential equation, the time constants τ_r and τ_d scale the rise and decay of $C(t)$, respectively. The function $C_L(L_{si})$ describes the increase of force development with sarcomere length, and $F_{rise}(t)$ describes the time-dependent rise of mechanical activation. The term $g(X)$ causes a delay in the decay of contractility. It holds:

$$X = \frac{t_c - t_A}{\tau_d} \tag{S5.13}$$

with $t_c = t - t_{act}$ the time elapsed since onset of activation t_{act}, and t_A the duration of activation. This duration of activation is determined by a length-independent offset ADO as well as a length-dependent parameter $LDAD$:

$$t_A = \left(ADO + LDAD \cdot \frac{L_{si}(t)}{L_{si,0}}\right) \cdot T_a \tag{S5.14}$$

where T_a is a factor scaling the contraction duration.

Passive stress $\sigma_{f,pas}(t)$ includes two components:

$$\sigma_{f,pas}(t) = \sigma_{f,tit}(t) + \sigma_{f,ECM}(t) \tag{S5.15}$$

where $\sigma_{f,tit}(t)$ is the stress that arises from the myocytes themselves due to intracellular structures such as titin, and $\sigma_{f,ECM}(t)$ is the stress resulting from the extracellular matrix (ECM). The intracellular component $\sigma_{f,tit}(t)$ is defined by:

$$\sigma_{f,tit}(t) = 0.01 \cdot S_{f,act} \cdot \left(\lambda_p(t)^{20/3} - 1\right) \tag{S5.16}$$

while the ECM component $\sigma_{f,ECM}(t)$ is calculated as:

$$\sigma_{f,ECM}(t) = S_{f,pas} \cdot \left(\lambda_p(t)^k - 1\right) \tag{S5.17}$$

Here, $S_{f,pas}$ is a scaling factor, while k determines the non-linearity of the relation between $\lambda_p(t)^k$ and $\sigma_{f,ECM}(t)$. Variable $\lambda_p(t)$ is calculated as:

$$\lambda_p(t) = \frac{L_s(t)}{L_{s0,pas}} \tag{S5.18}$$

with $L_s(t)$ being sarcomere length and $L_{s0,pas}$ the zero-passive stress length.

Supplementary Table 5.1: Overview of the 75 parameters personalized and their boundaries used during Monte Carlo (MC) simulations and dynamic multi-swarm particle swarm optimization (DMS-PSO). glob, global LV parameter; seg, segmental LV parameter; S, septum; LVfw, LV free wall; $t_{cycle,mea}$, measured cycle time.

Parameter	Number of parameters	Physiological meaning	Unit	Lower bound (MC)	Upper bound (MC)	Lower bound (DMS-PSO)	Upper bound (DMS-PSO)
q_0	1	Cardiac output	L/min	2.1	5.5	1	20
τ_{AV}	1	Atrioventricular delay relative to model intrinsic delay	s	-0.050	0.130	-0.100	0.200
ADO (glob)	1	Activation duration offset	s	0.52	0.78	0	$2^*t_{cycle,mea}$
dT (seg)	18	Mechanical activation delay	s	-0.030 (S) 0.000 (LVfw)	0.060 (S), 0.120 (LVfw)	-0.060 (S) -0.060 (LVfw)	0.120 (S), 0.200 (LVfw)
$A_{w,ref}$ (seg)	18	Reference wall area	cm^2	16/3	35/3	1.6 (S) 1.6 (LVfw)	24.4 (S) 24.5 (LVfw)
$L_{s0,pas}$ (seg)	18	Zero-passive stress length	µm	1.63	1.99	0	3
k (seg)	18	Stiffness coefficient	-	6.4	36	0	100
	75						

REFERENCES

1. Otterstad JE, Froeland G, St John Sutton M, Holme I (1997). Accuracy and reproducibility of biplane two-dimensional echocardiographic measurements of left ventricular dimensions and function. *Eur. Heart J.* 18(3), 507-513.
2. Liang JJ, Suganthan PN (2005). Dynamic multi-swarm particle swarm optimizer. *Proc. 2005 IEEE Swarm Intell. Symp.* 124-129.
3. Arts T, Delhaas T, Bovendeerd P, Verbeek X, Prinzen FW (2004). Adaptation to mechanical load determines shape and properties of heart and circulation: the CircAdapt model. *Am. J. Physiol. Heart Circ. Physiol.* 288(4): H1943-H1954.
4. Walmsley J, Arts T, Derval N, Bordachar P, Cochet H, Ploux S, Prinzen FW, Delhaas T, Lumens J (2015). Fast Simulation of Mechanical Heterogeneity in the Electrically Asynchronous Heart Using the MultiPatch Module. *PLoS Comput. Biol.* 11(7), 1-23.
5. van Osta N *et al.* (2020). Parameter subset reduction for patient-specific modelling of arrhythmogenic cardiomyopathy-related mutation carriers in the CircAdapt model. *Phil. Trans. R. Soc. A*. 378(2173), 20190347.
6. Arts T, Reesink K, Kroon W, Delhaas T (2012). Simulation of adaptation of blood vessel geometry to flow and pressure: Implications for arterio-venous impedance. *Mech. Res. Commun.* 42, 15-21.
7. Lumens J, Delhaas T, Kirn B, Arts T (2009). Three-wall segment (TriSeg) model describing mechanics and hemodynamics of ventricular interaction. *Ann. Biomed. Eng.* 37(11), 2234-2255.

6

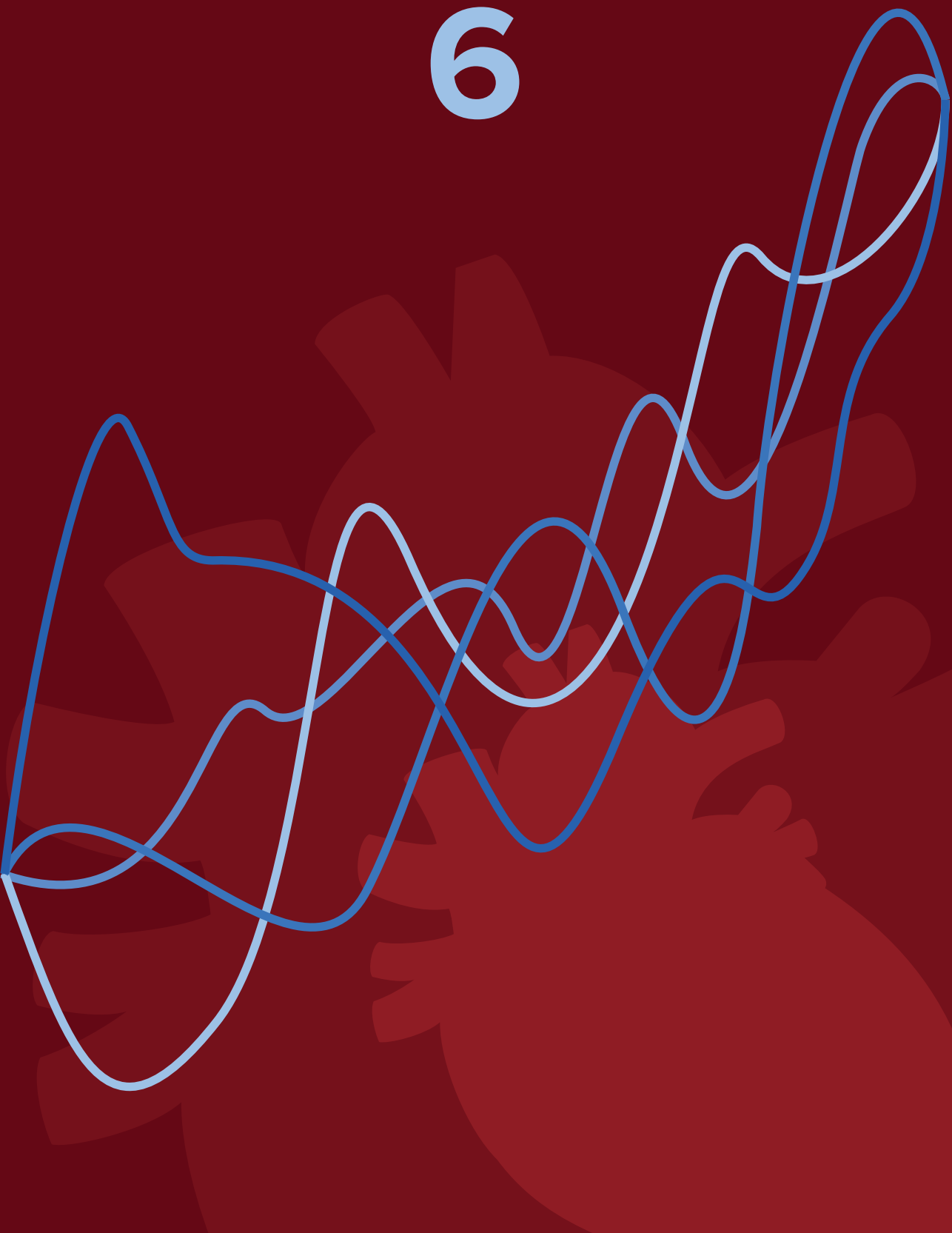

General Discussion

The aims of this thesis were to obtain more insight into the electro-mechanical myocardial disease substrates of dyssynchronous heart failure (HF) patients and to investigate whether integrative imaging-based characterization of the patient's disease can help to predict response to cardiac resynchronization therapy (CRT). To achieve these aims, we developed an algorithm which automatically personalized the CircAdapt model to a patient's non-invasive myocardial deformation measurements, thereby generating the patient's Digital Twin. We then simulated biventricular pacing in the Digital Twin to quantify virtual therapy response as a potential predictor of CRT response of the real patient, represented by the extent of left ventricular (LV) reverse remodeling at follow-up. This two-step approach is illustrated in Figure 6.1, which summarizes the clinical workflow of CRT implantation and the Digital Twin workflow that was used in this thesis.

In this concluding chapter, we discuss the insights that were obtained in this thesis in a broader context and we elaborate on the potential of the Digital Twin for future application in the field of pacemaker therapy. Following the content of Figure 6.1, we will discuss the potential and the limitations of the Digital Twin approach as a diagnostic support tool (DIAGNOSIS) and a therapeutic support tool (PREDICTION), and why these two fields of application are highly interdependent. Based on the important conclusion that the development of a Digital Twin should be in line with its context of use (COU), we also re-evaluate the methodologies used in this thesis and we propose potential improvements to the Digital Twin technology. Finally, we discuss the clinical and societal impact of the research included in this thesis.

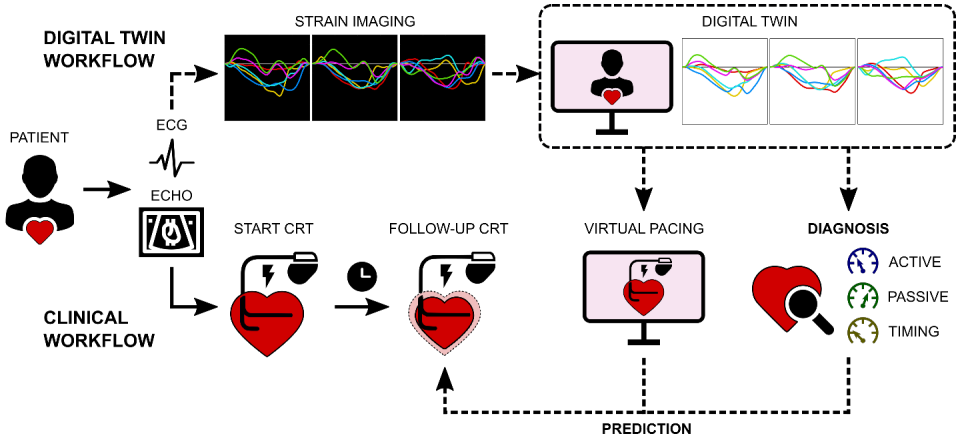

Figure 6.1: Schematic overview of the clinical workflow of cardiac resynchronization therapy (CRT) delivery (solid arrows) and the workflow used in this thesis to investigate the role of the Digital Twin to support this clinical CRT delivery (dashed arrows). In **Chapters 2**,**3**, and **4**, the main focus was on the development of a Digital Twin which extracts relevant diagnostic information from non-invasive left ventricular (LV) cavity volume and regional strain measurements (DIAGNOSIS). Then, in **Chapter 5**, this Digital Twin was used to predict the clinical effect of CRT (PREDICTION), where clinical effect was quantified by the extent of LV reverse remodeling at follow-up (FOLLOW-UP CRT). This prediction was performed by calculating a baseline diagnostic index of the Digital Twin (pathway: DIAGNOSIS), and by simulating a virtual pacing intervention in the Digital Twin (pathway: VIRTUAL PACING).

6.1 DIGITAL TWIN OF THE FAILING HEART ENABLES TISSUE CHARACTERIZATION (DIAGNOSIS)

Dyssynchronous HF patients often have a complex electro-mechanical disease substrate which is characterized by electrical and non-electrical myocardial tissue abnormalities [1]. Obtaining more insight into this electro-mechanical disease substrate is important to determine the potential of CRT [2]. In this thesis, we hypothesized that a patient's unique combination of LV regional strain patterns could reveal the electro-mechanical tissue properties underlying mechanical dyssynchrony (**Chapter 1**). The Digital Twin was used to extract these patient-specific myocardial tissue properties from LV regional strain and cavity volume measurements.

One of the tissue properties which plays an important role in HF and response to CRT is myocardial contractility. Development of HF is accompanied with ventricular remodeling processes which impair the contractile function of the myocardium [1,3]. Furthermore, myocardial infarction (MI) is a common cause of HF and involves a regional loss of tissue contractility and viability [4,5]. Heart failure patients who have extensive myocardial scarring improve less or are even harmed by CRT, despite having a wide QRS complex [6]. Similarly, studies have associated the presence of contractile reserve with an increased chance of CRT response [7,8]. Beside global myocardial viability, the location of MI is important since lead placement in scar tissue should be avoided [9-11].

Our Digital Twins of patients with narrow QRS complexes showed that contractility was reduced in myocardial segments with an increased percentage of late gadolinium enhancement (LGE), indicating scar [12] (**Chapter 3**). Contractility was represented by the non-contractile volume fraction ($NCVF$) which was based on a two-compartment model of regional ischemia as described by Sunagawa et al. [13]. In this thesis, we have shown that this parameter was more representative for acute and chronic MI as compared to the active stress constant $S_{f,act}$ (**Chapter 3**). Compared to $S_{f,act}$, $NCVF$ had a more linear relation with myocardial deformation indices which have previously been used as markers for scar, i.e. peak systolic strain, systolic pre-stretch, and post-systolic shortening [14-17]. We therefore concluded that $NCVF$ can provide a quantitative measure of ischemic dysfunction.

However, preliminary estimations of $NCVF$ in dyssynchronous HF patients demonstrated several limitations. First of all, the combination of $S_{f,act}$ and $NCVF$ was non-identifiable from the measurement data, while global LV hypocontractility was more accurately simulated by $S_{f,act}$ than by $NCVF$. Since global LV contractility in HF is often reduced as a consequence of impaired Frank-Starling reserve [3], $S_{f,act}$ was considered essential to simulate global ventricular mechanics. Second, due to the lack of LV end-diastolic pressure data in the measurement set used, the stiffness coefficients of the non-contractile compartments were non-identifiable. Third, the similarity between measured and simulated strain patterns of dyssynchronous HF patients was generally lower when using the two-compartment model of contractile dysfunction. Global increments of $NCVF$ had a dampening effect on the regional

strain patterns, explained by the averaging between an active and a passive segment, which caused less dynamic myocardial strain behavior. Consequently, we decided to generate Digital Twins of dyssynchronous HF patients using a one-compartment implementation of contractile dysfunction, at the cost of losing the interpretability of $NCVF$ (**Chapter 4**).

Based on the structural and functional implications of MI [4,18], we hypothesized that myocardial segments with more than 25% of LGE would demonstrate abnormal active and passive parameter values. In the final subset obtained in **Chapter 4**, contractility was scaled by a parameter of the passive tissue model, i.e., the zero-passive stress length. This zero-passive stress length scaled the operating length of the sarcomere and therefore also the generation of active force. At the same time, passive myocardial stiffness was scaled by the passive stiffness coefficient. The three ischemic HF patients that we included in **Chapter 4** did not consistently show deviating values of these parameters in scarred segments as compared to remote segments. Since these parameters represent intrinsic properties of the myocardium, we have concluded that the currently used LV strain and volume data are too limited to differentiate between intrinsic active and passive tissue properties. However, segments with a reduced contractility, meaning a load-dependent contractility in this case, may still be indicative of MI. A similar result was obtained in a modeling study of three dyssynchronous HF patients which showed a slightly stronger association between estimated contractility parameters and location of LGE [19].

In contrast to the individual model parameters, the LV myocardial work (MW) distribution of the Digital Twin was highly representative for the underlying myocardial disease substrate of the patient (**Chapter 4**). Digital Twins of patients with an isolated LBBB substrate demonstrated an asynchronous MW pattern, with more work performed by the lateral wall than by the septum, as is characteristic for LBBB [20,21]. This asynchronous MW distribution was also observed for patients with LBBB and MI, but it was modulated by the presence of MI. This modulation was most evident for one of the patients with a severe anteroseptal scar, whose Digital Twin showed a reduced MW in the area of MI. A similar interaction between LBBB and MI has been demonstrated in dogs as well as in HF patients [21].

The global LV reference wall area of our Digital Twins correlated strongly with LV end-diastolic volume of the patients and therefore did not provide additional insights into the underlying mechanisms of ventricular dilatation. While we hypothesized in **Chapter 2** that an increased LV eccentric remodeling as represented by an increased reference wall area could provide a remodeling that is reversible by CRT, we thus observed no independent information included in this parameter. Adding other measurement data would potentially provide more insights into these mechanisms of LV dilatation, on which we will elaborate later during this discussion.

6.2 DIGITAL TWIN CAN SUPPORT CRT PATIENT SELECTION (PREDICTION)

As a first step to determine whether a patient is eligible for CRT, the 12-lead ECG remains important as a fast and widely accessible measurement of the patient's electrical conduction function [22]. Patients with a QRS width≥150 ms and LBBB morphology are highly likely to benefit from CRT [23,24]. However, in patients with intermediate QRS criteria, i.e., a QRS width of 130-149 ms or non-LBBB morphology, there is a large variability in CRT outcome. This variability asks for improved selection criteria which are based on additional clinical measurements.

The Digital Twins in this thesis were developed using LV cavity volume and 18-segment myocardial strain measurements. The resulting virtual representation of the patient's heart was used to virtually quantify CRT response potential. In **Chapter 5**, we showed that the Digital Twin's baseline septal-to-lateral MW imbalance was significantly associated with the patient's degree of LV reverse remodeling six months after CRT. A similar positive correlation between baseline LV workload imbalance and CRT response has been obtained in clinical studies which used non-invasive approximations of work [25,26]. This association is explained by a large baseline MW imbalance representing a significant intraventricular activation delay in combination with a relatively preserved contractile function of the septum and LV free wall. This same rationale holds for the systolic stretch index (SSI) which has shown to have additional value in predicting CRT response on top of ECG parameters [2,27].

Application of virtual pacing in the Digital Twin showed that the pacing-induced reduction of septal-to-lateral MW imbalance correlated significantly with real-world post-CRT LV reverse remodeling (**Chapter 5**). A similar relation between redistribution of MW and LV reverse remodeling has been observed in real patients [26,28]. This integrative approach which combines the Digital Twin with virtual pacing provides a new strategy for selecting patients for CRT, based on the virtually predicted interaction of the patient's cardiovascular system with pacemaker therapy. Further validation of this Digital Twin technology remains necessary, but our results in **Chapter 5** show the potential of virtual pacing as an additional tool to select patients for CRT.

Future research could further investigate which model-derived indices predict CRT response most accurately. In this thesis, we have focused on LV workload imbalance reduction since this index was more predictive for LV reverse remodeling than acute hemodynamic response (AHR), where the latter was quantified by the acute increase of LV dp/dt_{max} (**Chapter 5**). The relation between AHR and long-term outcome of CRT remains uncertain, as is demonstrated by conflicting results in both clinical [28-32] and computational studies [33,34].

The reason why MW may be a stronger predictor of LV reverse remodeling than AHR is that MW depends on several factors which are known to determine this remodeling.

For example, a typical LBBB electro-mechanical activation pattern [20], myocardial scarring [21,25], and global myocardial contractility [8] all determine the amount of MW that is performed by the septum and lateral wall during LBBB. Furthermore, MW is determined by stress and strain which have been identified as triggers for structural adaptation [35,36]. The distribution of MW may therefore be more closely related with a ventricular remodeling response than hemodynamic parameters [37].

While occurrence of LV reverse remodeling has shown to have a strong association with survival [38], reverse remodeling is not the only relevant outcome measure to define CRT response. In the clinic, a positive CRT response is also often defined as a reduction of HF symptoms or an improvement in quality of life. Other CRT response measures focus on the occurrence of adverse events or composite endpoints [39]. We did not currently validate our Digital Twin approach against these other outcome variables, but it would be valuable to do so in future studies.

A recently published position statement of the European Society of Cardiology advocates for replacing the term 'CRT response' by the concept of 'disease modification' [40]. The authors emphasize that HF is often incurable and that the focus of quantifying the effect of CRT may be too much on improvement of cardiac function as opposed to stopping or slowing down disease progression. Indeed, 'CRT response' is a controversial term, and studies have shown that patients who stabilize early after CRT have a better survival than those who worsen over time [41]. The importance of disease stabilization as a positive outcome may currently be underestimated.

This discussion about CRT response is relevant in the context of our Digital Twin approach. Similar as for the degree of LV reverse remodeling, the results in **Chapter 5** show that the Digital Twin's pacing-induced septal-to-lateral MW imbalance reduction represents a continuous rather than a binary variable. While some Digital Twins only show a relatively small reduction of this workload imbalance, a small improvement can be important to the patient. Cutoffs for clinical decision making are often based on population averages. When considering LV reverse remodeling, for example, a positive CRT response is usually defined as a reduction of LV end-systolic volume by ≥15% [39]. However, the rationale of the Digital Twin is that it follows a personalized rather than a population-based approach, and a Digital Twin should therefore ideally be its own control. If HF is progressing, stabilizing of disease progression could be interpreted as a positive result.

In Figure 6.2, we have reprinted the results of our Digital Twin technology obtained in **Chapter 5**, but now according to the CRT classification guidelines of the European Society of Cardiology (ESC) published in 2013 [42] and in 2021 [43]. As can be observed, the criteria have become more conservative, leading to a shift of fifteen patients from a Class I indication for CRT in 2013 to a Class IIa or IIb indication in 2021. For these fifteen patients, the Digital Twin technology showed a strong correlation ($r=0.82$, $P<0.001$) between their predicted and actual CRT response. The majority of these patients experienced even >15% decrease of LVESV after six months, suggesting that the stricter LBBB definition as used in the 2021

guidelines may lead to CRT being withheld in patients who would significantly benefit from the therapy. In addition, this result shows that the imaging-based Digital Twin may be able to provide an additional tool to predict CRT response on top of QRS duration and morphology.

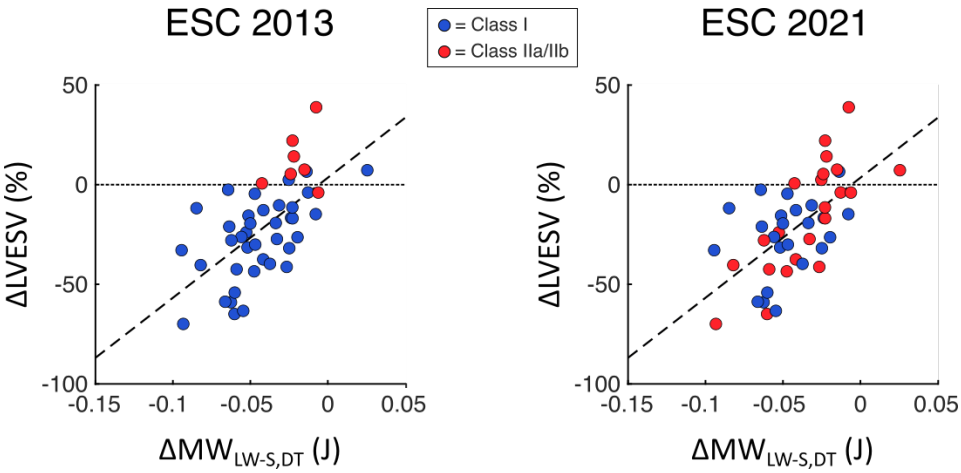

Figure 6.2: Correlation plots of virtual pacing-induced reduction of septal-to-lateral myocardial work imbalance in the Digital Twin ($\Delta MW_{LW\text{-}S,DT}$) versus LV end-systolic volume reduction after six months (ΔLVESV), where the patient population is classified according to the European Society of Cardiology (ESC) guidelines for CRT published in 2013 [42] and in 2021 [43].

6.3 FUTURE PERSPECTIVE: DIGITAL TWINS TO SUPPORT CLINICAL DECISION MAKING

The ultimate goal of developing Digital Twins in healthcare often includes their contribution to clinical decision making [44,45]. In this thesis, we have evaluated several strategies to do so (see Figure 6.1) and these strategies have been discussed in the previous sections. In this section, we will elaborate on the steps which can be taken to further improve the Digital Twin technology and to make it even more valuable for clinical application. We have subdivided these steps according to a few common challenges which have been described for developing Digital Twins [46]. First, we will zoom in on the Digital Twin's COU, after which we will discuss the model parameters estimated, the measurement data obtained and the model and optimization algorithm used.

6.3.1 Expanding the context of use

The specific approach by which a model is used to address a clinical problem is defined as the COU [46]. In **Chapter 5** of this thesis, our COU was to calculate the Digital Twin's baseline septal-to-lateral MW imbalance and to quantify the amount of reduction of this

MW imbalance which was achieved acutely by virtual pacing. However, the Digital Twin technology can be applied to other COUs to further support the current clinical practice of pacemaker therapy.

In addition to guiding the selection of patients for CRT, the Digital Twin provides a platform to optimize therapy delivery in HF patients [44]. In recent years, several strategies have been developed and tested to optimize atrioventricular (AV) and interventricular (VV) delay [47,48] as well as LV lead location [49-51] during CRT. Furthermore, other pacing strategies are currently being explored, including conduction system pacing (CSP) which shows to be a promising alternative to conventional CRT [43,52,53]. The CircAdapt model enables tweaking of pacing settings and has previously been used to perform generic simulation studies on AV and VV delay [54,55] as well as on LV lead location [11] during CRT. Recently, CircAdapt was used to develop a simulation framework of other pacing strategies including CSP [56]. Virtual pacing of the Digital Twin can reveal the interaction between pacemaker settings and the unique electro-mechanical disease substrates of the patient. Thereby, this Digital Twin-pacing framework has the potential to guide pacemaker therapy delivery by determining optimal settings prior to device implantation.

Patient-specific simulation approaches for pacemaker therapy have already been successfully implemented by other research groups [33,34,57-62]. These studies have shown that virtual pacing can be used to identify preferred LV lead locations and device settings. While a more extensive validation of these modeling approaches may remain essential, these approaches show the potential to use personalized models of pacing to support the clinical implantation procedure.

6.3.2 Reconsidering the subset of model parameters

Sensitivity and identifiability analyses are key in determining which model parameters are relevant for personalization. The input and output of the model in these analyses should be guided by the COU. Our objective in **Chapter 4** was to derive as much diagnostic information as possible from non-invasive LV cavity volume and regional strain measurements, meaning that the model output was already decided upon. This objective differed from the eventual COU in **Chapter 5**, which included the calculation of septal-to-lateral workload imbalance reduction by virtual pacing. In a new study setup, the sensitivity of estimated Digital Twin parameters to the pacing-induced LV workload imbalance reduction could be quantified. Such a sensitivity analysis may be performed as an alternative or supplemental approach to inform the choice of the final parameter subset.

6.3.3 Adding measurement data

Regional MW has been shown to depend on afterload and this dependence is larger during LBBB [64]. Using LV cavity volume and regional strain measurements, mean arterial pressure (MAP) was non-identifiable (**Chapter 4**), and therefore it was set to its reference value of 92 mmHg in all Digital Twins. Adding arterial pressure measurements of the patient could lead

to a better estimation of MW, which may further improve predictivity for CRT response. For example, an arm-cuff could be used to measure blood pressure during echocardiographic imaging.

Furthermore, flow velocity patterns of the mitral valve may allow a more accurate estimation of passive myocardial tissue properties [65]. When passive tissue properties are estimated more accurately, also active myocardial tissue properties can be more accurately estimated. Alternatively, including the diastolic part of the myocardial strain patterns may enable estimation of passive tissue properties. In the current Digital Twin approach, we chose to exclude these diastolic parts of the strain signals since these parts are often subjected to a significant amount of drift compensation [66], thereby potentially increasing measurement uncertainty. Future studies can evaluate how diastolic strain can successfully be incorporated into the Digital Twin technology.

Rather than using a single imaging modality to construct Digital Twins, as was done in this thesis by using echocardiography, Digital Twins may be improved by using input information from different imaging sources. Such a multi-modality Digital Twin follows multi-modality imaging approaches which are now increasingly evaluated in the clinic to improve patient selection for CRT [67]. For example, supplementing the assessment of mechanical dyssynchrony by echocardiography with septal scar extent by CMR has been shown to improve prediction of response to CRT [25]. At the same time, it should be noted that using more data to develop a Digital Twin may involve additional measurement uncertainty as well as a potential model discrepancy. It is key in this case to investigate the propagation of measurement uncertainty into variables which are used for clinical decision support [68,69].

Beside the measurements which are integrated into the Digital Twin itself, the Digital Twin could be supplemented with measurements which have already been shown to be predictive for CRT outcome, such as QRS area [70]. After all, CRT is an electrical therapy and our current approach only integrates non-electrical measurements into the Digital Twin. Potentially, a multivariate model could be constructed consisting of the baseline or virtual pacing-induced reduction of septal-to-lateral workload imbalance derived from the Digital Twin and baseline electrical characteristics. It remains to be investigated to what extent these measurements provide independent prognostic information.

6.3.4 Developing new cardiac models

The CircAdapt model which was used in this thesis includes a phenomenological description of active force development [71]. Electro-mechanical interactions are not included in this model, but may play an important role in dyssynchronous HF patients and their response to CRT [1]. In the future, a more detailed model of myocardial electrical activation could be included. For example, instead of assuming radial wave propagation during virtual CRT as we did in **Chapter 5**, a model of electrical wave propagation could be used to simulate CRT more realistically [56]. Using such a model would also allow personalization of regional myocardial conductive properties, for example by reducing the conduction velocity in

hypocontractile segments which may indicate infarction [4,72]. Furthermore, these wave propagation models could be more accurate to evaluate the effects of different LV lead locations [57] and pacing strategies such as CSP [60]. Moreover, these models may allow prediction of the risk of arrhythmic events during pacing, which was beyond the scope of the current research. Arrhythmic risk prediction has been shown to be feasible in personalized heart models which take into account regional myocardial conductive properties based on CMR-derived location of myocardial scar tissue [73,74].

Mechanistic models of the heart can also be coupled with growth and remodeling models to simulate CRT-induced remodeling [75]. These growth and remodeling models can provide more insight into the mechanical triggers responsible for reverse remodeling and the relation with other response parameters. While these models are often complex and therefore challenging to personalize, such models can be powerful tools to further improve CRT patient selection and therapy delivery.

6.3.5 Optimizing optimization

Dynamic multi-swarm particle swarm optimization (DMS-PSO) can deal with complex non-linear parameter spaces and this algorithm showed to produce patient-resembling Digital Twins in this thesis. However, the algorithm yields a single point estimate of all parameters, agreeing with the best match between patient and Digital Twin. A better match between patient and Digital Twin does not necessarily mean that a better prediction of therapy response is obtained. Furthermore, LV cavity volume and regional strain measurements are known to include measurement uncertainty. Given these two arguments, it would be useful to investigate the propagation of the Digital Twin's objective function value into the accuracy of clinical predictions.

A potential strategy to do so is to calculate parameter distributions by using Bayesian methods [76]. These distributions provide insight into the uncertainty of model parameter estimations. It may then be investigated how these parameter uncertainties propagate into uncertainty of predictive indices of the Digital Twin, e.g. the baseline septal-to-lateral workload imbalance or the virtual pacing-induced reduction thereof.

While DMS-PSO performed relatively fast for the purpose of research as it generated the patient's Digital Twin on average within 24 hours, its optimization is not the most cost-effective since this algorithm converges rather slow. DMS-PSO is especially effective within early iterations and for most of the patients a visually similar Digital Twin was obtained already after 4 hours. Potentially, DMS-PSO could be combined with other optimization algorithms to speed up the optimization process and make the Digital Twin technology even more suitable for clinical application.

6.4 IMPACT

Heart failure (HF) is a significant health problem in our society. In developed countries, the current prevalence of HF is 1-2% of the adult population. While management of cardiovascular diseases has improved over the last years, HF incidence continues to increase due to ageing of the population [77]. In humans aged 65 years or over, HF prevalence has been reported to be more than 5% [78].

Patients with HF frequently suffer from disease symptoms including dyspnea and fatigue, which significantly impact their daily activities and quality of life. Over time, these symptoms also often become worse due to disease progression, especially in those patients with acute HF. Timely diagnosis and intervention are essential to prevent worsening of patient prognosis and a reduced chance of treatment success [79].

In this section, we discuss more extensively the potential impact of our Digital Twin technology on HF management.

6.4.1 Diagnosis of patients with cardiovascular disease

The presented Digital Twin technology was developed to obtain insight into the myocardial disease substrates of dyssynchronous HF patients. These insights were used to identify HF patients who are likely to benefit from CRT. However, since the technology was developed as a diagnostic support tool, its field of application may be wider. The technology can potentially be used as a diagnostic tool in patients with various cardiovascular diseases, not limited to HF. For example, we showed that the technology could determine myocardial contractile function in non-HF patients with MI. The estimated tissue parameters of the Digital Twin may be useful to improve diagnosis of these patients and to better predict the risk of HF development at a relatively early stage.

6.4.2 Monitoring disease progression and therapeutic effect

A Digital Twin of the patient can be generated at each preferred moment in time, based on the acquisition of echocardiographic imaging data. Thereby, the technology can contribute to monitoring of disease progression by evaluating the course of myocardial tissue characteristics over time. Furthermore, the technology may be used for follow-up of patients after pacemaker implantation.

6.4.3 Improving pacemaker therapy success rates

Cardiac resynchronization therapy is an established HF therapy which has significantly improved the prognosis of HF patients. By optimizing patient selection and tailoring therapy delivery to individual patients, CRT success rates may be improved even further. This could make CRT a highly cost-effective therapy that can be used to treat dyssynchronous HF patients. At the same time, other pacing strategies are currently being explored, such as CSP [43,53]. The Digital Twin technology presented in this thesis can be modified or extended

to include other models of pacing. Therefore, the Digital Twin technology provides a useful tool to improve pacemaker therapy in HF patients. This could extend the life expectation of patients with HF and give them a better quality of life.

6.4.4 Reducing the unnecessary risk of complications

Currently, a significant number of HF patients who are implanted with a CRT device do not show to benefit from the therapy. Despite their negative therapy outcome, these patients have to go through an invasive procedure in which they are exposed to a substantial risk of developing perioperative complications [80,81]. Furthermore, post-operatively, various short-term and long-term complications may present, including life-threatening arrhythmias [80,82].

Although it can be decided to implant a CRT-D which also includes an implantable cardioverter defibrillator (ICD) to prevent sudden cardiac death (SCD) [43], it is usually preferred to implant a pacemaker only, also known as CRT-P. This is because CRT-D involves ICD-specific risks such as lead failure and inappropriate shocks. Furthermore, CRT-D is more expensive than CRT-P. By better identifying those patients who will likely benefit from CRT prior to implantation, unnecessary risks of complications during the CRT implantation procedure can be prevented. The Digital Twin technology developed in this thesis contributes to a better prediction of therapy potential prior to device implantation.

6.4.5 Enabling in silico clinical trials

The generation of virtual patient cohorts to perform *in silico* clinical trials provides an important addition to real-world clinical trials or animal experiments. These *in silico* clinical trials do not involve ethical considerations and can significantly reduce the costs of research studies. For example, simulation of device therapies in virtual patient cohorts can provide more insight into which patients are likely to benefit from a therapy or which potentially are harmed. The Digital Twin technology presented in this thesis adds important knowledge to inform the generation of virtual patient cohorts.

6.4.6 Contributing to the Digital Twin concept in cardiovascular research

Digital Twins currently are a hot research topic and the term ‘Digital Twin’ is on the rise, as shown by an increase from three publications listed on PubMed in the year 2018 to 362 in the year 2023. The Digital Twin provides an appealing concept for personalized medicine which facilitates to deliver the right therapy at the right moment to the right patient. In addition, it can help to improve collaboration and communication between researchers, clinicians, and patients. This thesis provides an important contribution to this Digital Twin concept in cardiovascular research and care.

REFERENCES

1. Nguyên UC, Verzaal NJ, van Nieuwenhoven FA, Vernooy K, Prinzen FW (2018). Pathobiology of cardiac dyssynchrony and resynchronization therapy. *Europace*. 20(12), 1898-1909.
2. Lumens J *et al.* (2015). Differentiating Electromechanical from Non-Electrical Substrates of Mechanical Discoordination to Identify Responders to Cardiac Resynchronization Therapy. *Circ. Cardiovasc. Imaging.* 8(9), 1-12.
3. Kemp CD, Conte JV (2012). The pathophysiology of heart failure. *Cardiovasc. Pathol.* 21(5), 365-371.
4. Richardson WJ, Clarke SA, Quinn TA, Holmes JW (2015). Physiological implications of myocardial scar structure. *Compr. Physiol.* 5(4), 1877-1909.
5. Lyseggen E, Skulstad H, Helle-Valle T, Vartdal T, Urheim S, Rabben SI, Opdahl A, Ihlen H, Smiseth OA (2005). Myocardial strain analysis in acute coronary occlusion: A tool to assess myocardial viability and reperfusion. *Circulation*. 112(25), 3901-3910.
6. Ypenburg C, Roes SD, Bleeker GB, Kaandorp TAM, de Roos A, Schalij MJ, van der Wall EE, Bax JJ (2007). Effect of Total Scar Burden on Contrast-Enhanced Magnetic Resonance Imaging on Response to Cardiac Resynchronization Therapy. *Am. J. Cardiol.* 99(5), 657-660.
7. Kloosterman M, Damman K, Van Veldhuisen DJ, Rienstra M, Maass AH (2017). The importance of myocardial contractile reserve in predicting response to cardiac resynchronization therapy. *Eur. J. Heart Fail.* 19(7), 862-869.
8. Leenders GE, Lumens J, Cramer MJ, De Boeck BWL, Doevendans PA, Delhaas T, Prinzen FW (2011). Septal Deformation Patterns Delineate Mechanical Dyssynchrony and Regional Differences in Contractility: Analysis of Patient Data Using a Computer Model. *Circ. Heart Fail.* 5(1), 87-96.
9. Chalil S, Stegemann B, Muhyaldeen SA, Khadjooi K, Foley PW, Smith REA, Leyva F (2007). Effect of posterolateral left ventricular scar on mortality and morbidity following cardiac resynchronization therapy. *PACE - Pacing Clin. Electrophysiol.* 30(10), 1201-1209.
10. Taylor RJ, Umar F, Panting JR, Stegemann B, Leyva F (2016). Left ventricular lead position, mechanical activation, and myocardial scar in relation to left ventricular reverse remodeling and clinical outcomes after cardiac resynchronization therapy: A feature-tracking and contrast-enhanced cardiovascular magnetic resonance study. *Heart Rhythm*. 13(2), 481-489.
11. Huntjens PR, Walmsley J, Ploux S, Bordachar P, Prinzen FW, Delhaas T, Lumens J (2014). Influence of left ventricular lead position relative to scar location on response to cardiac resynchronization therapy: A model study. *Europace*. 16, iv62-iv68.
12. Kim RJ, Wu E, Rafael A, Chen EL, Parker MA, Simonetti O, Klocke FJ, Bonow RO, Judd RM (2000). The Use of Contrast-Enhanced Magnetic Resonance Imaging to Identify Reversible Myocardial Dysfunction. *N. Engl. J. Med.* 343(20), 1445-1453.
13. Sunagawa K, Maughan WL, Sagawa K (1982). Effect of Regional Ischemia on the Left Ventricular End-Systolic Pressure-Volume Relationship of Isolated Canine Hearts. *Circ. Res.* 52(2), 170-179.
14. Kihlberg J, Haraldsson H, Sigfridsson A, Ebbers T, Engvall JE (2015). Clinical experience of strain imaging using DENSE for detecting infarcted cardiac segments. *J. Cardiovasc. Magn. Reson.* 17(1), 1-9.
15. Cimino S, Canali E, Petronilli V, Cicogna F, De Luca L, Francone M, Sardella G, Iacoboni C, Agati L (2013). Global and regional longitudinal strain assessed by two-dimensional speckle tracking echocardiography identifies early myocardial dysfunction and transmural extent of myocardial scar in patients with acute ST elevation

myocardial infarction and relatively. *Eur. Heart J. Cardiovasc. Imaging*. 14(8), 805-811.

16. Huttin O *et al.* (2016). Temporal deformation pattern in acute and late phases of ST-elevation myocardial infarction: incremental value of longitudinal post-systolic strain to assess myocardial viability. *Clin. Res. Cardiol.* 105(10), 815-826.
17. Maret E, Todt T, Brudin L, Nylander E, Swahn E, Ohlsson JL, Engvall JE (2009). Functional measurements based on feature tracking of cine magnetic resonance images identify left ventricular segments with myocardial scar. *Cardiovasc. Ultrasound*. 7(1), 1-14.
18. Holmes JW, Borg TK, Covell JW (2005). Structure and Mechanics of Healing Myocardial Infarcts. *Annu. Rev. Biomed. Eng.* 7(1), 223-253.
19. Owashi K, Taconné M, Courtial N, Simon A, Garreau M, Hernandez A, Donal E, Le Rolle V, Galli E (2022). Desynchronization Strain Patterns and Contractility in Left Bundle Branch Block through Computer Model Simulation. *J. Cardiovasc. Dev. Dis.* 9(2), 53.
20. Russell K, Eriksen M, Aaberge L, Wilhelmsen N, Skulstad H, Gjesdal O, Edvardsen T, Smiseth OA (2013). Assessment of wasted myocardial work: a novel method to quantify energy loss due to uncoordinated left ventricular contractions. *Am. J. Physiol. Circ. Physiol.* 305(7), H996-H1003.
21. Aalen JM *et al.* (2019). Mechanism of Abnormal Septal Motion in Left Bundle Branch Block: Role of Left Ventricular Wall Interactions and Myocardial Scar. *JACC Cardiovasc. Imaging.* 12(12), 2402-2413.
22. McDonagh TA *et al.* (2021). 2021 ESC Guidelines for the diagnosis and treatment of acute and chronic heart failure. *Eur. Heart J.* 42(36), 3599-3726.
23. Cleland JGF, Daubert JC, Erdmann E, Freemantle N, Gras D, Kappenberger L, Tavazzi L (2005). The Effect of Cardiac Resynchronization on Morbidity and Mortality in Heart Failure. *N. Engl. J. Med.* 352(15), 1539-1549.
24. Moss AJ *et al.* (2009). Cardiac-Resynchronization Therapy for the Prevention of Heart-Failure Events. *N. Engl. J. Med.* 361(14), 1329-1338.
25. Aalen JM *et al.* (2020). Imaging predictors of response to cardiac resynchronization therapy: Left ventricular work asymmetry by echocardiography and septal viability by cardiac magnetic resonance. *Eur. Heart J.* 41(39), 3813-3823.
26. Duchenne J *et al.* (2020). Acute redistribution of regional left ventricular work by cardiac resynchronization therapy determines long-term remodelling. *Eur. Heart J. Cardiovasc. Imaging.* 21(6), 619-628.
27. Gorcsan J, Anderson CP, Tayal B, Sugahara M, Walmsley J, Starling RC, Lumens J (2019). Systolic Stretch Characterizes the Electromechanical Substrate Responsive to Cardiac Resynchronization Therapy. *JACC Cardiovasc. Imaging*. 12(9), 1741-1752.
28. Wouters PC, Leenders GE, Cramer MJ, Meine M, Prinzen FW, Doevendans PA, De Boeck BWL (2021). Acute recoordination rather than functional hemodynamic improvement determines reverse remodelling by cardiac resynchronisation therapy. *Int. J. Cardiovasc. Imaging.* 37(6), 1903-1911.
29. Duckett SG *et al.* (2011). Invasive Acute Hemodynamic Response to Guide Left Ventricular Lead Implantation Predicts Chronic Remodeling in Patients Undergoing Cardiac Resynchronization Therapy. *J. Am. Coll. Cardiol.* 58(11).
30. Bogaard MD, Houthuizen P, Bracke FA, Doevendans PA, Prinzen FW, Meine M, van Gelder BM (2011). Baseline left ventricular dP/dt max rather than the acute improvement in dP/dt max predicts clinical outcome in patients with cardiac resynchronization therapy. *Eur. J. Heart Fail.* 13(10), 1126-1132.
31. de Roest GJ, Allaart CP, Kleijn SA, Delnoy PPHM, Wu L, Hendriks ML, Bronzwaer JGF, van Rossum AC, de Cock

CC (2013). Prediction of long-term outcome of cardiac resynchronization therapy by acute pressure-volume loop measurements. *Eur J. Heart Fail.* 15, 299-307.

32. Sohal M *et al.* (2021). A multicenter prospective randomized controlled trial of cardiac resynchronization therapy guided by invasive dP/dt. *Heart Rhythm O2*. 2(1), 19-27.
33. Okada J *et al.* (2017). Multi-scale, tailor-made heart simulation can predict the effect of cardiac resynchronization therapy. *J. Mol. Cell. Cardiol.* 108, 17-23.
34. Isotani A, Yoneda K, Iwamura T, Watanabe M, Okada J, Washio T, Sugiura S, Hisada T, Ando K (2020). Patient-specific heart simulation can identify non-responders to cardiac resynchronization therapy. *Heart Vessels*. 35(8), 1135-1147.
35. Arts T, Lumens J, Kroon W, Delhaas T (2012). Control of whole heart geometry by intramyocardial mechano-feedback: A model study. *PLoS Comput. Biol.* 8(2).
36. Vernooy K, Verbeek XAAM, Peschar M, Crijns HJGM, Arts T, Cornelussen RNM, Prinzen FW (2005). Left bundle branch block induces ventricular remodelling and functional septal hypoperfusion. *Eur. Heart J.* 26(1), 91-98.
37. Duchenne J *et al.* (2019). Left Ventricular Remodeling Results in Homogenization of Myocardial Work Distribution. *Circ. Arrhythmia Electrophysiol.* 12(5), 1-14.
38. Stankovic I *et al.* (2017). The association of volumetric response and long-term survival after cardiac resynchronization therapy. *Eur. Heart J. Cardiovasc. Imaging*. 18(10), 1109-1117.
39. Daubert C, Behar N, Martins RP, Mabo P, Leclercq C (2017). Avoiding non-responders to cardiac resynchronization therapy: A practical guide. *Eur. Heart J.* 38(19), 1463-1472.
40. Mullens W *et al.* (2020). Optimized implementation of cardiac resynchronization therapy: a call for action for referral and optimization of care: A joint position statement from the Heart Failure Association (HFA), European Heart Rhythm Association (EHRA), and European Association. *Eur. J. Heart Fail.* 22(12), 2349-2369.
41. Gold MR, Rickard J, Daubert JC, Zimmerman P, Linde C (2021). Redefining the Classifications of Response to Cardiac Resynchronization Therapy: Results From the REVERSE Study. *JACC Clin. Electrophysiol.* 7(7), 871-880.
42. Brignole M *et al.* (2013). 2013 ESC Guidelines on cardiac pacing and cardiac resynchronization therapy. *Eur. Heart J.* 34(29), 2281-2329.
43. Glikson M *et al.* (2021). 2021 ESC Guidelines on cardiac pacing and cardiac resynchronization therapy. *Eur. Heart J.* 42(35), 3427-3520.
44. Corral-Acero J *et al.* (2020). The 'Digital Twin' to enable the vision of precision cardiology. *Eur. Heart J.* 41(48), 4556-4564.
45. Peirlinck M *et al.* (2021). Precision medicine in human heart modeling: Perspectives, challenges, and opportunities. *Biomech. Model. Mechanobiol.* 20(3), 803-831.
46. Gray RA, Pathmanathan P (2018). Patient-specific cardiovascular computational modeling: Diversity of personalization and challenges. *J. Cardiovasc. Transl. Res.* 11(2), 80-88.
47. Cobb DB, Gold MR (2017). The Role of Atrioventricular and Interventricular Optimization for Cardiac Resynchronization Therapy. *Heart Fail. Clin.* 13(1), 209-223.
48. Gold MR *et al.* (2023). Effects of Atrioventricular Optimization on Left Ventricular Reverse Remodeling With Cardiac Resynchronization Therapy: Results of the SMART-CRT Trial. *Circ. Arrhythmia Electrophysiol.* 16(6), 313-324.
49. Marek JJ, Saba S, Onishi T, Ryo K, Schwartzman D, Adelstein EC, Gorcsan J (2014). Usefulness of echocardiographically guided left ventricular lead placement for cardiac resynchronization therapy in patients

with intermediate QRS width and non-left bundle branch block morphology. *Am. J. Cardiol.* 113(1), 107-116.

50. Nguyên UC *et al.* (2019). Integration of cardiac magnetic resonance imaging, electrocardiographic imaging, and coronary venous computed tomography angiography for guidance of left ventricular lead positioning. *Europace*. 21(4), 626-635.
51. Liu J, Adelstein E, Saba S (2013). Targeting left ventricular lead placement to improve cardiac resynchronization therapy outcomes. *Curr. Cardiol. Rep.* 15(8), 390.
52. Vijayaraman P *et al.* (2023). Cardiac Conduction System Pacing: A Comprehensive Update. *JACC Clin. Electrophysiol.* 9(11), 2358-2387.
53. Wijesuriya N, Elliott MK, Mehta V, De Vere F, Strocchi M, Behar JM, Niederer SA, Rinaldi CA (2023). Pacing interventions in non-responders to cardiac resynchronization therapy. *Front. Physiol.* 14, 1-10.
54. Willemen E *et al.* (2019). The Left and Right Ventricles Respond Differently to Variation of Pacing Delays in Cardiac Resynchronization Therapy: A Combined Experimental- Computational Approach. *Front. Physiol.* 10, 1-13.
55. Jones S *et al.* (2017). Cardiac resynchronization therapy: Mechanisms of action and scope for further improvement in cardiac function. *Europace*. 19(7), 1178-1186.
56. Meiburg R *et al.* (2023). Comparison of novel ventricular pacing strategies using an electro-mechanical simulation platform. *Europace*. 25(6), 1-11.
57. Crozier A *et al.* (2016). Analysis of lead placement optimization metrics in cardiac resynchronization therapy with computational modelling. *Europace*. 18, iv113-iv120.
58. Lee AWC *et al.* (2021). Non-invasive simulated electrical and measured mechanical indices predict response to cardiac resynchronization therapy. *Comput. Biol. Med.* 138, 104872.
59. Dokuchaev A, Chumarnaya T, Bazhutina A, Khamzin S, Lebedeva V, Lyubimtseva T, Zubarev S, Lebedev D, Solovyova O (2023). Combination of personalized computational modeling and machine learning for optimization of left ventricular pacing site in cardiac resynchronization therapy. *Front. Physiol.* 14, 1-21.
60. Strocchi M, Wijesuriya N, Mehta V, De Vere F, Rinaldi CA, Niederer SA (2024). Computational Modelling Enabling In Silico Trials for Cardiac Physiologic Pacing. *J. Cardiovasc. Transl. Res.* 17(3), 685-694.
61. Lee AWC *et al.* (2017). Biophysical Modeling to Determine the Optimization of Left Ventricular Pacing Site and AV/VV Delays in the Acute and Chronic Phase of Cardiac Resynchronization Therapy. *J. Cardiovasc. Electrophysiol.* 28(2), 208-215.
62. Panthee N, Okada J, Washio T, Mochizuki Y, Suzuki R, Koyama H, Ono M, Hisada T, Sugiura S (2016). Tailor-made heart simulation predicts the effect of cardiac resynchronization therapy in a canine model of heart failure. *Med. Image Anal.* 31, 46-62.
63. Holmes JW, Lumens J (2018). Clinical Applications of Patient-Specific Models: The Case for a Simple Approach. *J. Cardiovasc. Transl. Res.* 11(2), 71-79.
64. Aalen J *et al.* (2019). Afterload Hypersensitivity in Patients With Left Bundle Branch Block. *JACC Cardiovasc. Imaging*. 12(6), 967-977.
65. van Loon T, Knackstedt C, Cornelussen R, Reesink KD, Brunner La Rocca HP, Delhaas T, van Empel V, Lumens J (2020). Increased myocardial stiffness more than impaired relaxation function limits cardiac performance during exercise in heart failure with preserved ejection fraction: A virtual patient study. *Eur. Heart J. Digit. Health*, 1(1), 40-50.
66. Voigt JU *et al.* (2015). Definitions for a common standard for 2D speckle tracking echocardiography: consensus

document of the EACVI/ASE/Industry Task Force to standardize deformation imaging. *Eur. Heart J. Cardiovasc. Imaging.* 16(1), 1-11.

67. Galli E, Baritussio A, Sitges M, Donnellan E, Jaber WA, Gimelli A (2023). Multi-modality imaging to guide the implantation of cardiac electronic devices in heart failure: is the sum greater than the individual components? *Eur. Heart J. Cardiovasc. Imaging*, 24(2), 163-176.
68. Roy CJ, Oberkampf WL (2011). A comprehensive framework for verification, validation, and uncertainty quantification in scientific computing. *Comput. Methods Appl. Mech. Eng.* 200(25-28), 2131-2144.
69. Eck VG, Donders WP, Sturdy J, Feinberg J, Delhaas T, Hellevik LR, Huberts W (2016). A guide to uncertainty quantification and sensitivity analysis for cardiovascular applications. *Int. J. Numer. Method. Biomed. Eng.* 32(8), e02755.
70. van Stipdonk AMW *et al.* (2018). QRS Area Is a Strong Determinant of Outcome in Cardiac Resynchronization. *Circ. Arrhythmia Electrophysiol.* 11(12), e006497.
71. Walmsley J, Arts T, Derval N, Bordachar P, Cochet H, Ploux S, Prinzen FW, Delhaas T, Lumens J (2015). Fast Simulation of Mechanical Heterogeneity in the Electrically Asynchronous Heart Using the MultiPatch Module. *PLoS Comput. Biol.* 11(7), 1-23.
72. Strocchi M *et al.* (2023). Effect of scar and His – Purkinje and myocardium conduction on response to conduction system pacing. *J. Cardiovasc. Electrophysiol.* 34, 984-993.
73. Deng D, Arevalo HJ, Prakosa A, Callans DJ, Trayanova NA (2016). A feasibility study of arrhythmia risk prediction in patients with myocardial infarction and preserved ejection fraction. *Europace*. 18, iv60-iv66.
74. Arevalo HJ, Vadakkumpadan F, Guallar E, Jebb A, Malamas P, Wu KC, Trayanova NA (2016). Arrhythmia risk stratification of patients after myocardial infarction using personalized heart models. *Nat. Commun.* 7, 1-8.
75. Oomen PJA, Phung TKN, Weinberg SH, Bilchick KC, Holmes JW (2022). A rapid electromechanical model to predict reverse remodeling following cardiac resynchronization therapy. *Biomech. Model. Mechanobiol.* 21(1), 231-247.
76. van Osta N *et al.* (2021). Uncertainty Quantification of Regional Cardiac Tissue Properties in Arrhythmogenic Cardiomyopathy Using Adaptive Multiple Importance Sampling. *Front. Physiol.* 12, 1-15.
77. Conrad N *et al.* (2018). Temporal trends and patterns in heart failure incidence: a population-based study of 4 million individuals. *Lancet*. 391(10120), 572-580.
78. van Riet EES, Hoes AW, Wagenaar KP, Limburg A, Landman MAJ, Rutten FH (2016). Epidemiology of heart failure: the prevalence of heart failure and ventricular dysfunction in older adults over time. A systematic review. *Eur. J. Heart Fail.* 18, 242-252.
79. Abdin A *et al.* (2021). Time is prognosis' in heart failure: time-to-treatment initiation as a modifiable risk factor. *ESC Heart Fail.* 8(6), 4444-4453.
80. Udo EO, Zuithoff NPA, van Hemel NM, de Cock CC, Hendriks T, Doevendans PA, Moons KGM (2012). Incidence and predictors of short- and long-term complications in pacemaker therapy: The FOLLOWPACE study. *Heart Rhythm*. 9(5), 728-735.
81. Kirkfeldt RE, Johansen JB, Nohr EA, Moller M, Arnsbo P, Nielsen JC (2011). Risk factors for lead complications in cardiac pacing: A population-based cohort study of 28,860 Danish patients. *Heart Rhythm*. 8(10), 1622-1628.
82. Koneru JN, Jones PW, Hammill EF, Wold N, Ellenbogen KA (2018). Risk factors and temporal trends of complications associated with transvenous implantable cardiac defibrillator leads. *J. Am. Heart Assoc.* 7(10), e007691.

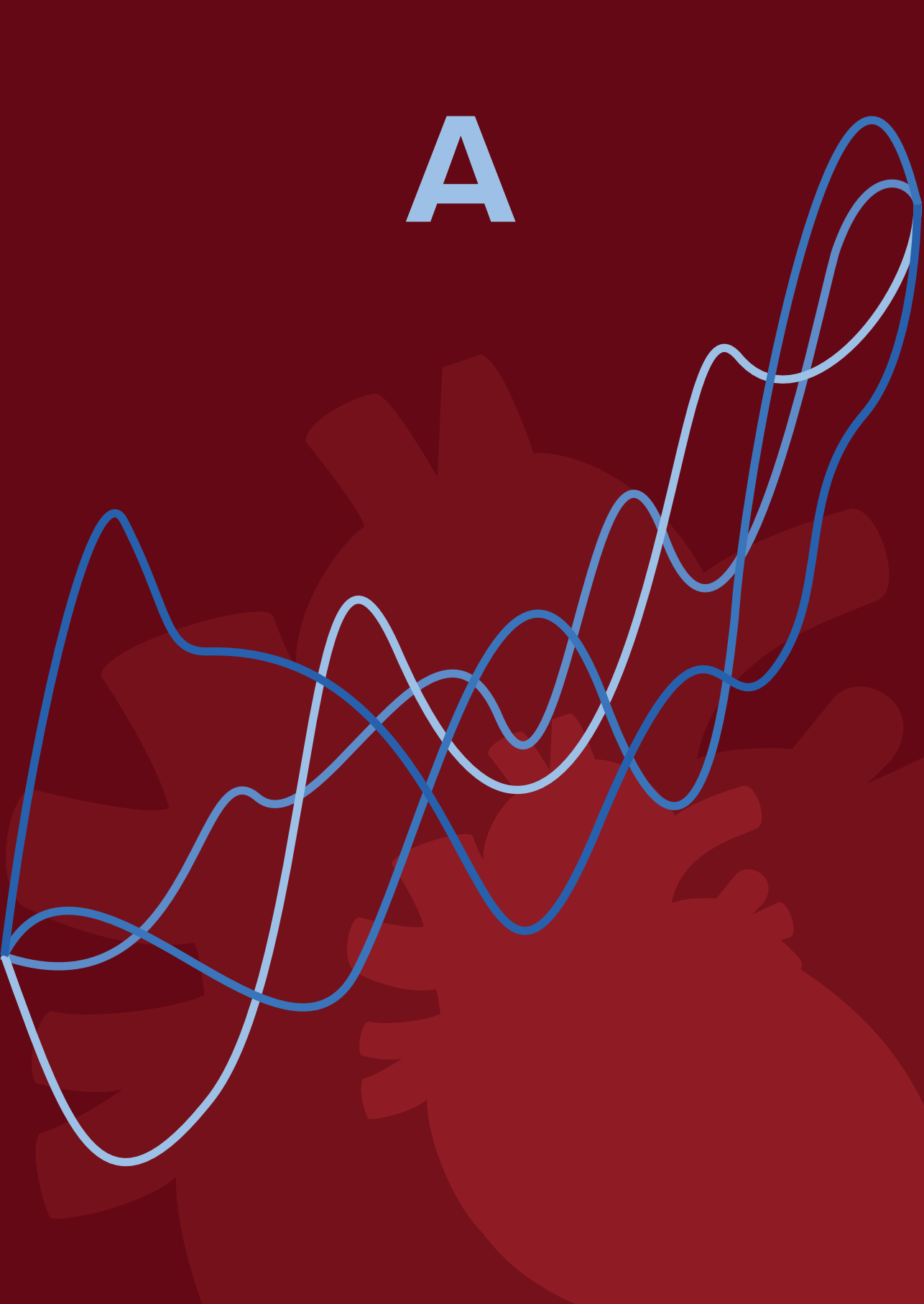
A

Appendices

SUMMARY

The pumping function of the heart relies on a well-coordinated contraction which is normally initiated by a rather synchronous activation of the cardiac ventricles. In dyssynchronous heart failure (HF), this coordinated contraction is lost due to an electrical conduction disturbance, often left bundle branch block (LBBB), and replaced with an inefficient pattern of ventricular contraction and relaxation. The resulting reduction of left ventricular ejection fraction (LVEF) is further aggravated not only by adverse structural remodeling processes, but also by active and passive tissue abnormalities induced by e.g. myocardial infarction (MI). Patients with dyssynchronous HF often have a reduced quality of life and five-year mortality rates remain as high as 67%.

Cardiac resynchronization therapy (CRT) is an established device therapy for dyssynchronous HF which has shown to acutely improve pump function and reduce HF symptoms and mortality. Current guidelines recommend CRT in patients with an LVEF ≤35% and QRS duration ≥150 ms with LBBB QRS morphology. Despite the important success of CRT as an HF treatment, significant uncertainty remains about which patients will benefit from CRT implantation. Up to 45% of implanted patients are found to be non-responders, while a large number of eligible patients do not currently receive a CRT device. Strategies to further improve patient selection and delivery of CRT are therefore essential.

In this thesis, we have used the CircAdapt model of the human heart and circulation to obtain more insight into the electro-mechanical myocardial disease substrates of dyssynchronous HF patients. Furthermore, we have used the model to investigate whether a personalized characterization of the patient's disease can help to predict response to CRT. These aims were achieved by developing an algorithm which automatically personalized the model to a patient's non-invasive LV cavity volume and regional deformation measurements, thereby generating the patient's Digital Twin. We then simulated biventricular pacing in the Digital Twin to quantify virtual therapy response as a potential predictor of the real patient's response to CRT, quantified by the extent of LV reverse remodeling.

In **Chapter 2**, we used computer simulations to improve our mechanistic understanding of myocardial strain patterns which are typically observed in CRT candidates. We showed that the CircAdapt model is able to accurately simulate these strain patterns, and also that different patterns could be explained by different types and degrees of LV structural remodeling. The selection of manually fitted model parameters was based on clinical observations which suggested that the degree of LBBB-induced remodeling influences the myocardial strain patterns of HF patients. Our results in **Chapter 2** corroborated this hypothesis, and therefore importantly extended the findings of previous studies which showed that myocardial contractility and stiffness also determine the morphology of strain patterns. Moreover, these studies already showed that these different strain patterns are associated with a different response to CRT. Therefore, we concluded that a personalized modeling approach based on integration of strain measurements into the CircAdapt model

could provide more insight into the contractility and stiffness of the myocardium, but also into the degree of LV structural remodeling.

Since a large number of dyssynchronous HF patients are suffering from ischemic heart disease which is known to impact CRT response, we implemented a two-compartment modeling approach in **Chapter 3** to simulate global and regional tissue mechanics during acute myocardial ischemia and infarction. This two-compartment model simulated the myocardium using an active and a passive compartment, and was based on experimental observations of the effects of regional ischemia on end-systolic pressure-volume relationships in excised canine ventricles. After we validated this modeling approach using previously published myocardial deformation measurements in dogs with coronary occlusion, we applied this modeling approach to simulate the strain patterns of six patients with MI but without a ventricular conduction delay (i.e. with narrow QRS complexes). Hereto, we developed an algorithm which automatically estimated the parameters of the two-compartment model based on non-invasive LV cavity and regional strain measurements. Automatic estimation of the regional severity of contractile dysfunction, quantified by the non-contractile volume fraction ($NCVF$), showed that increased $NCVF$ values were found in myocardial segments with an increased percentage of late gadolinium enhancement (LGE), representing scar.

The set of model parameters which was estimated in **Chapter 3** was chosen based on prior knowledge about the pathophysiology of the patient population. However, in **Chapter 4** we performed a comprehensive sensitivity and identifiability analysis to define an objective parameter subset for estimation in dyssynchronous HF patients. The goal of this analysis was to find a parameter subset which could be reproducibly estimated from non-invasive echocardiographic LV cavity volume and regional strain measurements of patients with dyssynchronous HF, as well as of patients with a narrow-QRS complex and MI. Due to a poor identifiability of the parameters of the two-compartment model, we switched back to a one-compartment implementation of myocardial contractile dysfunction. In this latter model, we obtained a parameter subset which consisted of cardiac output, global and regional ventricular myocardial activation, and a limited set of LV myocardial constitutive properties. This parameter subset was used not only to generate Digital Twins of the same six patients as studied in **Chapter 3**, but also to create Digital Twins of four HF patients with non-ischemic LBBB and three HF patients with ischemic LBBB. We concluded that the LV myocardial work (MW) distribution of these Digital Twins was representative for the patient's underlying disease substrates of LBBB and MI.

In **Chapter 5**, we then evaluated whether this personalized modeling approach could be used to predict the effect of CRT. To this end, we generated Digital Twins of 45 dyssynchronous HF patients using measurements obtained before CRT device implantation. Since previous studies have shown that the baseline difference in MW performed by the septum and the lateral wall is a strong predictor of CRT response, we quantified this index for each Digital Twin. We subsequently applied a patient-specific virtual pacing intervention

to calculate the pacing-induced reduction of this workload imbalance. Our results showed that the Digital Twin's baseline septal-to-lateral workload imbalance as well as the reduction thereof by virtual pacing were significantly associated with the patient's LV reverse remodeling at six months follow-up after CRT.

We conclude that we have obtained more insight into the underlying disease substrates of dyssynchronous HF patients based on the LV MW distribution of their Digital Twins, albeit that additional measurements are needed to allow a better differentiation between active and passive myocardial tissue properties. Nonetheless, the Digital Twins which were generated in this thesis show the potential of this personalized medicine approach as an additional strategy to select patients for CRT on top of ECG characteristics. In our concluding **Chapter 6**, we have discussed the insights that were obtained in this thesis and we have elaborated on the potential of the Digital Twin for future application in the field of pacemaker therapy. With further refinement of the technology, supported by the addition of measurement data and the reconsideration of model definition and context of use, we think that the Digital Twin technology can play a promising role to support the clinical delivery of pacemaker therapies.

SAMENVATTING

De pompfunctie van het hart wordt geleverd door een sterk gecoördineerde samentrekking van de hartspier. Normaal gesproken wordt deze samentrekking geïnitialiseerd door een vrijwel gelijktijdige activatie van de linker- en rechterhartkamers, maar in het geval van dyssynchroon hartfalen (HF) is de gecoördineerde samentrekking verloren gegaan door een verstoring van de elektrische geleiding, vaak een linker-bundeltakblok (LBTB). Patiënten met dyssynchroon HF hebben een inefficiënt patroon van samentrekken en ontspannen van de hartkamerspier, hetgeen resulteert in een slechtere pompfunctie waarbij er een lagere fractie van het bloedvolume in de linkerkamer wordt uitgepompt. Deze vermindering van de ejectiefractie van de linkerkamer (LVEF) wordt niet alleen verder verergerd doordat de hartspier zich tevergeefs probeert aan te passen aan de veranderde belasting, maar ook door actieve en passieve afwijkingen van het spierweefsel, bijvoorbeeld als gevolg van een myocardinfarct (MI). Patiënten met dyssynchroon HF hebben vaak een verminderde kwaliteit van leven en de sterfte na vijf jaar loopt op tot wel 67%.

Cardiale resynchronisatietherapie (CRT) is een erkende pacemakertherapie voor dyssynchroon HF. Onderzoek heeft aangetoond dat deze therapie tot een acute verbetering van de pompfunctie leidt en dat deze zowel de symptomen van HF vermindert als de overlevingskans doet toenemen. De huidige richtlijnen bevelen CRT aan bij patiënten met een LVEF ≤35%, een ventriculaire activatietijd (QRS-duur) ≥150 ms en een LBTB-morfologie van het QRS-complex. Ondanks de vele successen van CRT als behandeling voor HF, is het nog steeds erg onduidelijk welke patiënten baat zullen hebben bij deze pacemakertherapie. Niet alleen kan het gerapporteerde percentage van patiënten met een negatieve behandelingsuitkomst wel oplopen tot zo n 45%, maar ook wordt CRT momenteel onthouden bij een groot aantal geschikte patiënten. Het is daarom van essentieel belang om nieuwe strategieën te ontwikkelen die leiden tot een betere patiëntselectie voor toediening van CRT.

In deze thesis hebben we het CircAdapt model van het menselijk hart en de menselijke bloedsomloop gebruikt om meer inzicht te verkrijgen in de onderliggende weefselabnormaliteiten van patiënten met dyssynchroon HF. Ook hebben we dit model gebruikt om te onderzoeken of een gepersonaliseerde karakterisering van de hartspier van de patiënt kan helpen bij het voorspellen van het effect van CRT. Deze doelstellingen zijn bereikt door een algoritme te ontwikkelen waarmee het model automatisch gepersonaliseerd wordt aan de hand van niet-invasieve metingen van het holtevolume en de lokale bewegingspatronen van de linkerkamerspier. Het gepersonaliseerde CircAdapt model kan vervolgens gezien worden als een digitale kopie, ook wel digitale tweeling genoemd, van het hart van de individuele patiënt. In deze digitale tweeling hebben we CRT gesimuleerd om de door het model voorspelde uitkomst van de therapie te bepalen en deze te vergelijken met de werkelijke uitkomst van CRT in de patiënt. Laatstgenoemde werd gekwantificeerd door bepaling van de mate van volumeverandering van de linkerkamer na zes maanden.

In **Hoofdstuk 2** hebben we computersimulaties gebruikt om ons inzicht in de bewegingspatronen van de hartspier van CRT-kandidaten te vergroten. We hebben aangetoond dat het CircAdapt model in staat is om deze patronen met grote nauwkeurigheid te simuleren. Bovendien hebben we laten zien dat verschillende bewegingspatronen verklaard kunnen worden door verschillende typen en maten van structurele aanpassing van de hartspier. De keuze van afgeschatte, handmatig gekwantificeerde modelparameters was gebaseerd op klinische waarnemingen die suggereerden dat de mate van structurele aanpassing van de hartspier als gevolg van LBTB in patiënten met HF van invloed is op de lokale bewegingspatronen van de hartspier. Onze resultaten in **Hoofdstuk 2** waren in lijn met deze hypothese. Daarmee vormden ze een belangrijke aanvulling op eerder gedane studies, die lieten zien dat de contractiekracht en stijfheid van de hartspier ook invloed hebben op deze bewegingspatronen. Uit deze eerdere studies was bovendien al gebleken dat deze verschillende bewegingspatronen verband houden met een verschillend effect van CRT. Daarom concludeerden we dat een gepersonaliseerde aanpak met het CircAdapt model op basis van bewegingspatronen meer inzicht zou kunnen bieden in de contractiekracht en stijfheid van de hartspier, en ook in de mate van structurele aanpassing van deze hartspier.

Omdat veel patiënten met dyssynchroon HF ook problemen hebben met de doorbloeding van de hartspier, ook wel ischemische hartziekte genoemd, en bekend is dat deze ziekte invloed heeft op het effect van CRT, hebben we in **Hoofdstuk 3** een model gebruikt teneinde het globale en regionale weefselgedrag tijdens acute ischemie en infarct te reproduceren. Dit model simuleerde het spierweefsel met behulp van twee compartimenten, een actief en een passief compartiment, en was gebaseerd op experimentele waarnemingen die de effecten van regionale ischemie op de eindsystolische druk-volumerelatie van geïsoleerde hartkamers van honden lieten zien. Nadat we deze modelaanpak hadden gevalideerd met behulp van eerder gepubliceerde metingen van hartspierbewegingen in honden met afgesloten kransslagaders, hebben we deze aanpak toegepast om de bewegingspatronen van zes patiënten met een MI maar zonder geleidingsprobleem (met normale QRS-duur) te simuleren. Hiertoe ontwikkelden we een algoritme dat de parameters van het tweecompartimentenmodel automatische afschatte op basis van niet-invasieve metingen van holtevolume en regionale beweging van de linkerkamerspier. De automatische afschatting van de lokale ernst van krachtvermindering, gekwantificeerd door de niet-contractiele volumefractie ($NCVF$), liet zien dat een verhoogde $NCVF$ werd bepaald in segmenten die een toegenomen late gadolinium aankleuring (LGE) vertoonden, wat duidt op de aanwezigheid van een infarct.

De modelparameters die werden geschat in **Hoofdstuk 3** waren gekozen op basis van voorkennis met betrekking tot de ziekte van de patiëntenpopulatie. In **Hoofdstuk 4** hebben we een uitgebreide gevoeligheids- en identificeerbaarheidsanalyse uitgevoerd om een objectieve subset van modelparameters te bepalen voor afschatting bij patiënten met dyssynchroon HF. Het doel van deze analyse was om een subset van parameters te

vinden die reproduceerbaar kon worden afgeschat uit niet-invasieve echocardiografische metingen van het holtevolume en de regionale beweging van de linkerkamerspier, zowel bij patiënten met dyssynchroon HF als bij patiënten met normale QRS-duur en MI. Vanwege een slechte identificeerbaarheid van de bij het tweecompartimentenmodel behorende parameters, stapten we over op een ééncompartimentenmodel van contractiele krachtvermindering. In laatstgenoemde model verkregen we een subset van relevante en identificeerbare parameters bestaande uit hartminuutvolume, globale en regionale activatie van de hartkamers, en een beperkte set van weefseleigenschappen van de linkerkamerspier. Deze subset van parameters hebben we niet alleen gebruikt om digitale tweelingen te genereren van dezelfde zes patiënten die werden opgenomen in **Hoofdstuk 3**, maar ook om digitale tweelingen te maken van vier HF patiënten met niet-ischemische LBTB en drie HF patiënten met ischemische LBTB. We concludeerden dat de ruimtelijke verdeling van arbeid in de linkerkamerspier van deze digitale tweelingen kenmerkend was voor de onderliggende ziektesubstraten van LBTB en MI van de patiënt.

In **Hoofdstuk 5** hebben we getest of deze gepersonaliseerde modelaanpak gebruikt kan worden om het effect van CRT te voorspellen. Hiertoe hebben we digitale tweelingen gegenereerd van 45 patiënten met dyssynchroon HF, gebruikmakend van metingen die werden verkregen vóór de implantatie van de CRT-pacemaker. Omdat eerder gerapporteerd was dat de arbeidsverdeling tussen het septum en de vrije wand van de linkerkamer een goede voorspeller is voor het effect van CRT, hebben we deze index in iedere digitale tweeling gekwantificeerd. Daarna hebben we een patiëntspecifieke pacemakerinterventie gesimuleerd en de resulterende vermindering van deze arbeidsongelijkheid gekwantificeerd. Onze resultaten lieten zien dat zowel de aanvankelijke ongelijkheid in arbeid tussen het septum en de vrije wand van de linkerkamer als de vermindering van deze arbeidsongelijkheid door virtueel pacen significant geassocieerd konden worden met de klinisch opgetreden mate van volumeverandering van de linkerkamer na zes maanden van CRT.

We concluderen dat we op basis van de arbeidsverdeling in de linkerkamer van digitale tweelingen van patiënten met dyssynchroon HF meer inzicht hebben verkregen in de onderliggende ziektesubstraten van deze patiënten, hoewel aanvullende metingen nodig zijn om een beter onderscheid te kunnen maken tussen actieve en passieve eigenschappen van het hartspierweefsel. Desondanks tonen de digitale tweelingen in deze thesis de potentie van deze gepersonaliseerde benadering. Ze kunnen naast de karakteristieken van het ECG worden gebruikt als een aanvullende strategie om patiënten te selecteren voor CRT. In ons afsluitende **Hoofdstuk 6** hebben we de inzichten die we hebben opgedaan in deze thesis besproken en hebben we de potentie van de digitale tweeling voor verdere toepassing op het gebied van pacemakertherapie uitgebreid belicht. Wanneer de technologie verder verfijnd wordt, ondersteund door het toevoegen van meer data en het heroverwegen van de definitie en het gebruik van het model, zijn wij van mening dat de digitale tweelingtechnologie een veelbelovende rol kan spelen bij het ondersteunen van de klinische implementatie van pacemakertherapieën.

ACKNOWLEDGEMENTS

Finally, my PhD trajectory has come to an end. What an adventure it has been. A memorable journey with, most of all, many great experiences. I feel like I have been at Maastricht University for a very long time. And actually, it has been a long time. I remember that I came to Maastricht University as early as in 2013, at that time still as a Bachelor student at TU Eindhoven. Back then, I did not know yet what I wanted to do with my life (other than doing sports and playing GTA 5). However, I did notice that I was fascinated by the clinical procedures which I witnessed here. Spending time in the clinic was an inspiration for me as an engineer. It was also during that time that I met **Tammo**, **Joost**, and **Koen R.**, who taught me about the physiology of the heart and blood vessels. I enjoyed discussing with them a lot. They were passionate about research and they knew exactly how to challenge me. And on top of that, they were just simply very nice guys. It was thanks to their enthusiasm and critical questions (especially from **Tammo**, I will never forget Boron and Boulpaep ;)) that I discovered my own passion for research. While I could not foresee at the time that I would start my PhD in Maastricht four years later, I think that the seed had been planted. For sure, it was also thanks to **Claire**, since she was always there to help me and she made me feel very much at home at the Biomedical Engineering (BME) department.

And now, more than ten years later and after many hours of working to complete my thesis, I can say that I am happy to have performed my PhD research at BME. I will never forget this period of my life. I have enjoyed the many scientific discussions I have had. The countless lab meetings. Even the journal clubs (okay, let us be honest, not too often). The conferences I have gone to. The translational meetings I have attended. The courses I have followed. The presentations I have given. The teaching sessions I have done. All of these were fun. And they have made me grow as a researcher and as a person. In addition to all of these scientific ingredients, I have enjoyed just as much all other aspects of my PhD at BME. I have eaten more pieces of vlaai than I could ever have imagined. I have attended many exciting day-outs and departmental dinners. I have improved my football skills during lunch and working time (as of today, I am still surprised by how little got broken in the lab). I have trained my table tennis skills. And I have cycled many, many kilometers through the beautiful surroundings of Maastricht. By now, I have heard people speak Limburg dialect so often that I even came to understand it (speaking is a different thing, I will not try that). It is fair to say that Maastricht is in my heart. And even though I still feel like a Brabander, I have experienced what people like about Maastricht so much. It is a great place to live and to be. I am grateful to be able to acknowledge that.

However, without a doubt, my experiences would not have been the same without the many people who were involved. It is thanks to these people, you, that my PhD trajectory has been a great time and that I can look back on it with a smile. You gave me so many beautiful memories. Yes, you were the people who supported me, inspired me, motivated me, laughed and cried with me. You have truly meant a great deal to me. Therefore, in this

section, I would like to explicitly thank you for being a part of my journey and for making this thesis more than a product of my own.

Before I continue to do so, however, there is something else which I have to address. I cannot look at my thesis without being reminded of something that is not so colorful. While having had doubts to write about it here, I know that I have to. I want to. There is no way that I can write about my PhD trajectory and leave out a significant part of it. And actually, I even want to express my gratitude to it. Back in 2017, when I started, I had thought that I would be defending by the end of 2021, maybe 2022. That was my plan. And I wanted to enjoy doing research like I had done before. However, it turned out that during these years, often, I could not. I was unable to. For many days, I was struggling to even make it to the office. Every day again. Again, and again. For many hours, I felt miserable. Anxious. Confused. Desperate. I did not recognize myself anymore. I was unable to focus on research. My brain just kept going. I was spending time in places where it was dark. Extremely dark. I hated myself. I hated myself for not being able to pull myself together. For getting dragged into the past every time. For not daring to speak up about the thoughts that bothered me. For delivering bad quality work. For fucking up the opportunities that were given to me. For not showing up when I had to. For feeling anxious all the time. For not being a man, whatever that meant. The voices in my head were loud. I felt ashamed. Much ashamed. And even though I knew that I still had love for research, I could not find it anymore. The thoughts and feelings were just too strong. I did not know how to get out of it. I tried to do as much as I could. At any moment in time. But often, I felt like I was just surviving. I would typically walk into the office in the morning, hopeful of getting some work done, and then soon find out that my brain and heart had their own agenda. I felt powerless. I was completely exhausted by the end of the day and I did not get a centimeter closer to my destination. It felt horrible. What was I supposed to do? After a while, I started to consider giving up on my PhD. I simply could not stand the pain of failing all the time anymore. Of course, I did not want to stop. Absolutely not. But I was feeling like I was letting everyone down. The people I worked with, my friends, my family, my girlfriend. I blamed myself for that too. And then, I began to question whether life was still worth living. It got that bad. At times, I really found myself not giving a shit about anything anymore. It scared me. Of course, I did not want to give up. Even inside all of that darkness, I knew that somewhere, sometime, there had to be a way that I could begin to enjoy life again. But at the same time, I came to the conclusion that there was a limit to what I could take. And I was close to that limit.

Luckily, I can say today that I am still here and that I am feeling much better. I am so happy to be able to say that. Is it all over now? No. I am still in the process, for sure. But I see a lot of progress, and that gives me so much energy and motivation. I feel calmer, happier, clearer, more interested, and especially, more myself. In the end, that is the key for me. I am truly learning to be okay with myself. To accept the good and the bad. The mistakes which I have made. The mistakes which I still am going to make. The coping mechanisms which I have developed in the past. The way of dealing with these coping mechanisms in the

future. There is another voice inside of me. A voice which tells me that I am good enough. And that voice is getting louder. I do not feel ashamed anymore. No, I am open, and you can ask me whatever you want. If there is anything that this period has taught me, it is that not opening up can be a big danger. Of course, there can be good reasons to do so. But, please, from my perspective, be aware of the consequences that it may have. If you ask me, we need each other. I needed other people. I can come up here with some story that I dealt with this on my own, but that is not true. I have had many hours of therapy. I have read and listened to other people's stories. I have talked for many hours with friends and family. I had a girlfriend who was taking care of me. I have been inspired by you, the people around me. I had to feel and experience that I was not in this alone. To realize that in fact, nothing was really wrong with me. It was too easy to get lost in my head sometimes. I am so, so grateful to those of you who have taken the time to listen to me. And, moreover, to those of you who have been so courageous to open up to me. As a great gift of that, our relationships have deepened. I am very, very grateful for that. Please know that I will be there for you too, whenever I can. You know that I will be, because I know how much it matters. I love you.

To conclude, I would like to stress that even though this period has obviously been difficult and painful, I am grateful for what it has brought me. Things have gone the way they have. I feel like a different person now. I am accepting of what is. I did what I could. And I am still proud of the thesis that I have written. I stand behind the scientific content that it includes, and I will defend it to the best of my abilities. After all, hidden inside all of that pain, were lessons. Important lessons. On the surface, they were difficult to see. I mean, how can you see them when clouds are blocking your view? But truly, they were there all the time. I just did not know where to look. And as with many things in life (also referring to the quote in the beginning of my thesis), I think that understanding patterns is key. Our own thought patterns, in this case. Just like strain patterns in heart failure patients, they contain a lot of information. Yes, they are true patterns with potential. Let us end with a smile and move on.

And now that this is off my chest, I would like to continue to thank all of those people who were part of my journey. First of all, I would like to express my gratitude to my promotion team. **Joost**, ik kan je niet genoeg bedanken voor jouw begeleiding tijdens mijn PhD. Ik denk dat ik me geen betere mentor had kunnen wensen. Ten eerste heb ik simpelweg met heel veel plezier met jou samengewerkt. We hebben gelachen, we hebben heel veel leuke gesprekken gehad, en we hebben heel veel mooie wetenschappelijke discussies gevoerd. Naast de begeleiding die jij mij hebt geboden als onderzoeker, ben je voor mij onmisbaar geweest als persoon. Je bent altijd in mij blijven geloven en je hebt me steeds de kans gegeven om mijn weg te vervolgen. Bovendien was je altijd bereid om met mij te discussiëren over onderzoek, of eigenlijk over wat dan ook. Je wist me te blijven motiveren door telkens de positieve kanten van mijn werk te laten inzien. Jouw enthousiasme werkt voor mij aanstekelijk en je bent een geweldige sparringpartner die altijd ideeën en/of een mening heeft over hoe iets aangepakt kan worden. Bovendien heb je de resultaten van ons laatste artikel in het nationale nieuws gekregen, dat was nog eens een hele mooie

waardering van ons werk en ik ben je dankbaar dat je deze stap hebt genomen. Ik kan met recht zeggen dat je een inspiratie voor me bent en dat deze thesis er zonder jou niet was gekomen. Datzelfde geldt voor jou, **Tammo**. Dankjewel dat je mij de kans hebt gegeven om deze thesis tot een goed einde te brengen en dat je me hebt geholpen om mezelf te ontwikkelen als onderzoeker en als persoon. Jij bent nooit te beroerd om je mening te geven en ik waardeer die mening enorm. Ook jij bent voor mij een voorbeeld als mentor, en bovendien heb je een unieke kijk op het onderzoek die mij vaak heeft geholpen om mijn werk te verbeteren. **Nick**, ook jou wil ik hier een speciale vermelding geven. Jij hebt gedurende mijn hele PhD een grote rol gespeeld in het tot een goed einde brengen van deze thesis. In het eerste gedeelte van mijn PhD was dit vooral met inhoudelijke discussies, die ik met veel plezier heb beleefd. In het tweede gedeelte was jij ook betrokken bij de begeleiding van mijn onderzoek. Hierbij wist jij mij te motiveren met jouw enthousiasme en was je een goede sparringpartner wat betreft het onderzoek of zaken daarbuiten. Daarbij heb je ook nog eens taken van mij overgenomen op het moment dat ik deze zelf even niet kon uitvoeren, en daar ben ik je heel erg dankbaar voor. Wat ook niet onvermeld mag blijven is dat jij heel veel kennis hebt van de computationale aspecten van ons onderzoek en van die kennis maakte ik maar al te graag gebruik op de momenten dat ik die nodig had. Heel erg bedankt hiervoor!

Shaiv, switching back to English, you have become more than a good friend of mine. I have not often experienced a connection in the way that I did when I started speaking with you about, basically, anything. I think we are similar in many ways. And having such different backgrounds at the same time, I think that is something which is amazing to discover. I have enjoyed our extensive conversations about scientific and non-scientific topics. Wherever our paths will lead, I am sure that we will stay in touch.

Prof. dr. ir. R.L.M. Peeters, Prof. dr. L. Geris, Dr. J.G.L.M. Luermans, Prof. dr. J.U. Voigt, Prof dr. P.G.A. Volders, thank you for taking the time to critically assess my thesis and for approving it for public defense. Also, thank you, **Dr. V. van Empel** and **Dr. M. Cluitmans**, for your critical assessment of my thesis and for completing the committee during my defense.

And now back to the BME department. **Andrija**, we have also grown closer over the years. I am always having a good time with you, whether it is when having a coffee, playing chess, or going on a trip to Prague. And, together with **Shaiv**, we have had many fun pizza nights with interesting conversations which have been a nice distraction from the work on the thesis. Thanks a lot for that! **Tim**, fitboy, dankjewel voor alle leuke momenten samen. Ik heb jou mogen meemaken vanaf masterstudent tot na het afronden van je PhD en ik vond het super om daarbij te zijn. Lekker ook om even Brabants te kunnen praten tussen al dat Limburgs door. Ook hebben we samen de Papendal cursus gedaan, was erg leuk om dat samen te doen (en ik zal jouw TED talk daar niet gauw vergeten haha). Ik heb ook genoten van de discussies met jou en onze andere fitboy **Nick**, over fitten (hoe kan het ook anders), politiek, en van alles en nog wat. Samen hebben we heel veel lol gehad op de kamer, van BME radio tot Tirolermuziek, Franzl Lang, Lammert, Costa Cordalis en noem

de hele mikmak allemaal maar op. Dat ga ik zeker niet vergeten. Mocht er ooit een kans komen om alsnog naar het Tirolerfeest in Oostenrijk te gaan, laat het me vooral weten. **Alessandro**, I have enjoyed running with you a lot! Our weekly interval trainings on the track were a huge success. Let us try to keep up the shared runs whenever we can, and at least run a marathon together (hopefully Berlin next year!). **Margarita**, thank you for all of the nice coffee gatherings at the bookstore. We have spent a good amount of time together in the last months of my PhD and that has been very nice. To me, you are always an inspiring person to talk with. Also together with **Shaiv**, we have spent a lot of time at the bookstore and I have enjoyed that a lot. Both of you inspired me to pick up reading again. I am looking forward to continue our friendship. **Melania**, thank you for all of the fun together and for your ever-existing interest and compassion. When I think of you, I think of the many nice little chats that we have had in the office. You have also been checking up on me sometimes and I appreciated that a lot. **Claudia**, also to you, thank you for all of the fun together and for being my office roommate for such a long time. I can imagine it must not have been easy to share an office with me and the other fitboys, haha. In any case, I was glad that you were accompanying us and it was always nice to have a chat with you. I am also very interested in the final results of your thesis as I was able to follow your research from up close. **Ahmed**, thank you for your help during my PhD. On top of the Editorial which we have written together, you have collected a good amount of clinical data for me which was essential for this thesis. Thank you for that. And sorry for bothering you with discussions about Monte Carlo simulations and particle swarm optimization haha, I hope you have been able to enjoy them. **Bart S., Koen vdL., Afrah, Rita, Cindy**, somewhere along the way of this section I have to stop addressing people individually, as my budget for printing this thesis is limited. But really, thank you. While we may have spent a little less time together, I am happy that you were a part of my PhD journey. With every single one of you it has always been nice to have a chat. And even in the current times of hybrid working, I think I was always able to find at least one of you at the office. That was nice to know. Also, **Anneloes, Gitte, Tom K.**, **Roel, Joey, Mehrdad,** thank you for all of the nice chats at the office and for your input during our Focus group meetings. It has been a pleasure to work together with you. Then, I also have a long list of people to thank who were part of the former BME team. With you guys, I have spent the first years of my PhD trajectory, and it has been a lot of fun. I truly have many wonderful memories of this time. **Peter H., Erik, Maarten, Sjeng, Ben, Niek, Frank B., Frank van R., Raoul, Lauren, Myrthe, Job S., Letty, Aurore.** Seeing all of your names together now, it makes me realize what a nice group of people that was. I am grateful that I have been a member of this group and I hope to see you on the day of my defense.

To continue, there are more people who I have worked with and who have had an impact on this thesis. **Frits,** you as a CRT expert and organizer of our shared TRANCE meetings have been significantly involved in my research and I thank you for bringing it to a higher level. It has been both fun and educative to have meetings with you. Thank you for your input during my PhD. The same holds for you, **Kevin**. I have learned a lot from having

meetings with you. As a computational modeler, it is great to experience that cardiologists are interested in your work and you clearly have shown to be supportive and cooperative. Being able to receive input from someone who sees patients on a daily basis is something that is a great stimulus to our work, in my opinion. I hope that you are going to keep up these nice collaborations. For similar reasons, I would like to express my gratitude to the Cardiology team of UMC Utrecht: **Bas, Feddo, Maarten Jan, Arco, Mathias, Philippe, Willem**. Your input has been essential to make this thesis into a success. Without the data that you have collected, which is of great quality, we would not have been able to perform our studies in the way we did. And on top of that, you have always shown a lot of interest in our work. That has been amazing to experience. Back to the MUMC+ team, I would like to thank **Twan** and **Miranda** for collecting some great-quality data for me as well. Your input to this thesis is much appreciated. Also, a thank you to **Richard, Uyen, Floor, Jolijn, Hongxing, Moedi, Nienke, Meike, Frans** for your useful input during our TRANCE meetings.

Then, switching back to BME, I would also like to thank **Wouter** for helping me with model parameter estimation. Your knowledge has been very useful and you always made time for me when I wanted to discuss. Thank you, really. Furthermore, **Theo**, thank you for your input during my PhD. It is great to see that you are still coming to the office after your retirement and you have so much knowledge to share. It helped me at different moments during my PhD. Thank you for that. Now, I might still be forgetting some people who I have worked with during my PhD trajectory. If so, please forgive me, it has been a long time. I would like to say that your input was no less appreciated.

I will continue by thanking some people who have otherwise influenced this thesis. **Alberto, Mitch, Jerremy, Peter D., Gijs**. Playing table tennis with you during lunch has been so much fun! Thank you for all of the entertaining workouts. After all, some movement during the day is important to stay productive. I would also like to thank the BM2wielers **Alberto, Peter H., Job S., Aurore, Frank van R., Maarten, Bart P., Letty, Niek** for the many beautiful rides in the surroundings of Maastricht. In my opinion, the ride to Drolenval was one of the most memorable ones, haha. It has been a pleasure. Furthermore, a thank you to the people from Ferro Mosae **Remco, Jeanine, Jonas, Andreas, Tom H., Thara, Thomas, Ilse, Eva, Sven S., Eline, Job vL., Amber H., Pieter, Meinte, Gregor**. Training with you was fun! Also, **Michele**, running with you on the track was nice! I hope to see you sometime during a marathon. To continue, **Skip, Janou, Jules**, thank you for all of our entertaining padel games.

And then, it is time to thank some more friends. **Paul**, wat ben ik blij om jou als vriend te hebben. Wij kennen elkaar goed en ik denk dat onze band alleen maar sterker is geworden. Ik kan altijd iets bij je kwijt en jij ook bij mij. Maar we kunnen het ook heerlijk luchtig houden en samen lachen om simpele dingen. Dankjewel voor alles! **Edse, Per-Olav,** dankjewel voor alle leuke momenten samen. Mooi dat we elkaar altijd weer weten te vinden. Ik heb het dan ook altijd super naar mijn zin. Ook met jullie kan ik goed praten en ik weet dat ik op jullie kan rekenen. Dat is geweldig om te weten, en dat is ook zeker wederzijds. **Stanley, Jeroen,**

ook aan jullie dankjewel voor alle leuke momenten. Er zijn eigenlijk weinig woorden voor nodig, wij hebben het gewoon altijd naar ons zin samen, wat we ook doen. Dankjewel voor alle gezelligheid! **Amber L., Sven M.**, ik ben blij dat ik jullie heb leren kennen tijdens mijn PhD. Jullie zijn goede vrienden geworden en ik vind het altijd leuk om jullie te zien. Ik kijk er naar uit om contact te houden en ik ga zeker proberen om ook aanwezig te zijn bij jullie verdedigingen.

And then, it is time to thank some more people who have really had an impact on this thesis. The people who are close to me. **Papa, Mama**, ik weet niet eens waar ik moet beginnen. Waar zou ik zijn zonder jullie? Ik ben jullie enorm dankbaar voor alles. Ik denk dat we wel weten van elkaar hoe het zit. Ik ga er hier dan ook niet heel veel meer woorden aan besteden. Ik hou van jullie. Dankjewel! Ook mijn zus **Romy**, dankjewel dat je er altijd voor me bent. Het is zo fijn om even te kunnen bellen wanneer dat nodig is. Ik ben ontzettend dankbaar voor de band die wij hebben. En datzelfde geldt voor jou, **Steven**. Wat fijn dat jij onderdeel bent van onze familie en dat je altijd een helpende hand toesteekt wanneer dat nodig is. Je hebt voor dit boekje ook nog eens mijn cover ontworpen en figuren bewerkt, dankjewel daarvoor! Ook zou ik graag mijn lieve nichtje **Tessa** en neefje **Huub** willen bedanken. Wanneer ik weer een appje ontvang dat **Tessa** 'oom Tijmen' heeft gebeld, krijg ik altijd een lach op mijn gezicht. **Huub** is nog wat te klein om dat te doen, maar ik wil nu alvast zeggen dat ook hij me altijd mag bellen. Tja, en dan wil ik toch ook jou bedanken, **Bibi**. Je bent nu eenmaal onderdeel geweest van een groot gedeelte van mijn PhD traject. Voor altijd zul je een speciaal plekje in mijn hart hebben. Ik ben je ontzettend dankbaar dat je me hebt bijgestaan tijdens deze periode en ik heb veel van je geleerd. We hebben samen heel veel leuke momenten beleefd en die momenten koester ik. Echt, dankjewel daarvoor! Ook dank aan **Maud, Leon** en **Lars** voor jullie warme ontvangst. Ik heb me altijd zeer welkom en op mijn gemak gevoeld bij jullie. Jullie hebben ook zeker een aandeel in deze thesis.

Het is nu denk ik wel tijd om dit stuk af te sluiten. Nogmaals, het zou kunnen dat ik iemand vergeten ben in dit hele verhaal. Zo ja, mijn oprechte excuses hiervoor en weet dat ik je niet minder dankbaar ben voor jouw verrichtingen. Tot ziens en liefs,

Tijmen

CURRICULUM VITAE

Tijmen Koopsen was born on May 4, 1994 in Veldhoven, Noord-Brabant, The Netherlands. He completed gymnasium (pre-university education) at Christiaan Huygens College in July 2011, after which he started his academic education at Eindhoven University of Technology (TU/e) in September 2011. At TU/e, he obtained his Bachelor's degree in Biomedical Engineering in 2014. In 2015, he started his Master Medical Engineering, which included clinical modules at Maastricht University with a strong focus on clinically applied research. Tijmen chose to specialize in computer modeling and cardiovascular physiology and he started his Master thesis research at the end of 2015, under the supervision of Prof. dr. ir. Joost Lumens and Prof. dr. Tammo Delhaas. The main subject of his thesis was the deformation imaging-based detection of myocardial scar. As a part of this research, he performed an internship at University of Pittsburgh Medical Center (UPMC) in 2016, under the supervision of Prof. dr. John Gorcsan III. At UPMC, he got trained in speckle tracking echocardiography and he collected data of patients with ischemic heart disease and left bundle branch block.

After obtaining his Master's degree in 2017, Tijmen started as a PhD candidate at the Department of Biomedical Engineering at Maastricht University, under the supervision of prof. dr. ir. Joost Lumens and prof. dr. Tammo Delhaas. During his PhD, he worked on the personalization of a computer model of the heart and circulation, CircAdapt, to predict the outcome of pacemaker therapy in patients with dyssynchronous heart failure. To personalize the model, he used non-invasive deformation imaging measurements, and he developed an algorithm which generated the patient's Digital Twin.

Tijmen will continue his career at Bright Society, through which he currently works as a system integrator at Philips Healthcare in Best, The Netherlands.

LIST OF PUBLICATIONS

Peer reviewed journals

Hermans BJM, Bennis FC, Vink AS, **Koopsen T**, Lyon A, Wilde AAM, Nuyens D, Robyns T, Pison L, Postema PG, Delhaas T (2020). Improving long QT syndrome diagnosis by a polynomial-based T-wave morphology characterization. *Heart Rhythm*. 17(5), 752-758.

van Osta N, Lyon A, Kirkels F, **Koopsen T**, van Loon T, Cramer MJ, Teske AJ, Delhaas T, Huberts W, Lumens J (2020). Parameter subset reduction for patient-specific modelling of arrhythmogenic cardiomyopathy-related mutation carriers in the CircAdapt model. *Phil. Trans. R. Soc. A*. 378(2173), 20190347.

van Osta N, Kirkels F, Lyon A, **Koopsen T**, van Loon T, Cramer MJ, Teske AJ, Delhaas T, Lumens J (2021). Electromechanical substrate characterization in arrhythmogenic cardiomyopathy using imaging-based patient-specific computer simulations. *Europace*. 23, i153-i160.

Lumens J, **Koopsen T**, Beela AS (2021). What Do We Gain From Septal Strain? *JACC Cardiovasc Imaging*. 14(9), 1703-1706.

van Osta N, Kirkels FP, van Loon T, **Koopsen T**, Lyon A, Meiburg R, Huberts W, Cramer MJ, Delhaas T, Haugaa KH, Teske AJ, Lumens J (2021). Uncertainty Quantification of Regional Cardiac Tissue Properties in Arrhythmogenic Cardiomyopathy Using Adaptive Multiple Importance Sampling. *Front. Physiol*. 12, 1-15.

Koopsen T, van Osta N, van Loon T, van Nieuwenhoven FA, Prinzen FW, van Klarenbosch BR, Teske AJ, Vernooy K, Delhaas T, Lumens J (2022). A Lumped Two-Compartment Model for Simulation of Ventricular Pump and Tissue Mechanics in Ischemic Heart Disease. *Front. Physiol*. 13, 1-17.

Koopsen T, van Osta N, van Loon T, Meiburg R, Huberts W, Beela AS, Kirkels FP, van Klarenbosch BR, Teske AJ, Cramer MJ, Bijvoet GP, van Stipdonk A, Vernooy K, Delhaas T, Lumens J (2024). Parameter Subset Reduction for Imaging-Based Digital Twin Generation of Patients with Left Ventricular Mechanical Discoordination. *Biomed. Eng. Online*. 23(1), 46.

Koopsen T, Gerrits W, van Osta N, van Loon T, Wouters P, Prinzen FW, Vernooy K, Delhaas T, Teske AJ, Meine M, Cramer MJ, Lumens J (2024). Virtual Pacing of a Patient's Digital Twin to Predict Left Ventricular Reverse Remodelling after Cardiac Resynchronization Therapy. *EP Europace*. 26(1), 1-8.